University of Alberta

Fabrication and Applications of Highly Porous Thin Films

by

Kenneth David Harris ©

A thesis submitted to the Faculty of Graduate Studies and Research in partial fulfillment of the requirements for the degree of Doctor of Philosophy

Department of Electrical and Computer Engineering

Edmonton, Alberta
Spring 2003

National Library
of Canada

Acquisitions and
Bibliographic Services

395 Wellington Street
Ottawa ON K1A 0N4
Canada

Bibliothèque nationale
du Canada

Acquisisitons et
services bibliographiques

395, rue Wellington
Ottawa ON K1A 0N4
Canada

Your file Votre référence
ISBN: 0-612-82112-9
Our file Notre référence
ISBN: 0-612-82112-9

The author has granted a non-exclusive licence allowing the National Library of Canada to reproduce, loan, distribute or sell copies of this thesis in microform, paper or electronic formats.

The author retains ownership of the copyright in this thesis. Neither the thesis nor substantial extracts from it may be printed or otherwise reproduced without the author's permission.

L'auteur a accordé une licence non exclusive permettant à la Bibliothèque nationale du Canada de reproduire, prêter, distribuer ou vendre des copies de cette thèse sous la forme de microfiche/film, de reproduction sur papier ou sur format électronique.

L'auteur conserve la propriété du droit d'auteur qui protège cette thèse. Ni la thèse ni des extraits substantiels de celle-ci ne doivent être imprimés ou aturement reproduits sans son autorisation.

Canada

University of Alberta
Library Release Form

Name of Author: Kenneth David Harris

Title of Thesis: Fabrication and Applications of Highly Porous Thin Films.

Degree: Doctor of Philosophy

Year this Degree Granted: 2003

Permission is hereby granted to the University of Alberta Library to reproduce single copies of this thesis and to lend or sell such copies for private, scholarly or scientific research purposes only.

The author reserves all other publication and other rights in association with the copyright in the thesis, and except as herein before provided, neither the thesis nor any substantial portion thereof may be printed or otherwise reproduced in any material form whatever without the author's prior written permission.

Kenneth David Harris
56 Ross Haven Way
Medicine Hat, Alberta
T1B-2T8

Submitted to the Faculty of Graduate Studies and Research on November 27th, 2002

"That is the only thing that never fails. You may grow old and trembling, you may miss your love and lose your moneys to a monster, you may see the world about you devastated by evil lunatics, or know your honour trampled in the sewers of baser minds. There is only one thing for it then – to learn. Learn why the world wags and what wags it. That is the only thing the poor mind can never exhaust, never alienate, never be tortured by, never fear or distrust, and never dream of regretting. Learning is the thing for you."

-T.H. White, The Sword in the Stone

University of Alberta
Faculty of Graduate Studies and Research

The undersigned certify that they have read, and recommend to the Faculty of Graduate Studies and Research for acceptance, a thesis entitled *Fabrication and Applications of Highly Porous Thin Films* submitted by Kenneth David Harris in partial fulfillment of the requirements for the degree of Doctor of Philosophy

Dr. Michael Brett

Dr. Ying Tsui

Dr. Christopher Backhouse

Dr. Jeremy Sit

Dr. Frank Hegmann

Dr. David Pulfrey
University of British Columbia

November 8th, 2002

To my family
. . . (there through all)

Abstract

Using traditional glancing angle deposition (GLAD) as a starting point, some major refinements and extensions to the existing technology are described. The fabrication of adhesion-promoting microstructures, multilayered thin films, thin films of variable composition and controlled chevron thin films are discussed, and the possibility of patterning GLAD thin films by photolithography is described. Two successful efforts to create GLAD-like structures in typical microchannel arrangements are then discussed along with measurements of the surface area amplification that these geometries provide. The creation of inverse, or negative, perforated thin film structures is the final fabrication-based topic. No structures of similar form are found anywhere else in the scientific literature, and consequently, a great deal of space is reserved for the elucidation of the wide range of structures that may be formed.

Specific applications of the newly developed process technology are also discussed. Effective, GLAD-based humidity sensors, optical polarization rotation filters, and electrodeposited, chiral, metallic thin films are all thoroughly described. A functional hydrocarbon sensor composed of helical Pt structures is discussed, and extremely sensitive electrochemical sensors for H_2S and SO_2 are presented. Thick, multilayered, zirconia thin films having measured thermal conductivities significantly lower than contemporary, state-of-the-art thermal barrier coatings are also presented.

Acknowledgements

It seems I've been preparing to write this page since the very hour I began sitting in classrooms. From the teachers who taught me, to the friends who reassured me, countless people have helped along the way, and it's a daunting task to describe them all.

First of all, Dr. Brett, you provided my first introduction to microfabrication (and occasional refresher courses along the way). Had you been reticent about what you knew, this thesis would be about 200 pages shorter, and I'd be a much smaller person. Whenever obstacles appeared, thanks for providing insights and ideas which never failed to start things moving again.

Each and all of the members of the glancing angle deposition research group (Kevin, Cyrus, Doug, Greg, Jim, Mary, Jeremy, Brian, Scott, Mike, Martin, Barb, Peter, Andy and Anastasia) were important in much the same fashion. You taught me what I needed to know and helped me dream up new ideas whenever it was necessary. What's more, my computer has always been running, the evaporators have always ended up reassembled, and I've never been lacking for assistance in calibrating the ballistic simulator. Thanks.

Whenever I didn't quite know how to make something I'd dreamt up, Ken Westra was usually the first person I'd consult. The University of Alberta's nanofabrication facility and all of the capabilities it provides may be impressive, but they're nothing if you don't know how to use them. So because you readily provided advice, I am indebted. Furthermore, thanks are extended to Keith Franklin because usually the equipment was working, and when it wasn't, you were on top of it, and to Hue Nguyen, Nicole Morin and Stephanie Bozic who taught me some vital processing techniques, and then set me loose to experiment on my own.

Also essential was George Braybrook, that amazing photographer, who captured every one of the SEM images contained within these pages (and told great stories while doing so), and Herbert Dexel and the machinists who were always able to translate my mysterious hand motions into those mechanical devices which were so essential to this work. And to Albert Huizinga, who really knows his electronics, thanks for all the assistance in assembling the circuitry that became necessary as the work progressed.

As the scope of this thesis has steadily broadened to include new concepts, I've also been consistently blessed with an ever expanding group of knowledgeable collaborators. Drs. Backhouse, Elezzabi, Harrison, McMullin and Jon Holzman at the University of Alberta, Drs. Prohaska and Dalmia from Perkin Elmer, Drs. McBride and Neitering of Ford, Dr. Josell and Eduardo Gonzalez from NIST, Dr. Smy of Carleton University, and Dr. Broer of the Technical University of Eindhoven and Philips Research Laboratories have all played vital roles in particular aspects of my research, and for these contributions, I extend my gratitude.

But now things change . . . Mom, Dad, sure you don't know very much about "nanostructured thin films", but you taught me how to spell my name. Which is the more important contribution? Not only were you my first teachers, but, more importantly, you taught me how to live, and how to learn. All this thin films stuff is bunk anyway.

Finally, to everyone who's stopped me in the halls to chat, distracted me when I should have been working, or who's simply smiled at the right time . . . thanks. You've made it worthwhile.

Table of Contents

Chapter One – The Growth of Thin Films and Glancing Angle Deposition 1

1.1 – Introduction 2
    1.1.1 – Nanostructured thin films 2
    1.1.2 – Historical aspects of glancing angle deposition 2
    1.1.3 – Contemporary GLAD research 3
    1.1.4 – Thesis organization 3
1.2 – Thin Films and Deposition Techniques 4
1.3 – Growth of Thin Films at Normal Incidence 5
1.4 – Growth of Thin Films at Glancing Incidence 8
    1.4.1 – The creation of porosity 8
    1.4.2 – Preferential growth 9
1.5 – Substrate Motion 11
1.6 – Typical GLAD Microstructures 12
    1.6.1 – The slanted post microstructure 13
    1.6.2 – The chevron microstructure 14
    1.6.3 – The helical microstructure 14
    1.6.4 – The posts microstructure 15
    1.6.5 – Capping of porous thin films 16

Chapter Two – Column Angle Variations in Chevron Thin Films 22

2.1 – Chevron Column Angle Variations 23
2.2 – Theoretical Considerations 28
2.3 – Chevron Thin Film Simulations 31

Chapter Three – Advanced Processing with Glancing Angle Deposition 34

3.1 – The Development of GLAD Technology 35
3.2 – The Graded Density Microstructure 35
3.3 – Patterning of GLAD Thin Films 38
    3.3.1 – Photolithography 38
    3.3.2 – Photoresist application 38
    3.3.3 – Pattern transferal 40
    3.3.4 – Residual photoresist 44
    3.3.5 – Summary 45
3.4 – Controlled Positioning of GLAD Structures 45
3.5 – GLAD Microstructures of Variable Composition 48
    3.5.1 – Multi-material depositions 48

3.5.2 – Composition analysis 49
3.5.3 – Potential applications 49

Chapter Four – High Surface Area Microchannels 54
4.1 – The Lab-On-A-Chip Concept 55
4.2 – Glancing Angle Deposition over Microchannel Topography 56
4.2.1 - Glancing angle depositions into microchannels 56
4.2.2 - Alignment issues 58
4.3 – Photolithographically Defined Channels 60
4.4 – Surface Area Measurement by Porosimetry 61
4.5 – Surface Area Measurement by Simulation 63

Chapter Five – Perforated Thin Films 67
5.1 – Existing Technology 68
5.2 – Fabrication of Perforated Thin Films 69
5.3 – Variants of Perforated Thin Films 73
5.3.1 – Alternate pitch helically perforated thin films 73
5.3.2 – Chevron perforated thin films 74
5.3.3 – Periodically perforated thin films 75
5.3.4 – Variations in filler material 76
5.4 – The Perforated Thin Film Process 78
5.5 – Replica Thin Films 78
5.5.1 – Materials limitations 78
5.5.2 – Electrodeposition of GLAD films 79
5.5.3 – Composition analysis 83

Chapter Six – Applications of Perforated Thin Films 88
6.1 – Introduction 89
6.2 – Perforated Thin Film Humidity Sensors 89
6.2.1 – Existing GLAD humidity sensors 89
6.2.2 – Construction of a perforated thin film humidity sensor 89
6.2.3 – Sensor calibration 92
6.2.4 – Response time 93
6.3 – Optical Polarization Rotation by Perforated Thin Films 95
6.3.1 – Optical activity and theoretical considerations 95
6.3.2 – Polarization rotation measurements 96

Chapter Seven – Sensor Applications of GLAD Thin Films 102
7.1 – Electrochemical Sensors 103
7.1.1 – The electrochemical sensor application 103
7.1.2 – Functionality of an electrochemical sensor 103
7.1.3 – Sensor production 104

7.1.4 – Electrochemical testing 108
7.1.5 – SO_2 test results 109
7.1.6 – H_2S test results 111
7.1.7 – Advantages of GLAD gas sensors 112
7.2 – Microcalorimetric Sensors 113
7.2.1 – The automotive hydrocarbon sensor application 113
7.2.2 – GLAD hydrocarbon sensors 114
7.2.3 – Catalytic testing 115
7.2.4 – The helical microstructure 117
7.2.5 – Control samples 119
7.2.6 – Comparison of results 121

Chapter Eight – Thermal Barrier Coatings 127
8.1 – Traditional Thermal Barrier Coatings 128
8.2 – Deposition of YSZ Thin Films 130
8.3 – Theoretical Thermal Conductivity Estimates 132
8.3.1 – Theoretical considerations 132
8.3.2 – Thermal conductivity measurement by simulation 137
8.4 – Thermal Conductivity Measurements 139
8.4.1 – The mirage effect 139
8.4.2 – The 3ω technique 140
8.4.3 – Test results 141

Chapter Nine – Conclusions and Recommendations 147
9.1 – Summary 148
9.2 – Recommendations 149

Appendix A – Properties of the Humidity Control Chamber 155

Appendix B – The Response Time Test Circuit 160

Appendix C – Derivation of the Conversion Efficiency Equation 164

List of Tables

Table 3.1 – Steps in the patterning of SiO_2 GLAD microstructures 45
Table 5.1 – Steps in the production of a perforated thin film 78
Table 6.1 – Polarization rotation of light by various films 97
Table 7.1 – Results of the catalytic test experiments 119
Table 8.1 – Measured parameters for TBC calculations 136
Table 8.2 – Results of the thermal diffusivity measurements 142

List of Figures

Chapter One

Figure 1.1 – The electron beam evaporator 6
Figure 1.2 – Adatom diffusion 7
Figure 1.3 – The formation of a normal incidence thin film 8
Figure 1.4 – Early growth of a thin film deposited at glancing incidence 9
Figure 1.5 – Growth of a thin film deposited at glancing incidence 10
Figure 1.6 – A conceptual drawing of the GLAD system 11
Figure 1.7 – The GLAD deposition system 12
Figure 1.8 – The slanted posts microstructure 13
Figure 1.9 – The chevron microstructure 14
Figure 1.10 – The helical microstructure 15
Figure 1.11 – The posts microstructure 16
Figure 1.12 – Capping porous thin films 17

Chapter Two

Figure 2.1 – Definition of column angles 24
Figure 2.2 – SEM images of chevron thin films 25
Figure 2.3 – Binary image of a single chevron arm 26
Figure 2.4 – Column orientation function plots for the ZrO_2 film 27
Figure 2.5 –Column orientation function plots for the SiO_2 film 27
Figure 2.6 – Theoretical behavior of β_2 and β_1 with changes in α 29
Figure 2.7 – Theoretical behavior of the ultimate column angle (β_∞) 31

Chapter Three

Figure 3.1 – The graded density microstructure 37
Figure 3.2 – Potential difficulties in filling GLAD films with photoresist 39
Figure 3.3 – A GLAD thin film filled with photoresist 41
Figure 3.4 – Photoresist removed from selected areas of a GLAD film 42
Figure 3.5 – Lines of GLAD structures produced by photolithography 43
Figure 3.6 – Photoresist residue 44
Figure 3.7 – The concept of seed layers for controlled nucleation 46
Figure 3.8 – A periodic seed layer for glancing angle deposition 47
Figure 3.9 – Examples of GLAD thin films deposited onto periodic arrays 47
Figure 3.10 – GLAD microstructures of variable composition 48
Figure 3.11 – EDX spectrum from an alternating material GLAD film 49

Chapter Four

Figure 4.1 – A typical microchannel 56
Figure 4.2 – Filling an etched microchannel by glancing angle deposition 57

Figure 4.3 – A microchannel filled with GLAD structures 58
Figure 4.4 – The severity of misaligned depositions into microchannels 59
Figure 4.5 – Lithographic microchannels 60
Figure 4.6 – Capped lithographic microchannels 61
Figure 4.7 – A TPL porosity sensor 62
Figure 4.8 – Computer-generated simulation of a helical GLAD film 63
Figure 4.9 – Simulated surface area 64

Chapter Five

Figure 5.1 – Conceptual steps in the fabrication of a perforated thin film 70
Figure 5.2 – Steps in the fabrication of a perforated thin film 71
Figure 5.3 – Large pitch helical perforations 74
Figure 5.4 – Chevron perforated thin films 75
Figure 5.5 – Periodic perforations 76
Figure 5.6 – Perforated spin-on-glass thin film 77
Figure 5.7 – Motivation for alternate fabrication techniques 80
Figure 5.8 – Replication of a GLAD film by electrodeposition 81
Figure 5.9 – Replica thin film template 81
Figure 5.10 – Ni replica thin film 82
Figure 5.11 – Cu replica thin film 83
Figure 5.12 – EDX spectrum for electroplated Ni helices 84

Chapter Six

Figure 6.1 – Conceptual diagram of a helically perforated humidity sensor............ 90
Figure 6.2 – The perforated thin film humidity sensor 91
Figure 6.3 – Calibration of the PTF humidity sensor 92
Figure 6.4 – Typical capacitance response curves 94
Figure 6.5 – Positions of the optical materials 96
Figure 6.6 – The polarimeter concept 98

Chapter Seven

Figure 7.1 – Steps in the fabrication of GLAD electrochemical gas sensors 106
Figure 7.2 – SEM images of the porous electrolyte carrier films 107
Figure 7.3 – Schematic diagram of an electrochemical sensor 108
Figure 7.4 – Typical SO_2 oxidation current response for the 60° sensor 109
Figure 7.5 – Typical SO_2 oxidation current response for the 0° sensor 109
Figure 7.6 – Typical H_2S oxidation current response for the 60° sensor............ 111
Figure 7.7 – Typical H_2S oxidation current response for the 0° sensor 112
Figure 7.8 - Catalytic test films 114
Figure 7.9 – The gas flow reactor 116
Figure 7.10 – Conversion efficiency of the Pt GLAD sample 118
Figure 7.11 – Conversion efficiency of the sputtered sample 120
Figure 7.12 – Conversion efficiency of an alumina supported catalyst 121

Chapter Eight

Figure 8.1 – Traditional TBC schemes 129
Figure 8.2 – The GLAD TBC microstructure 130
Figure 8.3 – GLAD structures of YSZ 131
Figure 8.4 – Factors in the theoretical determination of thermal resistance 133
Figure 8.5 – Simulated GLAD TBCs 138
Figure 8.6 – Density and temperature within the simulated thin film 139
Figure 8.7 – The mirage technique 140
Figure 8.8 – The 3ω technique 141

Chapter Nine

Figure 9.1 – Actuated polymer thin film 150
Figure 9.2 – Membrane filtration 151

Appendix A

Figure A.1 – The humidity chamber control circuit 158

Appendix B

Figure B.1 – The oscillator circuit 162
Figure B.2 – The frequency-to-voltage converter 163
Figure B.3 – Sample response speed test circuit waveforms 163

Appendix C

Figure C.1 – Calculated conversion efficiency as a function of temperature 167

List of Symbols

α – vapor incidence angle (substrate's frame of reference)
α – thermal diffusivity
α – particle fraction
α' – vapor incidence angle (column's frame of reference)
α'_n – vapor incidence angle (column's frame of reference) for the nth component of a chevron thin film
β – columnar inclination angle (substrate's frame of reference)
β' – columnar inclination angle (column's frame of reference)
β_n – columnar inclination angle (substrate's frame of reference) of the nth component of a chevron film
β'_n – columnar inclination angle (column's frame of reference) for the nth component of a chevron thin film
β_∞ – steady-state column angle
γ – angle of misalignment between the microchannel axis and the direction of deposition
η – conversion efficiency
θ – arbitrary angle measured from the substrate normal
κ – thermal conductivity
κ_o – reaction rate constant
λ – wavelength
ρ – thermal resistivity
ρ – mass density
ρ – point density
ϕ – azimuthal position of the vapor source with respect to the substrate
ω – angular frequency
A – area
C – capacitance
C_p – specific heat capacity
D – spatial extent of an image in the direction perpendicular to the substrate
D – coefficient of binary molecular diffusion
E – activation energy
F – column orientation function
L – spatial extent of an image in the direction parallel to the substrate
Q – volumetric gas flow rate
R – redox ratio
R – thermal resistance
R_{cap} – thermal resistance of a solid cap
R_{cone} – thermal resistance of a slanted truncated cone
R_{para} – thermal resistance of a truncated paraboloid
R_{TBC} – total thermal resistance of a GLAD thermal barrier coating microstructure
R_{trad} – total thermal resistance of a traditional thermal barrier coating microstructure

RH – relative humidity
SNR – signal-to-noise ratio
T – temperature
T_o – gas temperature measured at the mass flow controllers
V – voltage
V_A – voltage at point A
V_B – voltage at point B
c – reactant concentration at the gas inlet
c_o – reactant concentration at the gas outlet
d – microchannel depth
d_1 – average column diameter at the lower bound of a slanted post region
d_2 – average column diameter at the upper bound of a slanted post region
d_3 – average column diameter in a capping layer
h – height of the gas flow reactor
h – arbitrary x-coordinate of a parabola
k – arbitrary y-coordinate of a parabola
k – Boltzmann's constant
k – dielectric constant
l – length of a test catalyst
n – an arbitrary number
n – average number of columns within a defined area A
n – index of refraction
n_A – index of refraction for material A
n_{air} – index of refraction for air
n_B – index of refraction for material B
n_{filler} – index of refraction for a material interpenetrating a GLAD film
n_{PR} – index of refraction for HPR504 photoresist
n_{SiO2} – index of refraction for evaporated SiO_2
n_{water} – index of refraction for liquid water
p – distance between a parabola vertex and focus
r – radius
r_3 – average column radius in a capping layer
r_2 – average column radius at the upper bound of a slanted post region
s – shadow width
s_{90° – shadow width at $\gamma = 90^\circ$
t – time
t_r – residence time
t – thickness
t_1 – thickness of a capping layer
t_2 – thickness of a paraboloidal pre-cap region
t_3 – thickness of a slanted posts region
w – microchannel width
w – width of a test catalyst
x – coordinate of a point in a thin film
y – coordinate of a point in a thin film
z – vertical position in a thin film

Chapter One

The Growth of Thin Films and Glancing Angle Deposition

1.1 – Introduction

1.1.1 – Nanostructured thin films: As evidenced by the current, world-wide investment, nanotechnology is gaining tremendous momentum in the international research community. Germany and Japan each spend approximately $200M annually in the field, the United States alone spends $518M per year, and Taiwan, a nation smaller than Canada in population, recently invested $290M in a single facility. New and existing institutions are continually turning their efforts towards solving today's technological problems by manipulation of structure on a nano-scale, and this trend is not expected to be a short term phenomenon.

One important element at the foundation of nanotechnology lies in the controlled construction of nanostructured thin films. Multitudes of distinct methods for producing these films are already known and commonly practiced by the scientific community. High aspect ratio nanostructures, for instance, are not difficult to locate in the literature. Femtosecond laser pulses,[1-3] high density plasma deposition,[4] reactive ion etches,[5] electrodeposition,[6] surfactant assemblies,[7,8] lateral oxidation processes,[9] and nanocluster masking[10] have all successfully produced these structures. Even helical structures are not unknown; coils and helices have resulted from techniques involving novel chemical effects,[11-12] strain design,[13] photopolymerization,[14,15] microcontact printing,[16] and depositions within blast furnaces.[17] However, the feature that tends to be lacking is control: control over the microstructure, control over the porosity and pore characteristics, and control over the materials. To achieve more reproducible structures, a greater degree of control must be exerted over the fabrication process, and one highly successful path to the achievement of this goal is the glancing angle deposition (GLAD) technique.

1.1.2 – Historical aspects of glancing angle deposition: Most of the critical, individual components of the GLAD technique had been documented well before the present University of Alberta research effort. Extremely oblique depositions, for instance, were investigated by Holland before 1953,[18] and in 1959, substrate rotation was described by Young and Kowal.[19] Furthermore, alternating azimuthal deposition angles were discussed by Motohiro and Taga in 1989,[20] and a variety of anisotropy effects have also been sporadically identified by various research groups.[21-25] What remained, however, was the incorporation of all these features into a single, well-controlled system to engineer specific nanostructures, and this was the culmination of the research of Robbie, et al.[26] Since then, the GLAD technique has provided the foundation for a great deal of additional work, and a description of my personal contribution to this work is the primary intent of this thesis.

1.1.3 – Contemporary GLAD research: As must be expected with any useful deposition technology, a number of research groups are simultaneously investigating aspects of the GLAD technique. Hodgkinson, et al., have investigated optical effects of chiral thin films deposited at reasonably oblique angles,[27] Lakhtakia has extensively described theoretical optical behavior,[28,29] Malac, et al, have described a fibrous quality of the films,[30,31] a group from the University of Alabama has investigated magnetic properties,[32,33] and Suzuki and Taga have very recently published papers describing a GLAD-like thin film integrating many types of microstructures[34] and a three-dimensional thin film simulator for predicting the surface area of films deposited at glancing incidence.[35] Yet despite the mounting interest in the technology, much opportunity remains for research endeavors involving the technique.

1.1.4 – Thesis organization: A wide range of topics are addressed in these pages; concepts such as photolithography, sensing mechanisms, and heat flow equations are all encountered and united by the theme of porous thin films (or more specifically, porous thin film fabrication processes and applications thereof). Every section of every chapter is directed towards either extending the capabilities of the GLAD technique, or towards evaluating GLAD films in specific applications. It has been my intention to provide readers with dependable procedures for recreating the structures described in this thesis, and to provide examples of where these techniques are useful. Whenever appropriate, possible directions for future research are also discussed and applications which have not been sufficiently pursued are identified.

As all of the work I intend to describe is based on thin film fabrication and glancing angle deposition, I begin with an overview of thin film technology and proceed to a specific description of the existing GLAD technique as practiced at the University of Alberta. In the second chapter, I then describe some of the complications inherent to the technology and potential methods for circumventing the problems. The thesis then moves toward peripheral techniques, and chapters three, four and five describe fabrication-based research, including the patterning of GLAD films, filled microchannel topologies, and perforated thin films. The remainder of the thesis, chapters six, seven, and eight, are devoted to working demonstrations of the films in specific applications. A short summary is then provided, and my recommendations regarding the most appropriate directions for future research are presented.

1.2 – Thin Films and Deposition Techniques

A thin film is simply a thin layer of any material. An enormous degree of variation is possible: a film may be liquid, solid, or gaseous; it may be composed of molecular compounds, metals, alloys, ceramics, polymers, organics, salts or any combination thereof; and it may range anywhere between millimeters to only a single atom in thickness. As in a soap bubble, a thin film does not even require a solid support structure. Despite such a broad definition, the effective scope of the term "thin film" can be limited for the purposes of this thesis: all the films I will describe from this point forward may be considered to be solid, and they will stand on separate solid bases known as substrates.

Considering the wide variety of thin films which exist, it is not surprising that there are also numerous methods for creating them. The substrate, for instance, may simply be immersed in and extracted from a bath containing the desired coating material. This is referred to as dip-coating, and it tends to produce fairly thick films of questionable uniformity.[36] Dozens of additional deposition methods are employed,[37,38] many of them common industrial practices, however, even the briefest description of each would entail a great deal of excessive text. In this work, the majority of the thin films have been deposited by electron beam physical vapour deposition (EB-PVD). This process will be described in detail in the next section, and wherever additional techniques are encountered, they too will be addressed.

1.3 – Growth of Thin Films at Normal Incidence

EB-PVD occurs in an electron beam evaporator. Inside the evaporator, thermionic emission from a tungsten filament creates a space charge of electrons surrounding the filament. These electrons are then accelerated by a high voltage (generally 6 to 10keV) and directed using magnetic fields toward a water cooled crucible. At the crucible, energy from the electron beam is transferred into the crucible contents which increases the vapour pressure of the evaporant and forces the ejection of gaseous particles.[39]

In the high vacuum environment of the electron beam evaporator, the mean free path for most gaseous species is sufficiently large (>100m) that the vast majority of particles follow straight-line trajectories once they leave the crucible.[40] Any direct line of sight between the crucible and the interior of the vacuum chamber is followed by outgoing particles, and any objects interrupting these paths are bombarded. In a typical EB-PVD deposition, two such objects are of particular importance. The first is the crystal thickness monitor (CTM), a quartz crystal which oscillates at a frequency dependent upon the mass (and consequently, the thickness) of film located on its surface.[41] If the CTM is in close proximity with the substrate, a reasonably reliable estimate of film thickness at the substrate may be obtained from the oscillator frequency. The second object is the substrate onto which we intend to deposit a film, and this is always placed in a position chosen to encourage deposition. A simplified depiction of the positioning of the elements in a standard, normal incidence thin film deposition is shown in Figure 1.1.

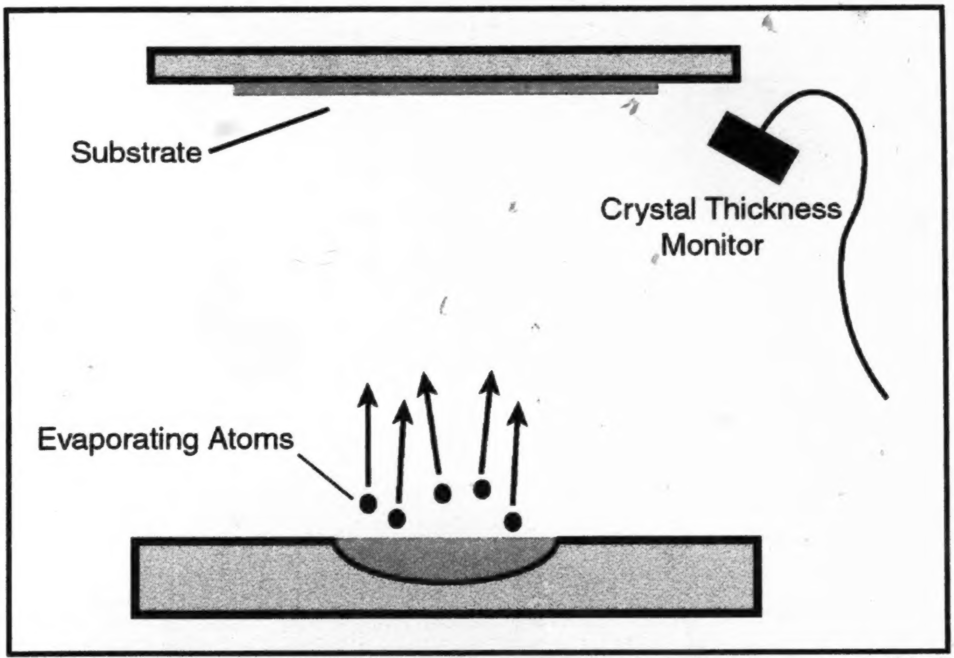

Figure 1.1 – The electron beam evaporator. A beam of electrons is projected toward a crucible filled with the evaporant material. Energy from the electron beam is transferred into the evaporant, and gaseous atoms are ejected from the crucible. These atoms then follow ballistic trajectories outward from the crucible until they encounter the substrate, crystal thickness monitor, or any other surface within the vacuum chamber.

Particles striking the substrate do not necessarily adhere to the surface immediately. After encountering a substrate, adatoms may simply reflect from the surface, or alternately, condense on the surface for a short time before re-evaporating into the vacuum chamber. In the most important case, however, a particle landing in a given position on the wafer first migrates a short distance before settling into a permanent, energetically favorable position.[42,43] (Figure 1.2) The possible range of migration is determined by a number of factors, such as the temperature of the substrate, the melting temperature of the evaporant, and the energy of the incoming particles. For example, substances that have lower melting temperatures are generally able to move further before being permanently incorporated into the film than higher melting point materials. This migration of adatoms has implications in the production of high quality GLAD films from high mobility substances.

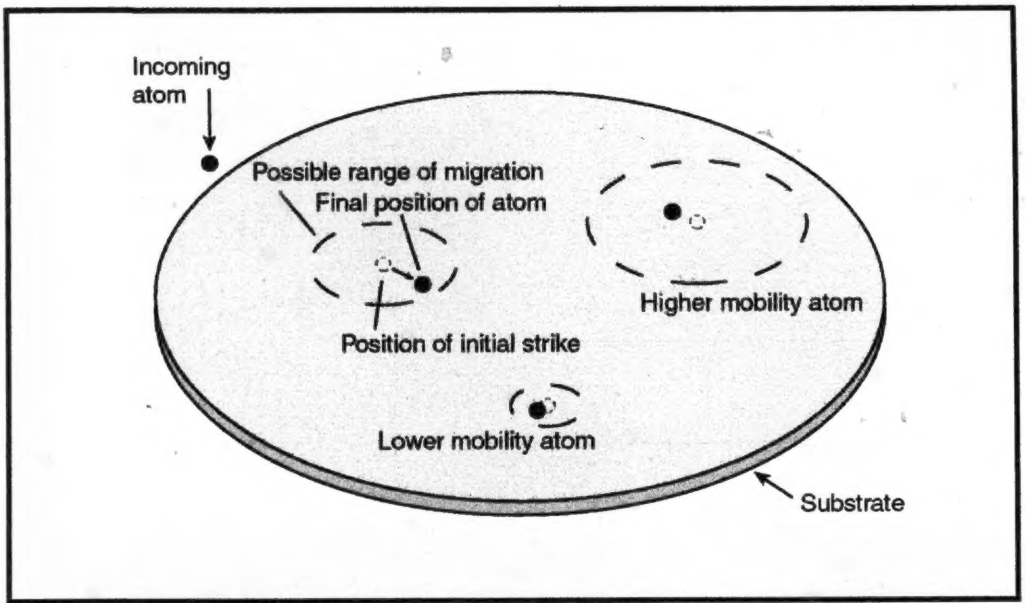

Figure 1.2 – Adatom diffusion. Gaseous particles strike the substrate surface and diffuse a small distance before settling into permanent positions. High mobility atoms (such as Cu or Au) are able to travel greater distances than particles of lower mobility (SiO_2, ZrO_2) before being incorporated into the film structure. Length scales in the drawing are highly exaggerated for illustrative purposes.

A state in which two atoms rest in contact with each other contains much less potential energy than a state in which the atoms are separated by a short distance. Therefore, atoms impinging upon the surface immediately begin to settle into small clusters known as nuclei, reducing the overall potential energy of the growing film. Thereafter, atoms striking the substrate tend to join pre-existing nuclei rather than forming additional clusters, and these nuclei begin to grow outward from their centers, covering a larger proportion of the total surface. Eventually, the nuclei will expand sufficiently as to begin to encounter one another at points across the substrate. Then, in a process known as coalescence, atoms from two neighboring nuclei rearrange themselves into a single, larger agglomeration having less exposed surface area and lower potential energy than the combination of the two previous clusters. The new, larger cluster then begins to grow outward as additional atoms are added. Eventually, coalescence will progress to a sufficient degree that a continuous film is formed across the entire substrate,[44,45] (see Figure 1.3).

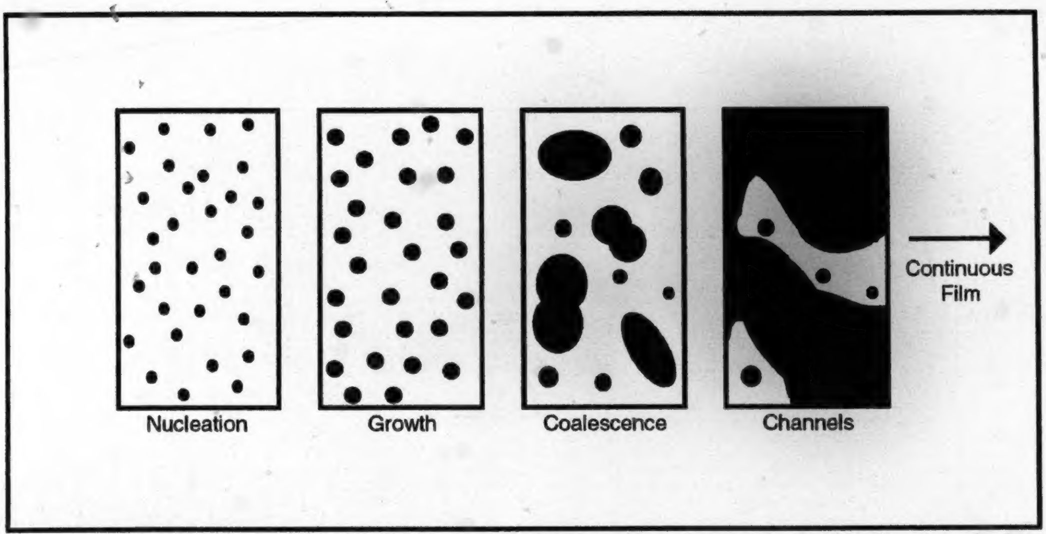

Figure 1.3 – Formation of a normal incidence thin film. In the early growth of a thin film deposited at normal incidence, atoms attempt to minimize their surface energy by forming small clusters or nuclei which then begin to grow outward from their centers. As they meet one another, these nuclei coalesce into larger particles, until ultimately all areas of the substrate are coated and a continuous film is formed.

1.4 – Growth of Thin Films at Glancing Incidence

1.4.1 – The creation of porosity: When particles arrive at the substrate from an oblique angle, the nucleation phase of thin film growth proceeds as described above. However, during the subsequent phases of growth, the three-dimensionality of the growing nuclei introduces another mechanism shaping the film microstructure. The nuclei begin to cast shadows behind themselves. (Figure 1.4) A restricted portion of the surface area (including the tops and "near" sides of the growing nuclei, and any portions of the substrate which do not fall within a shadowed region) is available to incoming atoms which arrive at oblique incidence. The greater the deposition angle, the greater the shadow area, and the more restricted the accessible surface area becomes. Thus, we have two offsetting effects: shadowing prevents incident flux from reaching certain regions, while atomic diffusion encourages it. At sufficiently oblique incidence, when the shadowing effect dominates atomic diffusion, a dramatic microstructural change takes place as some regions of the substrate become permanently inaccessible, and porosity is created within the film.[46]

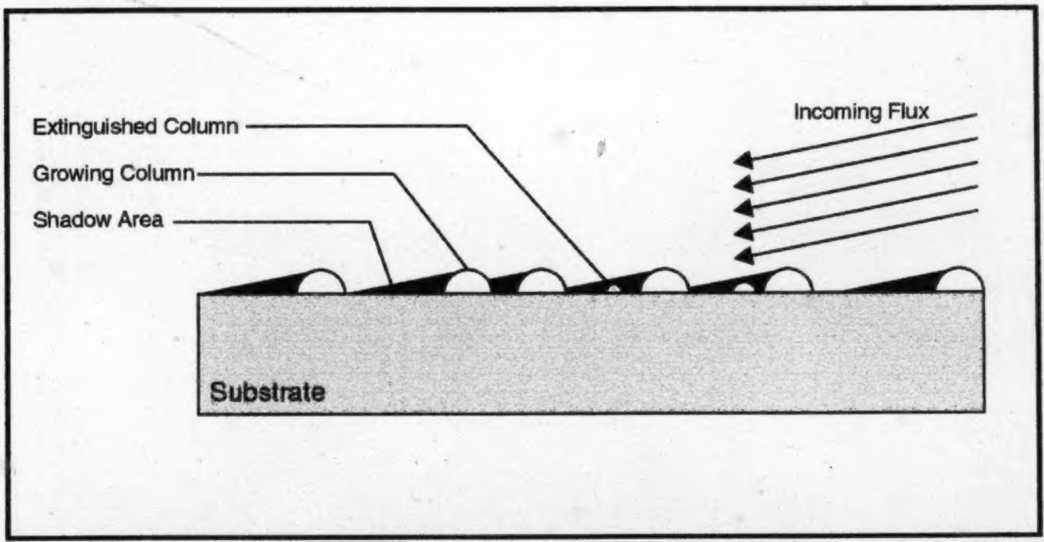

Figure 1.4 – Early growth of a thin film deposited at glancing incidence. During the nucleation stage of thin film growth, the three dimensionality of the atomic clusters creates shadows, or regions of surface where no adatoms may strike. Any nuclei lying entirely in the shadow of another nucleus will accumulate no additional atoms and thereby discontinue growing.

1.4.2 – Preferential growth: The angle of incidence (or deposition angle) in a thin film deposition is typically measured from the surface normal. By definition, glancing incidence is achieved when this angle, denoted α, exceeds 80°,[47] and such an experiment is then termed a glancing angle deposition (GLAD). Under these conditions, atomic shadowing is generally a stronger growth mechanism that surface migration, and the nuclei begin to grow without having filled in all areas of the substrate. Encountering the nuclei from an oblique angle, adatoms always strike in a confined area to one side of each growing nucleus, i.e., that side facing the vapor source. Consequently, as atoms are selectively incorporated on that particular side, the majority of growth occurs above each existing nucleus, but in a direction favoring the vapor source.[48] If, by random variations in the distribution of vapor flux, the shadow of one structure completely engulfs its neighbor, then the neighbor does not accumulate any additional particles, and its growth is terminated. The slightly larger structure will then be free to expand into the liberated areal space.

In Figure 1.5, an idealized GLAD thin film is depicted which has progressed well beyond the nucleation stage. As a result of limited diffusion, columnar microstructures have grown outward from the substrate, inclined in the direction of the vapor source. This is the most basic of the GLAD thin films; all other types are based on identical principles, but involve simple, substrate motion modifications. Numerous studies of the columnar angle of inclination, β, with variations in deposition angle have been completed for a variety of materials,[29,48-50] and both empirical (the tangent rule)[48] and geometrically based (Tait's rule)[49] equations have been developed, having some degree of success in predicting the actual inclinations observed. In general, the results show that β is always less than α, and that greater deposition angles lead to greater columnar inclination. (A more detailed discussion of Tait's rule and the tangent rule is provided in Chapter 2.)

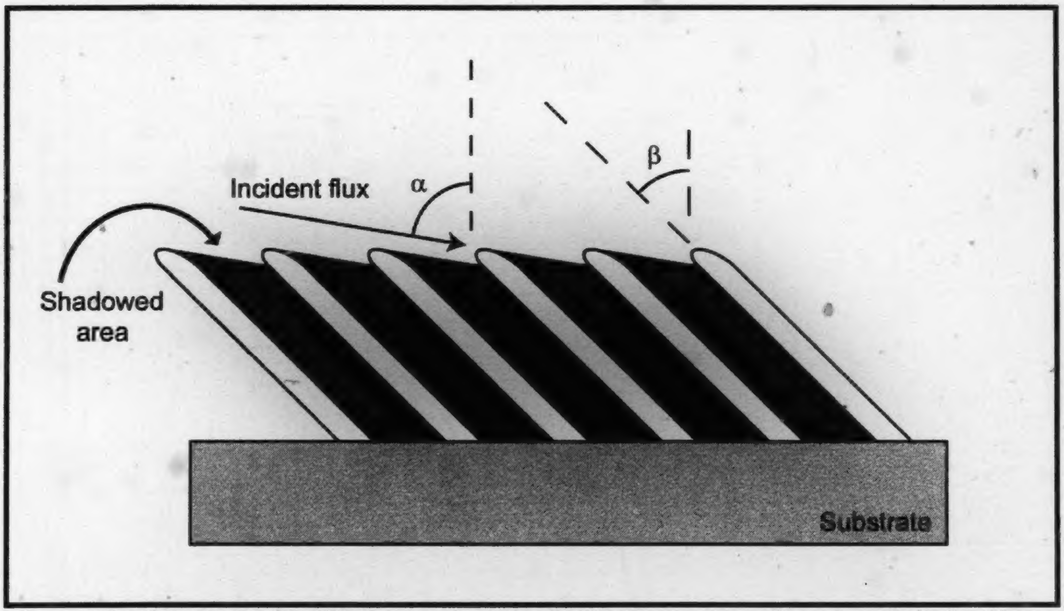

Figure 1.5 – Growth of a thin film deposited at glancing incidence. A growing column is inclined by an angle β in the direction of the vapor source, β always being less than the deposition angle, α. The effects of competition and column extinction have been ignored in this image.

1.5 – Substrate Motion

To create more versatile GLAD thin films, two properties are exploited.[26,51] First, the angle of incidence, α, determines both the inclination of the columns and the severity of shadowing in a growing film. Shadowing, in turn, controls the film porosity, and so control over α leads to a degree of control over the porosity of the thin film microstructure. Second, the columnar microstructures always grow in a direction favoring the vapor source, and so by changing the apparent position of the source with respect to the substrate, the direction of growth may be altered. A conceptual diagram of the apparatus which exploits these properties is located in Figure 1.6.

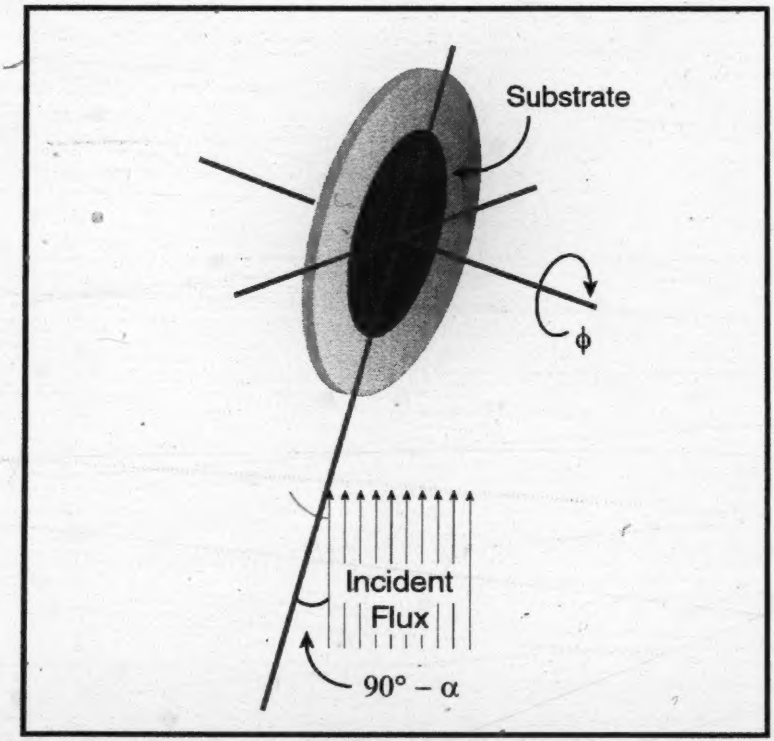

Figure 1.6 – A conceptual drawing of the GLAD system. Rotation of the substrate is possible about two axes: α adjusts the deposition angle, and consequently the film porosity, while φ controls the direction of microstructure growth.

In order to provide the smallest possible angular distribution of incident vapor flux in the GLAD system, a substrate is positioned at as great a distance from the vapor source as is practically feasible. In the most common configuration, the substrate/source separation is 41.5cm, which over a standard 4" wafer situated at $\alpha = 85°$ leads to an angular flux distribution of approximately ±2°. During the evaporation, the chuck and substrate are positioned using two computer-controlled stepper motors. One motor controls the film porosity by rotating the chuck about an axis passing directly across its surface and through its center (i.e., it adjusts α), while a second motor, by rotating the chuck about an axis perpendicular to its surface, adjusts the apparent azimuthal position of the vapor source with respect to a fixed line on the substrate (ϕ). The substrate position in both α and ϕ may be continuously varied throughout a deposition according to pre-programmed instructions, and a great deal of control over the microstructure of the completed film is maintained.[26] An image of the GLAD system is included as Figure 1.7.

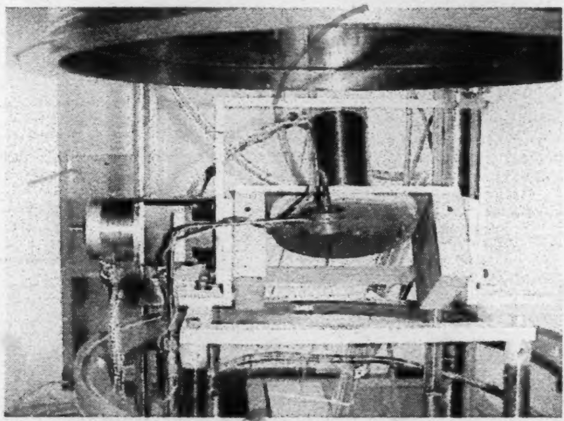

Figure 1.7 – The GLAD deposition system. The circular substrate mounting chuck is located near the center of the image, while the stepper motors for adjustment of ϕ and α are visible, respectively, above it and to its left.

1.6 – Typical GLAD Microstructures

In this section, five of the most common GLAD-produced microstructures will be discussed. For each, a description of the method of production and a conceptual drawing illustrating the activity of the stepper motors will be followed by an SEM image of an actual film. The fabrication of these five microstructures has been described in detail in previous works, and so within each section, references to publications having more complete descriptions will also be provided.

In general, thin films produced by the GLAD technique may be between approximately 80% (low α) and 20% (deposition angles near 90°) of bulk density. For illustrative purposes, the thin films depicted in this section will all be in an intermediate range, having approximate densities between 40% and 50% of bulk.

1.6.1 – The slanted post microstructure: No substrate motion is necessary in the production of the slanted posts microstructure.[48] Both stepper motors remain completely stationary throughout a deposition and are energized only to prevent any unexpected movement. Because the orientation of the microstructures with respect to the substrate crystal planes has been of little concern in research to date, the position of the ϕ motor is generally arbitrary. The α motor, however, is required to consistently maintain a position based upon the porosity and column angle which are desired. In Figure 1.8, one example of the slanted posts microstructure is shown. This is an aluminum film, 750nm in thickness which was deposited at $\alpha = 82°$. The column angle, β, is 51°.

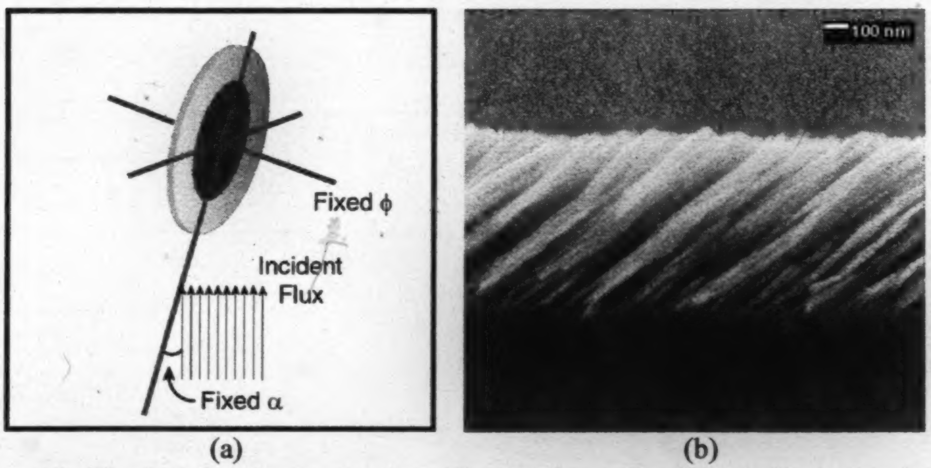

(a) (b)

Figure 1.8 – The slanted posts microstructure. The slanted posts film shown in (b) was deposited by holding the substrate fixed at a highly oblique angle (as depicted in (a)) throughout an entire deposition.

1.6.2 – The chevron microstructure: The fabrication of a chevron (or "zig-zag") structure may be visualized as the sequential stacking of slanted post microstructures. After completing one slanted posts segment as described above, the substrate is rotated 180° about the ϕ axis, and a second slanted posts microstructure growing in the opposite direction is initiated. This process is repeated until the desired number of chevron segments have been deposited.[52] Shown below (Figure 1.9) is a chevron thin film of SiO_2. Each of the eight, approximately 380nm thick, segments was deposited at $\alpha = 85°$, for a total thickness of 3.1μm. As in the slanted posts microstructure, the angle α was selected and held fixed to achieve the column angle and porosity that was required of the particular chevron film.

Some additional details and complications encountered in the growth of chevron thin films are discussed at greater length in Chapter 2.

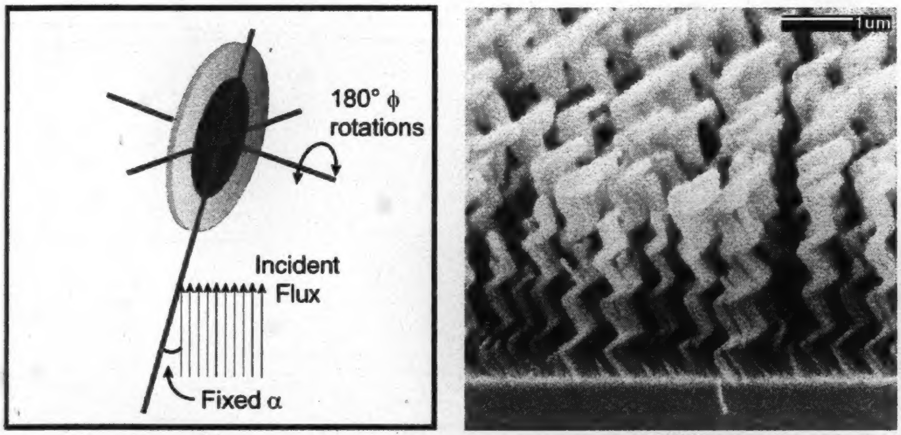

(a) (b)

Figure 1.9 – The chevron microstructure. As depicted in (a), the chevron film shown in (b) was deposited by periodically rotating the substrate through 180° in ϕ, while holding the deposition angle, α, constant at glancing incidence.

1.6.3 – The helical microstructure: In the making of a helical thin film, continuous substrate motion is employed. Rather than a burst of movement as a critical thickness is reached, the substrate is now rotated gradually, and the columnar structures, growing in a source-tracking manner, slowly wind outwards from the substrate as the azimuthal position of the source changes.[53] Reduced revolution rates lead to helices of greater pitch, however, in the GLAD control system, a constant revolution speed is not necessarily employed when attempting the production of a constant pitch helical film. Any fluctuations in the deposition rate (i.e., the rate at which thickness is added to a growing film) would lead to aberrations in the helical pitch under constant rotation conditions. In the current system, only when a specified thickness has been accumulated upon the CTM does the ϕ stepper motor make a step. This tends to produce more uniform helical films, and in addition, any step thickness may be specified to choose the helical pitch which is most useful. The film shown in Figure 1.10 is a helical SiO_2 thin film. During the deposition, the substrate underwent twelve complete rotations while being held at $\alpha = 85°$. The film is 3.6μm thick and has a helical pitch of 300nm.

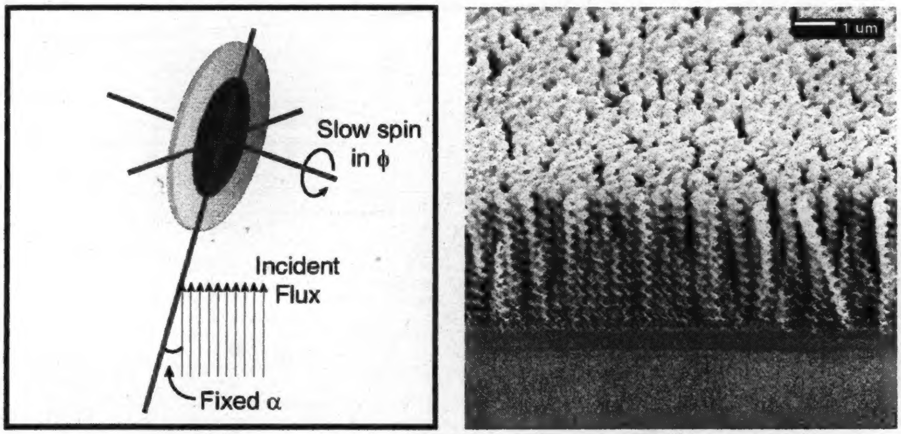

(a) (b)

Figure 1.10 – The helical microstructure. As depicted in (a), the helical film shown in (b) was deposited by slowly rotating the substrate in ϕ, while holding the deposition angle, α, at a highly oblique, but fixed value.

1.6.4 – The posts microstructure: The posts microstructure is a helical film of extremely small pitch.[54] If the substrate is rotated in ϕ with sufficient rapidity during a deposition, diffusion effects begin to overcome the source-seeking tendency of the columnar growth, and the helical structure is obscured. For many common evaporants, this effect occurs for rotation rates less than 1rpm, and helical pitches lower than about 30nm must be input to form the posts microstructure. The deposition angle α is held constant throughout the deposition to preserve the desired porosity. The film shown below in Figure 1.11 is a $ZrO_2(Y_2O_3)$ thin film which was deposited at $\alpha = 85°$. During the evaporation, the substrate was rotated 200 times in only 750nm of growth. No helical structure is apparent in the film.

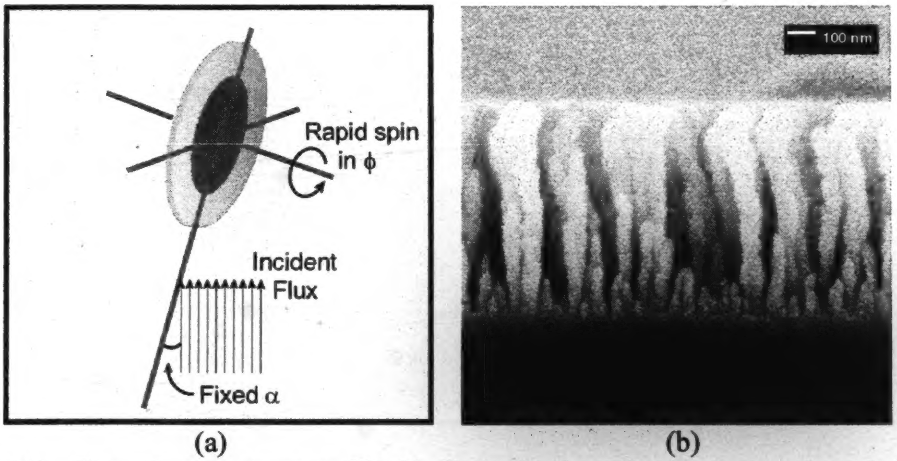

(a) (b)

Figure 1.11 – The posts microstructure. The thin film having the posts microstructure shown in (b) was deposited by rapidly rotating the substrate in ϕ, while maintaining a highly oblique, but fixed deposition angle, α.

1.6.5 – Capping of porous thin films: Nearly any type of GLAD film, including each of those described to this point, may be capped with a solid layer of material. To produce this microstructure, rotation of the substrate in α is necessary. Reducing α lessens the effect of shadowing in a growing film and increases the proportion of accessible surface area. Thus, reducing α encourages (through diffusion) the growing end of each column to broaden. The areal density of the film continually increases until the columns meet one another as a sufficiently low deposition angle is reached. Continuing the reduction in α, all areas are eventually filled in, and the cap becomes continuous. (In the first paper on the subject,[55] an exponential reduction was found to be the most effective method for varying α to produce a capping layer.) The capped film shown in Figure 1.12 is composed of SiO_2, and no gaps are apparent in the structure. It was initiated at $\alpha = 85°$, and the deposition angle was then reduced exponentially until $\alpha = 0°$ was reached.

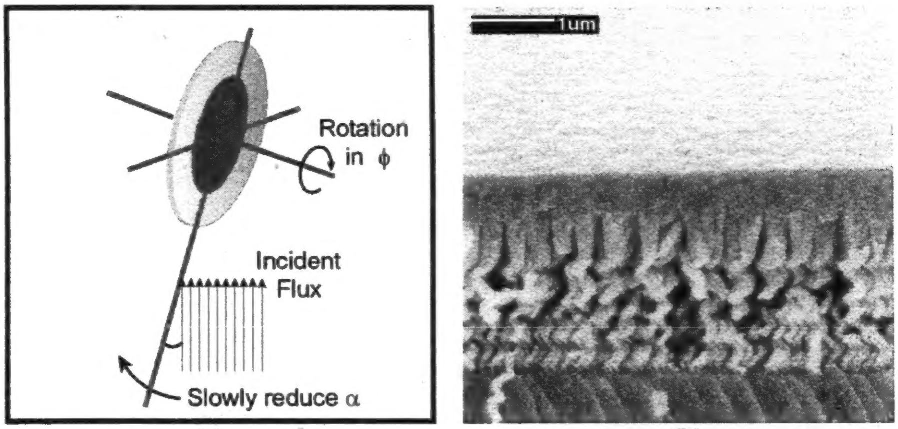
Rotation in ϕ
Incident Flux
Slowly reduce α
1um

(a) (b)

Figure 1.12 – Capping porous thin films. The application of a solid cap to a porous thin film may be accomplished by slowly reducing the deposition angle, α, while concurrently rotating the substrate in ϕ.

References

1) T.-H. Her, R.J. Finlay, C. Wu, S. Deliwala, E. Mazur, Microstructuring of silicon with femtosecond laser pulses, *App. Phys. Lett.*, **73**(12), 1673-1675, (1998).

2) A.J. Pedraza, J.D. Fowlkes, D.H. Lowndes, Silicon microcolumn arrays grown by nanosecond pulsed-excimer laser irradiation, *Appl. Phys. Lett.*, **74**(16), 2322-2324, (1999).

3) C. Wu, C.H. Crouch, L. Zhao, J.E. Carey, R. Younkin, J.A. Levinson, E. Mazur, R.M. Farrell, P. Gothoskar, A. Karger, Near-unity below-band-gap absorption by microstructured silicon, *Appl. Phys. Lett.*, **78**(13), 1850-1852, (2001).

4) A. K. Kalkan, S. Bae, H. Li, D.J. Hayes, S.J. Fonash, Nanocrystalline Si thin films with arrayed void-column network deposited by high density plasma, *J. Appl. Phys.*, **88**(1), 555-561, (2000).

5) D.M. Pooley, H. Ahmed, N.S. Lloyd, Fabrication and electron transport in multilayer silicon-insulator-silicon nanopillars, *J. Vac. Sci. Technol. B*, **17**(6), 3235-3238, (1999).

6) A. Jansson, G. Thornell, S. Johansson, High resolution 3D microstructures made by localized electrodeposition of nickel, *J. Electrochem. Soc.*, **147**(5), 1810-1817, (2000).

7) H. Yang, N. Coombs, G.A. Ozin, Morphogenesis of shapes and surface patterns in mesoporous silica, *Nature*, **386**, 692-695, (1997).

8) H. Yang, N. Coombs, I. Solokov, G.A. Ozin, Free-standing and oriented mesoporous silica films grown at the air-water interface, *Nature*, **381**, 589-592, (1996).

9) H. Fukuda, J.L. Hoyt, M.A. McCord, R.F.W. Pease, Fabrication of silicon nanopillars containing polycrystalline silicon/insulator multilayer structures, *Appl. Phys. Lett.*, **70**(3), 333-335, (1997).

10) T. Tada, T. Kanayama, Regular array Si nanopillars fabricated using metal clusters, *J. Vac. Sci. Technol. B*, **16**(6), 3934-3937, (1998).

11) S. Motojima, Q. Chen, Three-dimensional growth mechanism of cosmo-mimetic carbon microcoils obtained by chemical vapor deposition, *J. Appl. Phys.*, **85**(7), 3919-3921, (1999).

12) S. Motojima, W.-I. Hwang, X. Chen, H. Iwanaga, Preparation of TiN microcoils and microtubes by titanizing/nitriding of carbon and TiC microcoils, *J. Electrochem. Soc.*, **147**(3), 1228-1234, (2000).

13) V. Ya Prinz, D. Grützmacher, A. Beyer, C. David, B. Ketterer, E. Deckhardt, A new technique for fabricating three-dimensional micro- and nanostructures of various shapes, *Nanotechnology*, **12**, 399-402, (2001).

14) S. Maruo, S. Kawata, Two-photon-absorbed near-infrared photopolymerization for three-dimensional microfabrication, *J. Microelectromech. Syst.*, **7**(4), 411-415, (1998).

15) S. Kaweta, H.-B. Sun, T. Tanaka, K. Takada, Finer features for functional microdevices, *Nature*, **412**, 697-698, (2001).

16) J.A. Rogers, R.J. Jackman, G.M. Whitesides, Constructing single- and multiple-helical microcoils and characterizing their performance as components of microinductors and microelectromagnets, *J. Microelectromech. Syst.*, **6**(3), 184-191, (1997).

17) W.R. Davis, R.J. Slawson, G.R. Rigby, An unusual form of carbon, *Nature*, **171**, 756, (1953).

18) L. Holland, The effect of vapour incidence on the structure of evaporated aluminum films, *J. Opt. Soc. Am.*, **43**(5), 376-380, (1953).

19) N.O. Young, J. Kowal, Optically active fluorite films, *Nature*, **183**, 104-105, (1959).

20) T. Motohiro, Y. Taga, Thin film retardation plate by oblique deposition, *Appl. Opt.*, **28**(13), 2466-2482, (1989).

21) D.O. Smith, Anisotropy in permalloy films, *J. Appl. Phys.*, **30**(4), 264S-265S, (1959).

22) D.O. Smith, M.S. Cohen, G.P. Weiss, Oblique-incidence anisotropy in evaporated permalloy films, *J. Appl. Phys.*, **31**(10), 1755-1762, (1960).

23) M.S. Cohen, Anisotropy in permalloy films evaporated at grazing incidence, *J. Appl. Phys.*, **32**(3), 87S-88S, (1961).

24) T.G. Knorr, R.W. Hoffman, Dependence of geometric magnetic anisotropy in thin iron films, *Phys. Rev.*, **113**(4), 1039-1046, (1959).

25) E.W. Pugh, E.L. Boyd, J.R. Freedman, Angle-of-incidence anisotropy in evaporated nickel-iron films, *IBM J.*, **4**, 163-172, (1960).

26) K. Robbie, Glancing angle deposition, Ph.D. Thesis, University of Alberta, (1998).

27) I.J. Hodgkinson, Q.H. Wu, Inorganic chiral optical materials, *Adv. Mater.*, **13**(12-13), 889-897, (2001).

28) A. Lakhtakia, Axial loading of a chiral sculptured thin film, *Modelling Simul. Mater. Sci. Eng.*, **8**, 677-686, (2000).

29) A. Lakhtakia, Axial excitation of tightly interlaced chiral sculptured thin films: "averaged" circular Bragg phenomenon, *Optik*, **112**(3), 119-124, (2001).

30) M. Malac, R.F. Egerton, Observations of the microscopic growth mechanism of pillars and helices formed by glancing-angle thing-film deposition, *J. Vac. Sci. Technol. A*, **19**(1), 158-166, (2001).

31) M. Malac, R.F. Egerton, Thin-film regular-array structures with 10-100 nm repeat distance, *Nanotechnology*, **12**(1), 11-13, (2001).

32) F. Liu, C. Yu, L. Shen, J. Barnard, G.J. Mankey, The magnetic properties of cobalt films produced by glancing angle deposition, *IEEE Trans. Magn.*, **36**(5), 2939-2941, (2000).

33) F. Liu, M.T. Umlor, L. Shen, J. Weston, W. Eads, J.A. Barnard, G.J. Mankey, The growth of nanoscale structured iron films by glancing angle deposition, *J. Appl. Phys.*, **85**(8), 5486-5488, (1999).

34) M. Suzuki, Y. Taga, Integrated sculptured thin films, *Jpn. J. Appl. Phys.*, **40**, L358-L359, (2001).

35) M. Suzuki, Y. Taga, Numerical study of the effective surface area of obliquely deposited thin films, *J. Appl. Phys.*, **90**(11), 5599-5605, (2001).

36) J.G. Fish, Deposition Technologies for Films and Coatings, p. 509, (Noyes Publications, 1982).

37) H.K. Pulker, Coatings on Glass, (Elsevier, 1984).

38) J.L. Vossen, W. Kern, Thin Film Processes, (Academic Press, 1978).

39) E.B. Graper, Handbook of Thin Film Process Technology, pp. A1.2:1-A1.2:12, (1995).

40) J.F. O'Hanlon, A User's Guide to Vacuum Technology, pp. 9-10, 356, (John Wiley and Sons, Inc., 1980).

41) M. Ohring, The Materials Science of Thin Films, pp. 263-264, (Academic Press, 1992).

42) P. Ball, Made To Measure, (Princton University Press, 1997).

43) L. Abelmann, C. Lodder, Oblique deposition and surface diffusion, *Thin Solid Films*, **305**, 1-21, (1997).

44) L. Maissel, R. Glang, Handbook of Thin Film Technology, (McGraw-Hill Book Company, 1983).

45) M. Harsdorff, Heterogeneous nucleation and growth of thin films, *Thin Solid Films*, **90**, 1-14, (1982).

46) R.N. Tait, S.K. Dew, T. Smy, M.J. Brett, Density variations of tungsten films sputtered over topography, *J. Appl. Phys.*, **70**(8), 4295-4300, (1991).

47) K. Robbie, M.J. Brett, Method of depositing shadow sculpted thin films, U.S. Patent No. 5,866,204, (1999).

48) J.M. Nieuwenhuizen, H.B. Haanstra, Microfractography of thin films, *Philips Tech. Rev.*, **27**, 87-91, (1966).

49) R. N. Tait, T. Smy, M.J. Brett, Modelling and characterization of columnar growth in evaporated films, *Thin Solid Films*, **226**, 196-201, (1993).

50) A.G. Dirks, H.J. Leamy, Columnar microstructure in vapor-deposited thin films, *Thin Solid Films*, **47**, 219-233, (1977).

51) K. Robbie, J.C. Sit, M.J. Brett, Advanced techniques for glancing angle deposition, *J. Vac. Sci. Technol. B*, **16**(3), 1115-1122, (1998).

52) K. Robbie, L.J. Friedrich, S.K. Dew, T. Smy, M.J. Brett, Fabrication of thin films with highly porous microstructures, *J. Vac. Sci. Technol. A*, **13**(3), 1032-1035, (1995).

53) K. Robbie, M.J. Brett, First thin film realization of a helicoidal bianisotropic medium, *J. Vac. Sci. Technol. A*, **13**(6), 2991-2993, (1995).

54) K. Robbie, C. Shafai, M.J. Brett, Thin films with nanometer-scale pillar microstructure, *J. Mater. Res.*, **14**(7), 3158-3163, (1999).

55) K. Robbie, M.J. Brett, Sculptured thin films and glancing angle deposition: growth mechanics and applications, *J. Vac. Sci. Technol. A*, **15**(3), 1460-1465, (1997).

Chapter Two

Column Angle Variations in Chevron Thin Films

2.1 – Chevron Column Angle Variations

The relationship between the deposition angle, α, measured from the surface normal, and the column angle (or rise angle) in the resulting thin films, β, (see Figure 1.5) was first addressed by Nieuwenhuizen and Haanstra.[1] In their work, an empirical formula known as the tangent rule was developed which related the two quantities in columnar thin films deposited at oblique incidence:

$$2 \tan(\beta) = \tan(\alpha) \qquad (2.1)$$

By this expression, the column angle is always less than (or equal to) the angle of incidence, and a good agreement between predicted and physical column angles is maintained for incidence below approximately $\alpha = 70°$. At more oblique incidence angles, however, the equation is less reliable, and the predicted column inclinations are consistently greater than those observed in real films. In an attempt to address this issue, Tait, et al., employed geometrical arguments to develop a theoretically derived formula for the column angle which was valid at glancing incidence:[2]

$$2 \sin(\alpha - \beta) = 1 - \cos(\alpha) \qquad (2.2)$$

This equation is more successful in predicting the column angle of columnar thin films deposited at highly oblique angles (such as occur during GLAD), but discrepancies arise at angles nearer the normal. It must also be noted that Tait's rule is based entirely upon geometrical arguments, and no distinction is made between atoms of different materials. In addition, surface mobility, substrate temperature, residual gas pressure, and the conservation of parallel momentum have not been considered,[3-5] and as a result, the strong differences in column angles that are observed for various evaporated species cannot be accounted for. Neither rule is entirely accurate over the entire range of materials and incident angles, but in combination, the two formulas are reasonably reliable in predicting differences in the column angles of obliquely deposited thin films of any given material. As was shown by other scientists, the regions of validity for the two equations overlap somewhat,[2] but for the purposes of this thesis, I will use the tangent rule below $\alpha = 70°$ and Tait's rule for all other values of α.

It was long assumed that these equations were valid for all types of columnar thin films grown at oblique incidence, including those with the chevron microstructure. A closer examination of the geometry of the situation, however, proves this to be untrue. After one chevron arm has been deposited and the substrate rotated 180°, the growing surface (i.e., that surface onto which adatoms are incident) is no longer parallel to the substrate, but instead it is inclined at angle of (90° - β_1). (See Figure 2.1 for an illustration of the angles involved.) Consequently, with respect to this new surface normal, the flux appears to be arriving at a less oblique angle, and both the tangent and Tait's rule predictions based on a flat substrate are invalid.

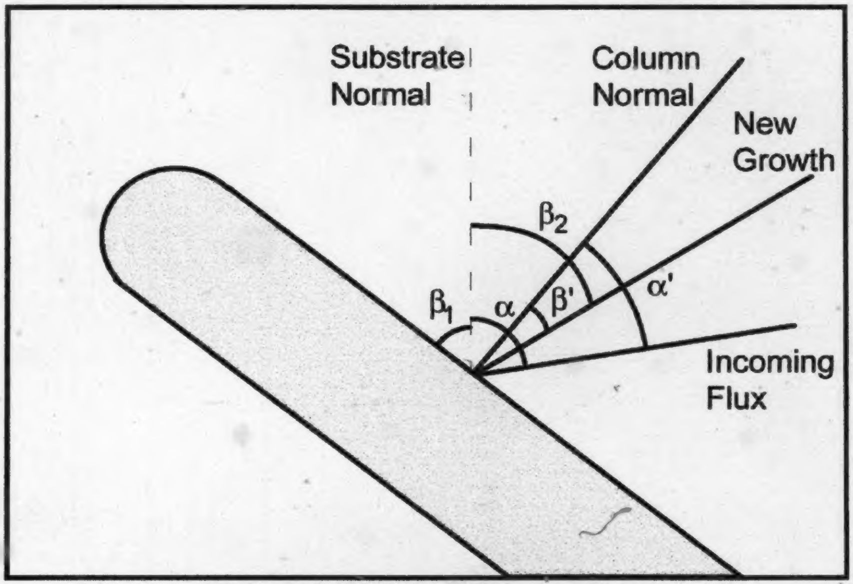

Figure 2.1 – Definition of column angles.

The importance of this effect can be seen in Figure 2.2. In the first image (Figure 2.2a), a yttria stabilized zirconia (YSZ) thin film consisting of four chevron arms is pictured. Each arm was deposited at a fixed incidence angle of $\alpha = 85°$ to approximately 3.2μm in thickness. In total, the film is nearly 13μm thick. In Figure 2.2b, a similar, four-arm chevron thin film is depicted which was also deposited at $\alpha = 85°$. In this case, the material is SiO_2, and the chevron arms are 350nm, 330nm, 360nm and 340nm in thickness for a total of 1.4μm. With a close inspection of either image, it may be observed that the second chevron arm is inclined at a greater angle than the first. For applications such as optical retardation plates, however, column angle variations are detrimental to device performance, and a strict adherence to one angle, β, must be maintained.[6,7]

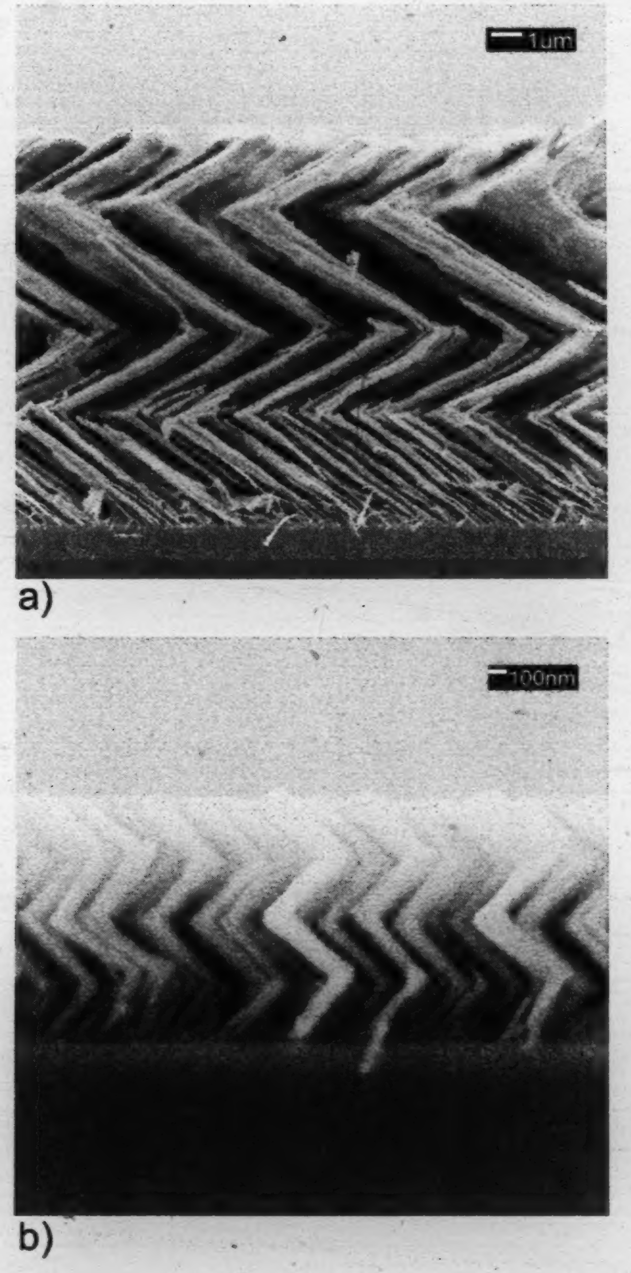

Figure 2.2 – SEM images of chevron thin films. YSZ and SiO_2 chevron films are shown in (a) and (b) respectively. Both films were deposited with constant incidence angles of $\alpha = 85°$.

In order to explicitly quantify this effect, the images under study were first divided into a number of individual files, each being composed of the pixels from a single chevron arm. The files were then converted to binary images using thresholding software and smoothing filters. To illustrate the match between the binary and greyscale figures, a binary image corresponding to the second chevron arm of Figure 2.2a has been included as Figure 2.3. The features evident in the original SEM image are also visible in the binary image, and thus one can be reasonably confident that the image processing does not significantly distort the angle data contained within the image.

Figure 2.3 – Binary image of a single chevron arm. This image corresponds to the second chevron arm of the thin film shown in Figure 2.2a. A close match between the characteristics evident in the structure of the SEM image and this binary image has been maintained.

To calculate the column angles, the technique of Sikkens, et al., was employed, and the column orientation function, F(θ), was defined as shown below:[8]

$$F(\theta)=\frac{\cos^2(\theta)}{\rho(1-\rho)D^2}\int_0^L \left\{\int_0^{D/\cos\theta}\left[\rho(x,y)-\rho\right]dy\right\}^2 dx \qquad (2.3)$$

In the equation, x and y are the coordinates of a pixel in the binary image, L and D are the spatial extents of the image, ρ(x,y) is the point density (0 or 1) of a pixel located at (x,y), ρ is the average point density of the image, and θ is an angle measured from the surface normal. A film with columns strongly oriented at an angle β will show a maximum in the column orientation function F(θ) when θ = β.[8,9] Plots of F(θ) for each of the binary images under investigation are included as Figure 2.4 and Figure 2.5. The curves in Figure 2.4 correspond to the film of Figure 2.2a, and the curves in Figure 2.5 are associated with the film of Figure 2.2b. In both cases, the column angle of the second chevron arm is significantly greater than that of the first arm. In Figure 2.2a, the first and second arms are oriented at angles of respectively 53° and 61° from the surface normal (an 8° difference), and in the film of Figure 2.2b, the angles are 36° and 44° (also an 8° difference). In a number of other films, similar behavior has been observed.

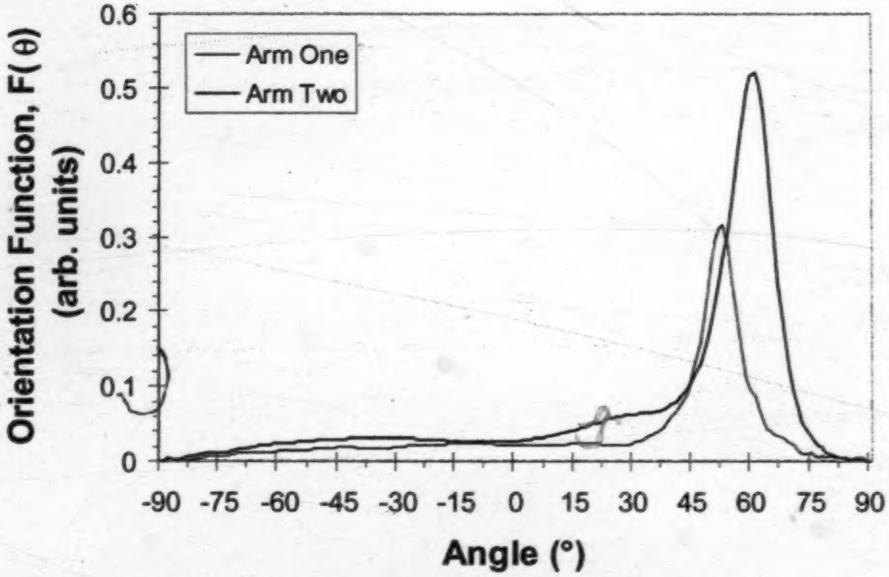

Figure 2.4 – Column orientation function plots for the YSZ film. F(θ) is plotted for the first two chevron arms of the YSZ film shown in Figure 2.2a. The peak for the first chevron arm (red line) occurs at 53°, while that of the second arm (blue line) occurs at 61°.

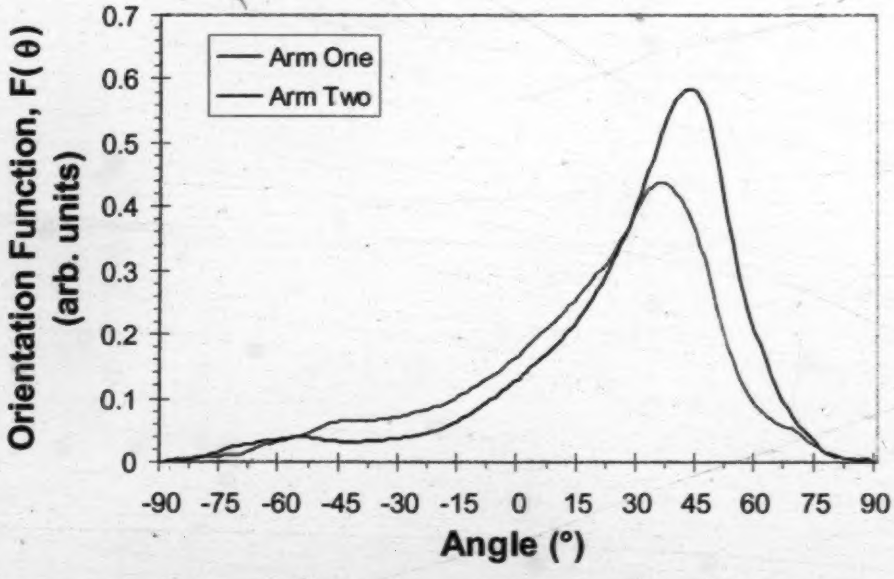

Figure 2.5 –Column orientation function plots for the SiO_2 film. F(θ) is plotted for the first two chevron arms of the SiO_2 film shown in Figure 2.2b. The peak for the first chevron arm (red line) occurs at 36°, while that of the second arm (blue line) occurs at 44°.

2.2 – Theoretical Considerations

To understand this phenomenon theoretically, the growth of each arm of a chevron thin film must be considered independently. After each 180° rotation, however, the orientation of the growing surface shifts, and one is forced to redefine the coordinate system. In this treatment, we will utilize the following notation: the angle of incidence (with respect to the substrate) will be denoted α, the effective angle of incidence for the n^{th} chevron arm (measured with respect to the column normal of the $(n-1)^{th}$ chevron arm) will be denoted α'_n, the column angle (with respect to the substrate) of the n^{th} arm of a chevron film will be denoted β_n, and the orientation of the n^{th} chevron arm (measured with respect to the column normal of the $(n-1)^{th}$ chevron arm) will be denoted β'_n. The conceptual diagram provided in Figure 2.1 may be a useful aid in visualizing the various coordinate systems that are discussed.

During the fabrication of the first arm of a chevron film at highly oblique incidence, the evaporation may be considered in the same fashion as a simple columnar thin film deposited at glancing incidence. Thus, assuming angles of incidence greater than $\alpha = 70°$, Tait's rule in its basic form suffices:

$$\beta_1 = \alpha - \sin^{-1}\left[\left(1-\cos(\alpha)\right)/2\right] \qquad (2.4)$$

At the first chevron transition, the math is eased with a rotation into the column normal reference frame:

$$\alpha'_2 = \alpha + \beta_1 - 90^\circ \qquad (2.5)$$

$$\beta'_2 = \beta_2 + \beta_1 - 90^\circ \qquad (2.6)$$

And because the deposition angle is significantly less oblique at the second arm in the new reference frame, the tangent rule is now more appropriate:

$$\beta'_2 = \tan^{-1}\left(\frac{\tan(\alpha'_2)}{2}\right) \qquad (2.7)$$

And, by combining (2.5), (2.6) and (2.7), we see:

$$\beta_2 = \tan^{-1}\left(\frac{\tan(\alpha + \beta_1 - 90^\circ)}{2}\right) - \beta_1 + 90^\circ \qquad (2.8)$$

The behavior of equations (2.4) and (2.8) with variations in α is plotted as Figure 2.6, and in the curves, it can be seen that for all values of β_1 permitted by Tait's rule the second column angle is always greater than the first.

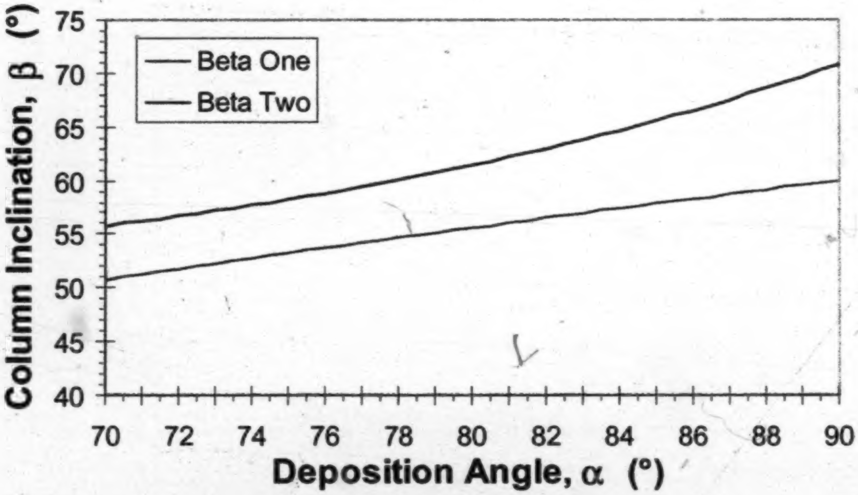

Figure 2.6 – Theoretical behavior of β_2 and β_1 with changes in α. By the theory developed above, the angle β_2 (blue line) is consistently greater than the angle β_1 (red line).

From the data, however, one weakness in the theory is apparent: equation (2.8) consistently overestimates the inclination of the second chevron arm. This deficiency may be partially accounted for in the fact that the second deposition does not occur entirely upon the "back" of the first chevron arm, but in reality, spreads to the rounded tip of the column as well. Here, the column normal is inclined by a lesser angle with respect to the substrate, and growth will occur at a less oblique angle. Thus, in reality, the entire growing surface should be considered, and some weighted average (or effective) column inclination, β_1, should be used in the calculation of β_2. The growing surface plays a second important role as well: at less oblique deposition angles, the microstructure is less porous, and a reduced fraction of the "back" of the column is accessible to incoming flux. Therefore, the growing surface is shifted towards the top of the column, and the theory developed above becomes less accurate. As a result, the region of validity is reduced to those deposition angles where the interior of the film is accessible after every chevron transition, i.e., those angles greater than about $\alpha = 70°$.

If equations (2.4), (2.5), (2.6), and (2.7) are combined, and the problem with the definition of the growing surface is ignored, we can arrive at an expression for the inclination of the second chevron arm, β_2, solely in terms of the deposition angle, α:

$$\beta_2 = 90° - \alpha + \sin^{-1}\left[\frac{1-\cos(\alpha)}{2}\right] + \tan^{-1}\left[\frac{\tan(2\alpha - 90^{\circ} - \sin^{-1}[(1-\cos(\alpha)/2)]}{2}\right] \tag{2.9}$$

If three or more chevron arms are to be considered, the expression becomes increasingly complex, and under these circumstances, it is more useful to develop, from (2.5), (2.6) and (2.7), a recursive formula for β_n:

$$\beta_n = \tan^{-1}\left(\frac{\tan(\alpha + \beta_{n-1} - 90^{\circ})}{2}\right) - \beta_{n-1} + 90^{\circ} \tag{2.10}$$

Arbitrarily choosing $\alpha = 85°$, this relation can be applied for every $n > 1$, while Tait's rule is used for $n = 1$ (this assumes the angle of incidence is sufficiently oblique, and the substrate is flat), and we can calculate that: $\beta_1 = 57.8°$, $\beta_2 = 65.6°$, $\beta_3 = 66.0°$, $\beta_4 = 66.1°$, $\beta_5 = 66.1°$, and so on. In no case is the variation in column angle as severe as in the 8° step between the first and second arms, and furthermore, each consecutive variation is less drastic than the preceding one. For every deposition angle α, similar behavior is mathematically predicted, and the column angle, β_n, appears to asymptotically approach some equilibrium value. In Figure 2.7, this behavior is plotted.

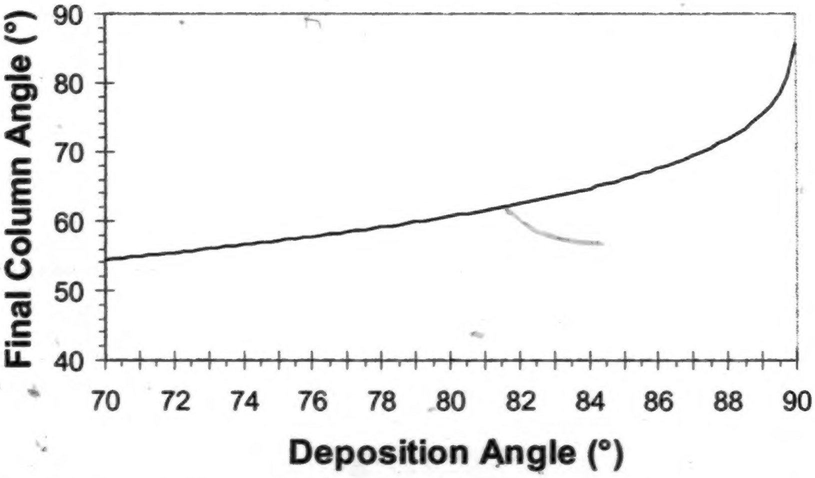

Figure 2.7 – Theoretical behavior of the ultimate column angle (β_∞). Using the recursive formula for β_n, the column angles of a chevron thin film are shown to asymptotically approach an equilibrium value. As the incidence angle, α, increases, the ultimate column angle, β_∞, increases as shown above.

In some situations (such as the optical retardation plates mentioned earlier),[6,7] column angle variations cannot be tolerated. In order to meet this contraint, one must compensate for the inclination in the growing surface by adjusting α after the first chevron arm has been deposited. For example, if the original deposition angle is 85°, Tait's law predicts a column inclination, β_1, of 57.8°. Thereafter, to maintain this column angle throughout the rest of the film, α must be reduced to 76°. (This angle is calculated in a rearrangement of equation (2.10).)

2.3 – Chevron Thin Film Simulations

In order to further validate these observations, a number of simulated thin films deposited using the 3D-FILMS simulation program were also considered.[10] The 3D-FILMS program uses a three dimensional ballistic deposition process to model the growth of three dimensional microstructures. A large number of identical growth units representing the statistically averaged behavior and position of a number of atoms (typically 1000) are launched from points slightly above a virtual substrate. The growth units follow straight-line trajectories until they strike either the substrate or the growing film, at which point, the particles are incorporated at positions based on a minimization of surface curvature and chemical potential. By this method, a three dimensional array of cubes is created, theoretically having the microstructure of an actual physical film grown under the same conditions. For example, films simulated with cubes arriving at a fixed angle with respect to the substrate normal, but from a continuously rotating direction, appear helical. The 3D-FILMS simulator was developed by T. Smy of Carleton University.

Virtual chevron thin films were deposited on flat substrates over a considerable range of growth parameters. Deposition angles from $\alpha = 80°$ to $\alpha = 87°$, various atomic diffusion lengths, and various incident flux angular distributions were all utilized, and the resulting films were examined. In all the relevant cases, the Sikkens autocorrelation method as described above was applied to the simulated chevron films. For example, in the case of a thin film grown at $\alpha = 80°$ with a surface mobility of 3nm, a 90° grain boundary grooving angle,[11,12] and an incident flux angular distribution of 2°, the angles β_1 and β_2 were respectively 48° and 55°, for a difference of 7°. As before, the second chevron arm is inclined at an angle significantly greater than the first. Because of the wide variety of growth conditions which were simulated (some of which very likely represent unphysical quantities), not all of the simulations showed such close agreement with theoretically predicted column angles or values measured for real films. In not a single case, however, was the measured angle β_2 less than that of β_1, and thus, considerable weight is lent to the observations recorded for the real films.

Sections of this chapter have been reprinted with permission from K.D. Harris, D.W. Vick, T. Smy, M.J. Brett, "Column angle variations in chevron thin films", *J. Vac. Sci. Technol. A*, **20**(6), 2062-2067, (2002).

References

1) J.M. Nieuwenhuizen, H.B. Haanstra, Microfractography of thin films, *Philips Tech. Rev.*, **27**, 87-91, (1966).

2) R.N. Tait, T. Smy, M.J. Brett, Modelling and characterization of columnar growth in evaporated films, *Thin Solid Films*, **226**, 196-201, (1993).

3) L. Abelmann, C. Lodder, Oblique evaporation and surface diffusion, *Thin Solid Films*, **305**, 1-21, (1997).

4) A. Van der Drift, Evolutionary selection, a principle governing growth orientation in vapour-deposited layers, *Philips Res. Repts.*, **22**, 267-288, (1967).

5) N.G. Nakhodin, A.I. Shaldervan, Effect of vapour incidence angles on profile and properties of condensed films, *Thin Solid Films*, **10**, 109-122, (1972).

6) T. Motohiro, Y. Taga, Thin film retardation plate by oblique deposition, *Appl. Opt.*, **28**(13), 2466-2482, (1989).

7) I. Hodgkinson, A. Lakhtakia, On the Motohiro-Taga interface for biaxial columnar media, *Opt. Eng.*, **37**(12), 3268-3271, (1998).

8) M. Sikkens, I.J. Hodgkinson, F. Horowitz, H.A. Macleod, J.J. Wharton, Computer simulation of thin film growth: applying the results to optical coatings, *Opt. Eng.*, **25**(1), 142-147, (1986).

9) M.J. Brett, Structural transitions in ballistic aggregation simulation of thin-film growth, *J. Vac. Sci. Technol. A*, **6**(3), 1749-1751, (1988).

10) T. Smy, D. Vick, M.J. Brett, A.T. Wu, J.C. Sit, K.D. Harris, Three-dimensional simulation of film microstructure produced by glancing angle deposition, *J. Vac. Sci. Technol. A,* **18**(5), 2507-2512, (2000).

11) W.W. Mullins, Theory of thermal grooving, *J. Appl. Phys.*, **28**, 333-339, (1957).

12) L.J. Friedrich, S.K. Dew, M.J. Brett, T. Smy, A simulation study of copper reflow characteristics in vias, *IEEE Trans. Semicond. Manuf.*, **12**(3), 353-365, (1999).

13) K.D. Harris, D.W. Vick, T. Smy, M.J. Brett, Column angle variations in chevron thin films, *J. Vac. Sci. Technol. A*, **20**(6), 2062-2067, (2002).

Chapter Three

Advanced Processing with Glancing Angle Deposition

3.1 – The Development of GLAD Technology

The framework of the GLAD technique was developed between 1994 and 1998 by K. Robbie and M.J. Brett.[1] All of the basic microstructures (helical, chevron, post and cap) were first produced in this period, and increasingly versatile versions of the control software were periodically written. By 1998, a procedure had been developed, whereby desirable parameters were input into a controller, and stepper motors executed all the complex motions which were required. However, limitations remained. Only the basic set of microstructures, for instance, were programmed into the software, only single material depositions had been attempted, and predominantly single layer porous films had been produced. The technology was incomplete, and additional development was required. In this chapter, I present work directed toward these deficiencies. Multilayered thin films, variable composition films and a new, adhesion-promoting microstructure are all presented, and in addition, a valuable process for patterning GLAD thin films by photolithography is described.

3.2 – The Graded Density Microstructure

It has been previously shown that the fabrication of GLAD structures is only possible because nuclei shadow their surroundings and confine the incorporation of new particles to restricted regions on their surfaces. After the isolated growth conditions are established, individual nuclei begin to compete with one another, and dominant columns emerge while others are completely extinguished. As such, in SEM images of GLAD thin films, it is common to observe a gradual broadening of the tallest columns as they grow outwards from the substrate, while at the interface, where most of the competition occurs, the columns remain relatively thin. Furthermore, several columns are usually present at the substrate for every column which has grown to the full film thickness. In consequence, one is forced to deal with the unfortunate property that both the average column diameter and the film density are not necessarily constant throughout the thickness of the film.[2]

The major disadvantages arising as a result of non-homogeneous growth are uncontrolled variations in the refractive index, optical scattering from extinguished columns within the film, and the inability of the structures to withstand laterally directed mechanical forces. Optically, scattering at the base is the greatest problem, and a significant portion of light signals incident upon GLAD films is dispersed by diffuse reflections from sub-surface columns. Mechanically, the large aspect ratio (and therefore, the long moment arm) of GLAD structures tends to concentrate transverse forces applied near the column tips to positions near the relatively weak bases.

As a potential solution, a transition layer between the dense substrate and the porous GLAD film may be proposed. The density of the layer is 100% at the film/substrate interface and, thereafter, decreases slowly at positions increasingly distant from the substrate. Near the top of the transition layer, the density matches that of the GLAD film located above it. Columns in such a configuration evolve slowly from the dense underlayer, rather than appearing suddenly at the substrate/film interface.

In practice, films of this type are realized by initiating a deposition at some small deposition angle, and then slowly increasing α until the angle corresponding to the intended porosity value is reached. At this point, any desired GLAD film may be deposited above the transition layer. In Figures 3.1a and 3.1b, two SiO_2 films which were grown by this technique are depicted. In the first, the transition layer was initiated at $\alpha = 35°$ and was increased to 85° during ten full turns in ϕ. Above the transition layer is a standard helical film of 2.5 turns and 290nm helical pitch, bringing the total film thickness to 1.05μm. In Figure 3.1b is a similar film of SiO_2 viewed from a less oblique angle. The film was initiated at $\alpha = 30°$ and evolved to $\alpha = 87°$ while undergoing 15 complete turns in ϕ. Above the transition layer, a 2 turn helical film of pitch 230nm was deposited by the standard technique, leaving a film 910nm in thickness. In both cases, the transition layer is sufficiently effective that it is difficult to discern the point where it ends and the helical film begins. From the images, it is immediately apparent that some alleviation of the problems with thin column bases has been achieved. In Figures 3.1a and 3.1b, the column thicknesses are respectively ~90nm and ~75nm at their thinnest, whereas in more typical helical films (ex., Figure 1.10b) the column diameter may be as small as 25nm near the substrate. In addition, fewer columns which appear in the transition layer fail to continue growing to the full thickness of the film.

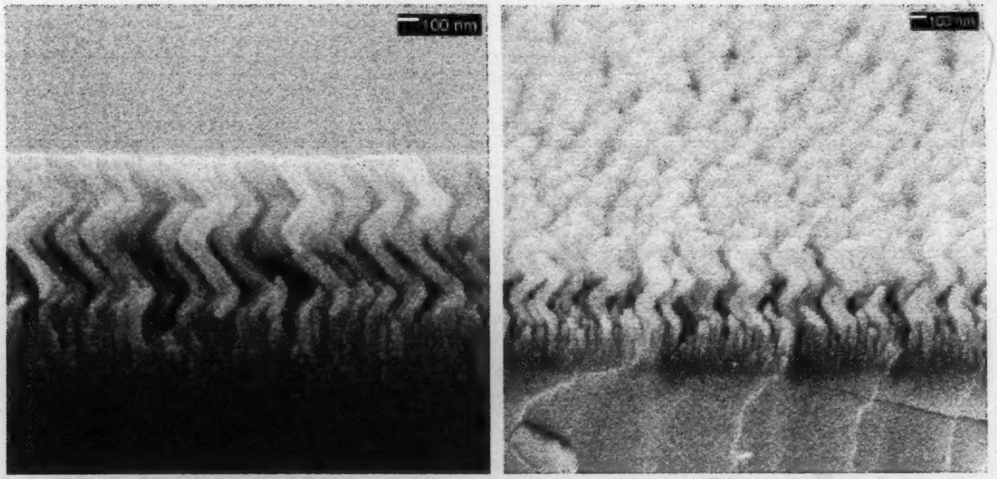

(a) (b)

Figure 3.1 – The graded density microstructure. To gradually reduce the density of a thin film, the angle α may slowly be increased during a deposition. As the deposition progresses, the film evolves from low porosity to GLAD-like structure. Typical results are shown in these two SiO_2 samples (a) and (b).

Materials strength constants are commonly expressed in terms of the maximum pressure which may be withstood before some catastrophic change takes place; for instance, the yield strength is the critical pressure which must be encountered before the onset of plastic deformation.[3] Increasing the average column diameter, as with the presence of a transition layer, distributes applied forces over a larger area, thereby reducing the applied pressure and increasing the forces necessary to exceed the film strength constants. Because force and pressure are related by area, a doubling of column diameter results in a quadrupling of the breaking force, and thus, as in the films discussed above, increasing the column diameter from 25nm to 90nm brings about nearly a thirteen-fold theoretical increase in structural strength.

A second, transition layer-based structural advantage could be incorporated in particularly troublesome GLAD films. If the adhesion between the coating and substrate is poor, the chemical composition of a transition layer may be chosen such that it acts as an adhesion promoter. For example, when attempting to deposit robust Au coatings onto Si wafers, it would be highly advantageous to provide a transition layer of Cr to prevent weak bonding between the film and wafer. This type of coating is analogous to the common industrial practice of sputtering flat Cr (or Ti) films directly onto wafers before depositing the Au layers which are intended to be patterned.[4]

3.3 – Patterning of GLAD Thin Films

3.3.1 – Photolithography: Of vital importance to the microelectronics industry is the capability of fabricating thin films that have been patterned into useful forms. When producing microelectronic components, a number of technologies are usually required in any fabrication run,[5-7] and in nearly every case, photolithographic patterning is employed at some processing stage. Because of its importance to the field, considerable research effort was devoted to repeating this process with GLAD thin films. In this section, the procedure that was found to effectively pattern GLAD layers is described in detail, and images of the films at various stages in the processing are provided.

In essence, photolithography is a six-step procedure by which selected areas of a thin film are removed from the substrate.[8] (For a more detailed description of photolithographic processing and the chemistry of photoresist, a number of in-depth references can be consulted.)[7-10] Using GLAD coatings, it was found that each processing step is conceptually identical to its counterpart in the standard technique, however, due to the highly porous nature of the films, a number of complications arise. In the text, each of these deviations is noted and granted particular attention. Since the deposition of the layers to be patterned (i.e., the GLAD films) has been well documented in Chapter 1, the discussion begins with the second processing step, i.e., the application of photoresist to the film.

3.3.2 – Photoresist application: As most standard fabrication runs deal with predominantly flat films, photoresist layers are generally formed directly above the film to be patterned. Even if there is a degree of surface roughness, a spin application of photoresist tends to planarize the corrugations in the underlayer, leaving reasonably flat photoresist for additional processing.[11-12] With a GLAD film, however, this is not the case: large pores are present between the columnar structures, and the role this plays on the spin application of photoresist was previously undetermined. The most favorable result that could reasonably be expected sees the photoresist flowing into the spaces between the microstructures,[13] leaving no voids in the composite, and completely encapsulating the columns. To be useful, the coating would also be continuous and free from cracks. Such an arrangement is suitable because it prevents the penetration of etchants into areas of the film which are intended to remain intact following the etch, i.e., because the columns are completely coated, the etchants may not pass underneath or through the photoresist layer by means of voids, or attack the column tops directly. (See Figure 3.2)

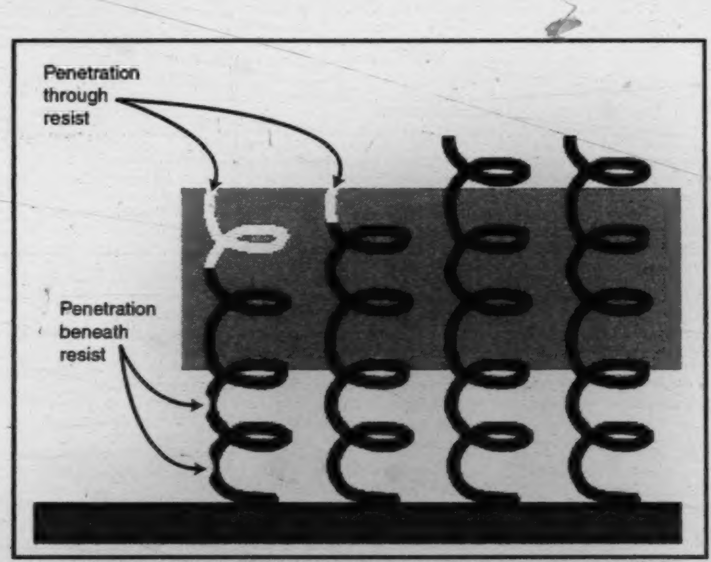

Figure 3.2 – Potential difficulties in filling GLAD films with photoresist. If photoresist does not completely encapsulate the GLAD structures, a possibility exists that etchants used in subsequent processing steps will penetrate into unintended areas. For example, if the photoresist does not reach the substrate, etchants may attack the GLAD structures from beneath the resist layer.

Two distinct types of photoresist were investigated: HPR504 from Arch Chemicals[14] and AZ5214 from Shipley Co.[15] Small volumes of these resists (<5mL) were dispersed over a number of GLAD thin films rotating at high speed, and the results of the experiments were surprisingly consistent over a range of conditions. First, the two resists tended to fill GLAD films in exactly the same manner, and SEM images of films filled with either of the two photoresists are indistinguishable. Second, the variation in photoresist thickness with changes in rotation speed is not as evident as in a typical spin coating. Usually, a greater rotation speed leads to a thinner photoresist layer,[16-17] however, in filling GLAD films with photoresist, surface tension effects play a role, and the porous films tend to be completely filled regardless of their thickness and the rotation rate. Variations in the spin speed only alter the volume of resist remaining above the helix tips. Spinning a small volume of HPR504 at 2500rpm, for instance, leaves 850nm of excess resist, and as the rotation rate increases, this thickness falls until by 5500rpm, almost no excess resist is apparent. Therefore, in choosing a suitable rotation rate, one need not be concerned with the filling aspect, but rather make the decision based upon the developer process. (i.e., only as much excess resist as will be removed by the developer should be permitted to form a cap above the plane of the film surface.) Based on this criterion, application speeds between 5000rpm and 5250rpm have been found to be optimum.

In Figure 3.3, an example of a helical film of SiO_2 is shown which has been impregnated with HPR504 while spinning at 4250rpm. In the image, it is clear that photoresist fully surrounds the helices, and no voids are readily visible in the structure. It is also important to note that the helices survived the centripetal forces which were encountered during the high speed rotation and did not become detached from the surface. As a test of the effectiveness of the photoresist encasement process, one wafer of SiO_2 helices was filled with HPR504 photoresist at 4000rpm and immersed in a solution of buffered oxide etch (a standardized etchant for SiO_2) for five minutes. Because no etching of the underlying GLAD film was discernable in subsequently acquired SEM images, it may be concluded that this filling process is effective.

3.3.3 – Pattern transferal: After applying a layer of photoresist, the intended pattern is transferred into the chemistry of the layer with UV radiation. No significant deviations from the standard photolithographic process were encountered at this stage. Emulsion masks were printed onto plastic film by Screaming Colour Inc.,[18] and affixed, printed side up, onto square glass mounts. (Some work was also done using metal film masks from Nortel Inc.)[19] In a mask aligner from AB-M Technologies,[20] the masks were vacuum pressed onto the photoresist filled wafers and illuminated with dual line (365 and 400nm) UV radiation from a mercury arc lamp. As will be shown shortly, the standard

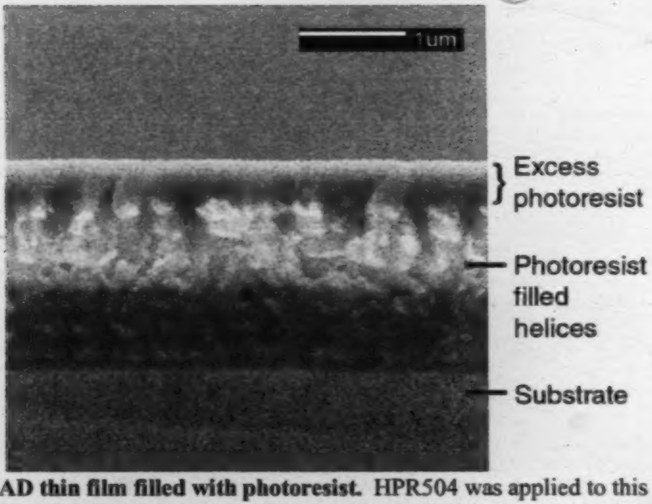

Figure 3.3 – A GLAD thin film filled with photoresist. HPR504 was applied to this film while spinning at 4250 rpm. The film has been entirely filled, and no voids are apparent in the microstructure.

process successfully transferred the mask features into the chemical structure of the photoresist layer throughout the entire thickness of the film, and therefore, no process modifications were required at this stage.

After UV illumination, the substrates were immediately immersed in a developer solution. The chemical composition of a particular developer is usually withheld by the supplier as proprietary information, but most often the developers are basic solutions based on NaOH.[21] For HPR504 photoresist, Shipley 354 Developer solution is an appropriate developer, and in the case of AZ5214 used in the negative mode, Shipley 321 Developer solution. In the example of Figure 3.4, a thin film of SiO_2 is shown which has been filled with HPR504, exposed though a mask, and immersed and agitated for 1min in 354 Developer. Following this, the UV exposed photoresist had dissolved, while the unexposed regions to the right and left remained intact. Some observations should be made: first, the edges of the developed regions are not always perfectly reproduced from the mask. In the figure below, there is a variation on the order of ±3μm in the position of each of the transitions between developed and undeveloped film. (This sample had the most uneven boundary of all those produced. Other films, such as those shown in Figure 3.5, do not show nearly this degree of non-linearity.) In the given example, the transitions remain distinct, however, if lithography were attempted on smaller dimensions a ±3μm variation could lead to a complete film removal in some regions and unintentionally wide lines in others. Second, upon the removal of the photoresist, the GLAD columns appear to have clumped together into clusters with dimensions on the order of ~1-3μm. The boundaries between these groups of helices tends to form the boundaries between developed areas and areas remaining coated in photoresist. The source of this effect is far from certain, but one potential explanation involves stress relief. As the solvents are removed from the photoresist, stress is introduced into the film, and a constriction effect takes place. In some cases, this effect occurs, and in other cases, it does not. This is not a well understood phenomenon, and was presented here only to describe some of the problems which may be encountered in future experiments.

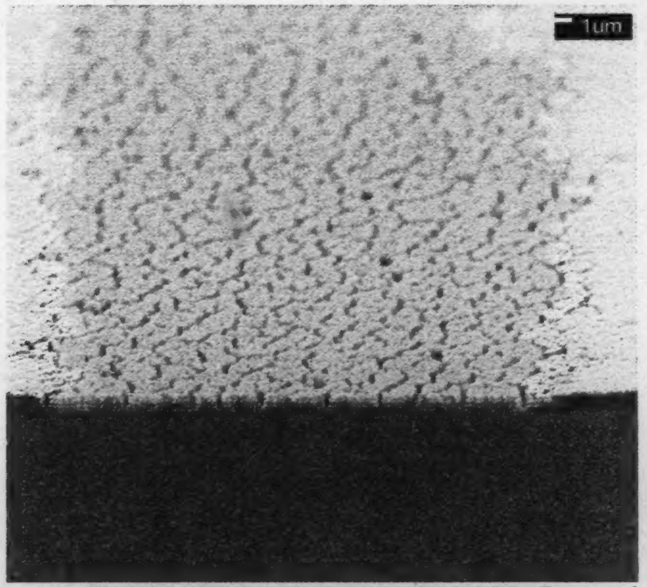

Figure 3.4 – Photoresist removed from selected areas of a GLAD film. By exposing certain areas of a photoresist filled SiO_2 GLAD film to UV light, those selected areas of resist can be removed from the wafer by immersion in a developer solution.

The unwanted GLAD structures are then removed from the substrate using an etchant appropriate to the material being patterned.[22-23] In the examples shown in Figure 3.5, SiO_2 thin films have been patterned into lines, their surroundings having been removed using 10:1 buffered oxide etchant (BOE) from Arch Chemicals. In each case, the etch time was 3 minutes, and an acetone rinse to remove the remaining photoresist immediately followed. Since the GLAD film has obviously not been entirely etched away, one can conclude that neither penetration of the etchant under nor through the resist has occurred, and that the photoresist filling process succeeded in dispersing the resist without significant voiding from the surface of the film to the substrate. Also, the surface of the substrate, previously coated in GLAD structures and photoresist, has been effectively cleaned of residue. Aside from the unetched helices themselves, nothing is visible upon the substrates. This property provides some evidence that both the UV radiation and the developer solutions penetrate the entire film from surface to substrate. Had this not been the case, smaller, subsurface columns could stay coated in resist throughout the etching process and remain undissolved in the etchant. Under those circumstances, structures extending only partially to the film surface would be in abundance over the etched substrate.

In Figure 3.5a, a patterned line of GLAD structures 4.0μm in width is shown, and in Figure 3.5b, a similar line of helical structures 2.5μm in width is shown. In more ambitious lithography experiments, the line widths could likely be reduced somewhat, however, in the limiting case, the discrete nature of the columnar structures will prevent the creation of clearly defined lines. Since particular columns may only be in one of two states, present or etched, the line edges will be, at best, rough on the scale of the combination of average column diameter and average column spacing. This is also the

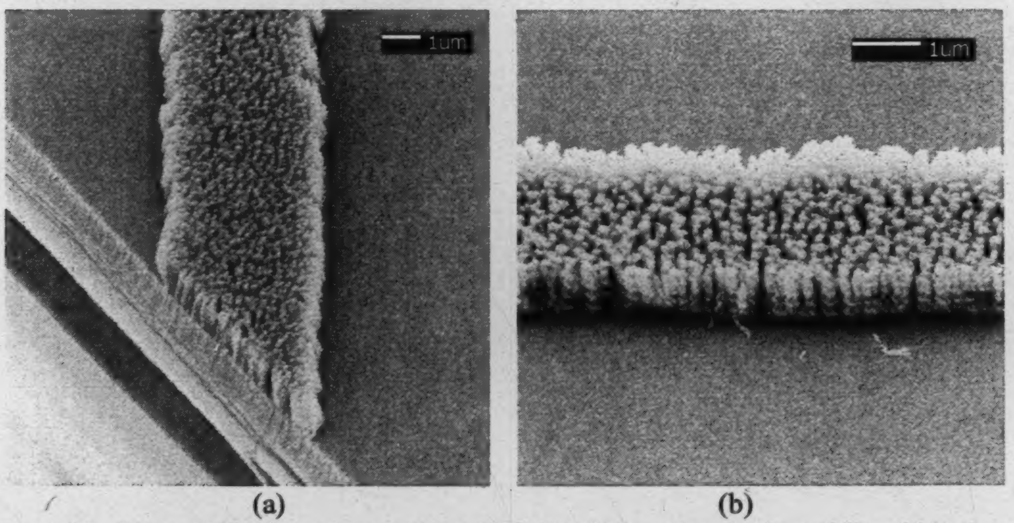

(a) (b)

Figure 3.5 – Lines of helical structures produced by photolithography. Sections of film which are not coated in photoresist after the developer stage may be removed by etching. This process leaves GLAD structures organized into useful patterns, such as the lines shown above.

ultimate limit for photolithography. In both the cases shown, the line edges are slightly jagged, with the degree of non-linearity in the range of approximately ±300nm per side. This is approximately equivalent to the average column diameter and spacing.

3.3.4 – Residual photoresist: Often, an acetone rinse is not sufficient to completely remove all photoresist from the wafer, and a thin residue clings to the top of the helical film. (An image is shown in Figure 3.6.) In some cases, this residue layer has proven to be extremely resilient, resisting both long term (>100 hours) exposure to acetone, as well as ultrasonic cleaning. Under these circumstances, more drastic removal schemes must be employed. A technique which was found to be adequate in all cases encountered to date requires the residue-fouled substrate to be immersed in a heated (120°C) solution of Shipley Microposit 1165 Remover for at least four hours. The film shown in Figure 3.5b is an example of one film treated in this manner. The residue was clearly removed, and no adverse structural effects are apparent.

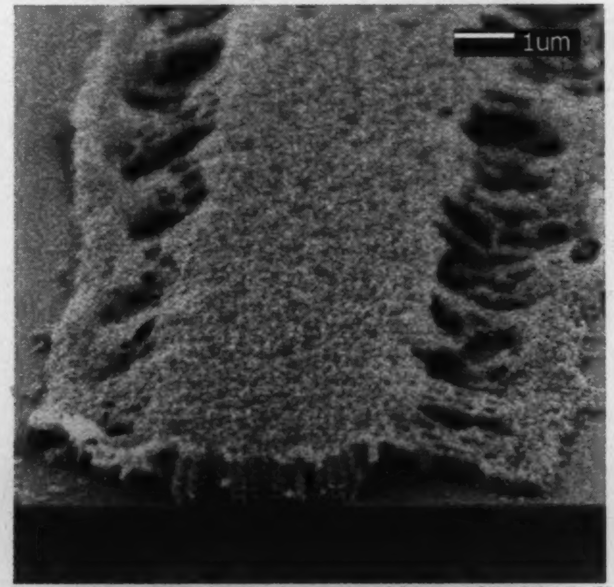

Figure 3.6 – Photoresist residue. After developing and etching an SiO_2 GLAD film, a solvent-resistant residue of photoresist or developer often clings to the film.

3.3.5 – Summary: As a summary, a recipe for effectively patterning GLAD microstructured thin films is presented in Table 3.1:

Step	Process	Description
1	Film Deposition	Deposit SiO_2 as required
2	Photoresist Fill	Spin 3mL of HPR504 into the film while rotating at 4000 rpm
3	Softbake	Heat the substrate to 115°C for 90s to remove excess solvents
4	Expose	Expose the photoresist to UV radiation through the desired mask for 4s
5	Develop	Immerse the substrate in 354 Developer for one minute, or as required
6	Etch	Immerse the substrate in BOE for three minutes, or as required to remove the film
7	Acetone Rinse	Rinse the patterned film in acetone to remove the photoresist
8	Residue Stripping	Immerse the substrate in Remover heated to 115°C for 4 hours (if required)

Table 3.1 – Steps in the patterning of SiO_2 GLAD microstructures.

3.4 – Controlled Positioning of GLAD Structures

One feature of a GLAD film which is highly advantageous is the ability to position the individual columnar microstructures onto pre-selected areas of a substrate, while leaving the interstitial areas free from column growth. The development of this process has recently been the work of B. Dick, S. Kennedy and M. Malac of the University of Alberta.[24-27] Because nucleation sites for GLAD structures appear randomly over a surface, and because competition and extinction occur regardless of surface position, no self-organization of microstructures takes place during a typical oblique deposition. To organize the structures, it is necessary to establish the shadowing conditions leading to regular growth before the deposition begins. As may be seen in Figure 3.7, the majority of obliquely incident particles strike positions on the substrate that are raised slightly above their surroundings. Since the resulting film growth is concentrated almost exclusively in the elevated areas, one is able to control the ultimate positioning of individual GLAD structures (within some reasonable bounds set by geometry, atomic diffusion, and practicality of the lithography) by controlling the layout of the substrate.

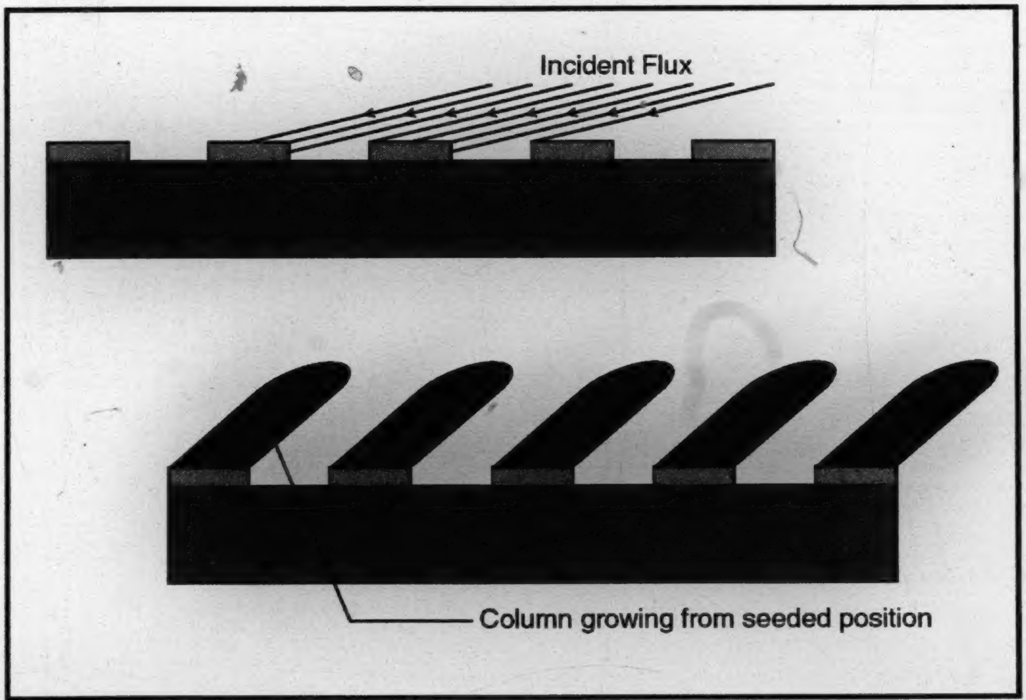

Figure 3.7 – The concept of seed layers for controlled nucleation. If a GLAD deposition occurs over a substrate that has been pre-patterned with raised areas, shadowing conditions will be in effect from the very beginning. Thus, the ultimate positioning of GLAD structures may be controlled by the layout of the substrate.

In practice, this effect is achieved with the use of substrates pre-patterned with arrangements of photoresist squares. An example of one such substrate is shown in Figure 3.8. In the figure, a silicon wafer that has been lithographically patterned with photoresist to have a square grid of raised structures separated by 1μm in the two perpendicular directions. Substrates of exactly the same specifications were used to deposit the periodic arrays of GLAD structures shown in Figure 3.9. In Figure 3.9a, a SiO_2/Cr posts structure 1.32μm in thickness stands on one array, and in Figure 3.9b, a

1.75 turn, helical SiO_2 film, 1.5µm in thickness stands on another array. Applications for the structures in (a) and (b) will be described in sections 3.5.3 and 5.3.3.

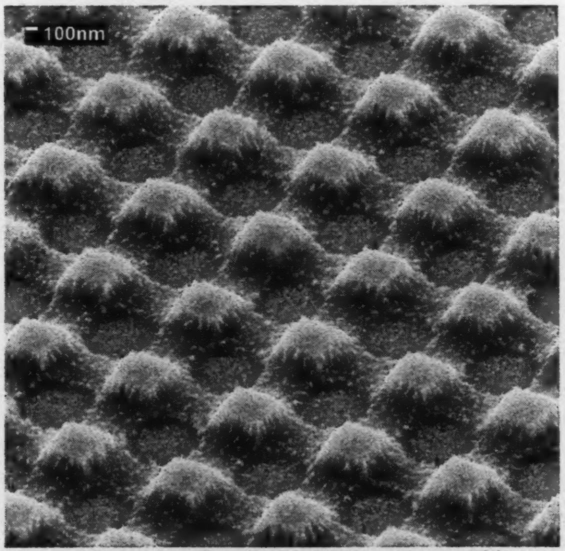

Figure 3.8 – A periodic seed layer for glancing angle deposition. This pattern of 400nm squares separated by 1µm in two dimensions was produced by standard photolithography techniques.

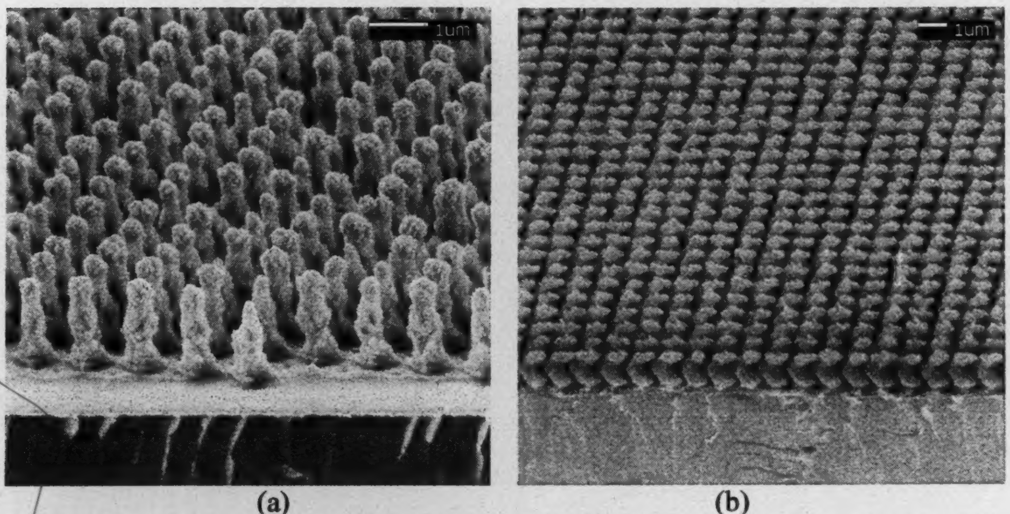

(a) (b)

Figure 3.9 – Examples of GLAD thin films deposited onto periodic arrays. In (a), posts of alternating SiO_2 and Cr deposited on a periodic array are shown, and in (b) helices of SiO_2 were deposited onto an array similar to that of Figure 3.8.

3.5 – GLAD Microstructures of Variable Composition

3.5.1 – Multi-material depositions: In the past, very little work has been done in investigating the fabrication of microstructures composed of more than one material. In a number of applications, such as semiconductor lasers[28] or thermal barrier coatings,[29] alternating patterns of two or more materials are often essential. Therefore, to show that it is possible to vary the chemical composition of a GLAD thin film, a number of thin films were deposited having typical GLAD microstructures, but being comprised of two different materials. In Figure 3.10, two examples of two such films are presented. Figure 3.10a shows a posts thin film where sources of ZrO_2 and SiO_2 have been alternated in a periodic manner throughout a deposition. Each of the eight regions (ZrO_2 being nearest the substrate) is approximately 190nm in thickness, making up a film of 1.52μm. In Figure 3.10b, we see a similar posts thin film where SiO_2 and Cr have been deposited into four bands, each approximately 330nm in thickness. In this second figure, the microstructures widen and thin as the deposition materials are switched. High mobility chromium atoms travel relatively far after impinging upon the surface, and the structure tends to broaden during Cr deposition. Silicon dioxide molecules, by contrast, have a lower mobility and are confined to a more central area of the growing column. Thus, the average column diameter oscillates as the deposition materials are alternated.

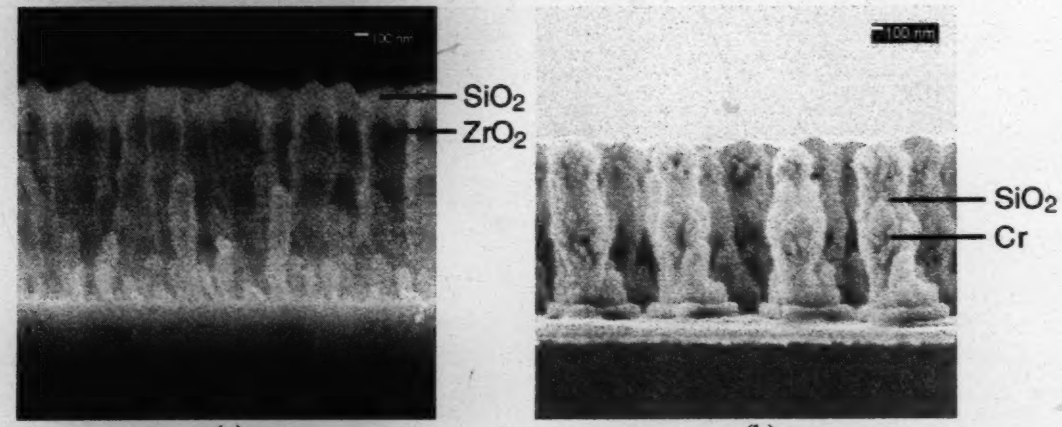

(a) (b)

Figure 3.10 – GLAD microstructures of variable composition. In (a) and (b), evaporants were exchanged during GLAD depositions. In (a), sources of ZrO_2 and SiO_2 were alternated, and in (b), sources of SiO_2 and Cr were alternated.

3.5.2 – Composition analysis: The greatest difficulty related to studying these films was providing evidence that two distinct materials were actually present in the microstructure. As a first step, the evaporants were selected such that they would yield the greatest possible atomic number contrast from an SEM,[30] while still being relatively non-toxic and simple to work with. Despite this, effective SEM contrast was difficult to attain. (See Figure 3.10.) As a second test, energy dispersive x-ray spectroscopy (EDX)[31] measurements were performed on both samples, and one of the spectra (corresponding to the film in Figure 3.10b) has been reproduced here as Figure 3.11. In the figure, peaks matching the known energies of x-rays originating from chromium and silicon atoms are clearly present and have been marked on the plot. Because chromium is the upper layer in this film, a greater proportion of the detected x-rays are from Cr rather than Si atoms. The Au peak which has been marked is the result of a (superfluous) processing step which occurred early in the fabrication of the film. The gold layer is present underneath and around each of the growing columns and was detected by the EDX technique.

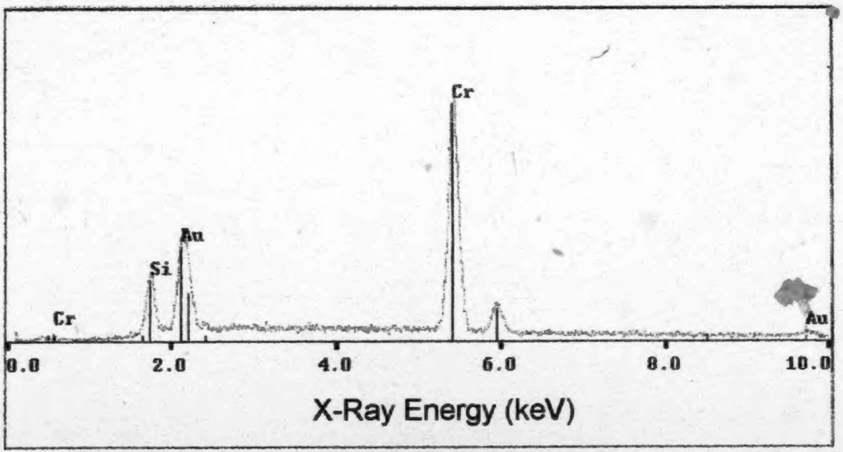

Figure 3.11 –EDX spectrum from an alternating material GLAD film. An energy dispersive x-ray spectroscopy (EDX) spectrum was gathered in a scanning electron microscope (SEM) from the sample shown in Figure 3.10b. The spectrum shows clear Cr, Au, and Si peaks.

3.5.3 – Potential applications: There is a possible application inherent in periodically alternating posts in the field of photonic bandgap (PBG) crystals.[32-34] The fabrication of a useful PBG crystal structure requires three dimensions of periodicity to be designed into a thin film microstructure. One of those periodicities (that in the direction perpendicular to the substrate) is available in a variable composition GLAD microstructure if the transitions between two evaporant materials can be controlled to a sufficient degree. The additional two periodicities may be designed into a thin film by performing the deposition onto a pre-patterned substrate, as was described in section 3.4. The film presented in Figure 3.10b is one example. The four layer thin film depicted in the image has two dimensions of 1μm periodicity parallel to the surface and an additional dimension of 660nm periodicity perpendicular to the surface.

References

1) K. Robbie, Glancing angle deposition, Ph.D. Thesis, University of Alberta, (1998).

2) K.D. Harris, M.J. Brett, T.J. Smy, C. Backhouse, Microchannel surface area enhancement using porous thin films, *J. Electrochem. Soc.*, **147**(5), 2002-2006 (2000).

3) W.D. Callister, Materials Science and Engineering: An Introduction, p. 118, (John Wiley & Sons, Inc., New York, 1994).

4) M. Ohring, Materials Science of Thin Films, p. 769, (Academic Press, San Diego, CA, 2002).

5) J.D. Plummer, M.D. Deal, P.B. Griffin, Silicon VLSI Technology, (Prentice Hall, Upper Saddle River, NJ, 2000).

6) B.G. Streetman, Solid State Electronic Devices, (Prentice Hall, Englewood Cliffs, NJ, 1995).

7) S.M. Sze, Semiconductor Devices: Physics and Technology, (John Wiley & Sons, New York, 1985).

8) M. Madou, Fundamentals of Microfabrication, (CRC Press, Boca Raton, FL, 1997).

9) L.F. Thompson, C.G. Wilson, M.J. Bowden, Introduction to Microlithography, (American Chemical Society, Washington, DC, 1994).

10) W.M. Moreau, Semiconductor Lithography, (Plenum Press, New York, 1988).

11) P. van Zant, Microchip Fabrication: A Practical Guide to Semiconductor Processing, pp. 297-302, (McGraw-Hill, New York, 2000).

12) J.D. Plummer, M.D. Deal, P.B Griffin, Silicon VLSI Technology, pp. 710-715, (Prentice Hall, Upper Saddle River, NJ, 2000).

13) M.C. Nobrega, L.C.F. Gomes, G.P. LaTorre, J.K. West, Microstructure, optical and dielectric characterization of porous gel silica impregnated with PMMA, *Mater. Charact.*, **40**, 1-5, (1998).

14) Arch Chemicals Inc., 501 Merritt 7, Norwalk, CT 06856.

15) Shipley Company L.L.C., 455 Forest Street, Marlborough, MA 01752.

16) L.F. Thompson, Introduction to Microlithography, pp. 1-17, (American Chemical Society, Washington, DC, 1994).

17) P. van Zant, Microchip Fabrication: A Practical Guide to Semiconductor Processing, p. 219, (McGraw-Hill, New York, 2000).

18) Screaming Colour Inc., 18252 102nd Avenue, Edmonton, AB T5S-1S7.

19) Nortel Networks, Photomasks Department, Nepean, ON K2H-8V4.

20) AB-Manufacturing Inc., 6280-M San Ignatio Avenue, San Jose, CA 95119.

21) P. LeBarny, Molecular Engineering of Ultrathin Polymeric Films, pp. 99-150, (Elsevier, New York, 1987).

22) P. Walker, W.H. Tarn, Handbook of Metal Etchants, (CRC Press, Boca Raton, FL, 1991).

23) J.L. Vossen, W. Kern, Thin Film Processes, (Academic Press, San Diego, CA, 1978).

24) M. Malac, R.F. Egerton, M.J. Brett, B. Dick, Fabrication of submicrometer regular arrays of pillars and helices, *J. Vac. Sci. Technol. B*, **17**(6), 2671-2674 (1999).

25) B. Dick, J.C. Sit, M.J. Brett, I.M.N. Votte, C.W.M. Bastiaansen, Embossed polymeric relief structures as a template for the growth of periodic inorganic molecules, *Nano Lett.*, **1**(2), 71-73, (2001).

26) M. Malac, R.F. Egerton, Observations of the microscopic growth mechanism of pillars and helices formed by glancing-angle thin-film deposition, *J. Vac. Sci. Technol. A*, **19**(1), 158-166, (2001).

27) B. Dick, M.J. Brett, T. Smy, M. Belov, M.R. Freeman, Periodic submicrometer structures by sputtering, *J. Vac. Sci. Technol. B*, **19**(5), 1813-1819, (2001).

28) B.E.A. Saleh, M.C. Teich, Fundamentals of Photonics, pp.636-637, (John Wiley & Sons Inc., New York, 1991).

29) E.J. Gonzalez, J.E. Bonevich, G.R. Stafford, G. White, D. Josell, Thermal transport through thin films: mirage technique measurements on aluminum/titanium multilayers, *J. Mater. Res.*, **15**(3), 764-771, (2000).

30) N. Rosenberg, C.Z. Jiang, P. Morin, Monte Carlo simulations of coaxial backscattered electrons in SEM, *Ultramicroscopy*, **76**, 97-105, (1999).

31) M. Ohring, The Materials Science of Thin Films, pp. 615-616, (Academic Press, San Diego, CA, 1992).

32) E. Yablonovich, Photonic band-gap structures, *J. Qpt. Soc. Am. B*, **10**(2), 283-295, (1993).

33) J.D. Joannopoulos, P.R. Villeneuve, S. Fan, Photonic crystals: putting a new twist on light, *Nature*, **386**, 143-149, (1997).

34) V.V. Poborchii, T. Tada, T. Kanayama, A visible-near infrared range photonic crystal made up of Si nanopillars, *Appl. Phys. Lett.*, **75**(21), 3276-3278, (1999).

Chapter Four

High Surface Area Microchannels

4.1 – The Lab-On-A-Chip Concept

Currently, much of present day molecular biology relies on capillaries, or hollow tubes having inner diameters on the order of 100μm, for chemical separations and identification of genetic material and proteins.[1] Although they play a major role in molecular biology, capillary-based systems do not lend themselves well to integration, as the devices tend to be large and expensive single function instruments.

Recently, it was shown that performance equivalent to or exceeding that of a capillary could be obtained from a microfluidic structure, in which photolithographic processes were used in fabrication.[2] The primary advantage of microfluidic chips is inherent in their size: speed is increased and cost is reduced while allowing far greater levels of integration. This has been termed the 'lab-on-a-chip' concept.[3]

A feature common to nearly all existing and conceived 'lab-on-a-chip' analytical systems is the existence of microchannels to manipulate the various fluids required on chip.[3] (An example is shown in Figure 4.1.) Often it is not merely transportation of fluids that is required of the microchannel, but the actual filtering, separation, or reactions which occur therein.[4] In many of these instances, due to a greater availability of sites, it is advantageous to operate in regions of high surface area. Numerous examples are found in the literature: on-chip liquid chromatography, for instance, requires millions of stationary phase support structures in small, sub 2μm channels.[5] In molecular imprinting, efficient separations are achieved by packing channels with many imprinted particles.[6-9] The 'Boom method' of nucleic acid purification requires a large surface area of silicon dioxide binding sites on which to hold nucleic acids,[10] and percolation filters generally require large cross-sectional areas in order to provide many parallel channels for filtration.[11]

In the past, surface area enhancement has been accomplished by packing existing microchannels with particles,[12] or by complex micromachining procedures.[5] However, with glancing angle deposition (GLAD), a new method of fabricating high surface area microchannels is available.

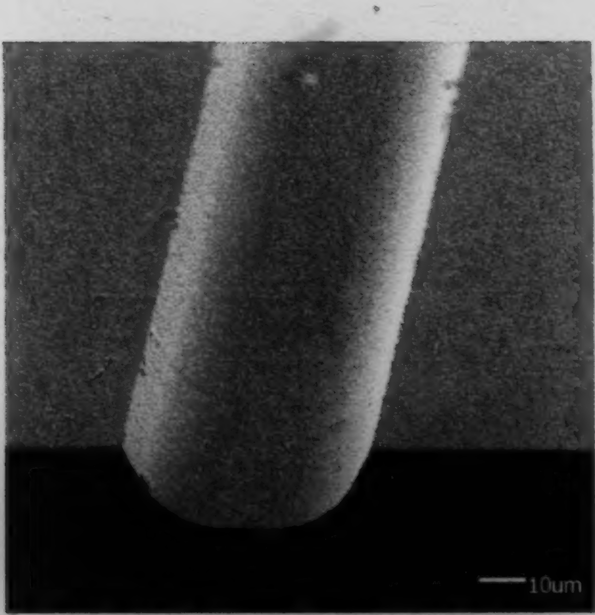

Figure 4.1 – A typical microchannel. This channel was etched into a glass slide to a depth of 18μm and a width of 52μm.

4.2 – Glancing Angle Deposition over Microchannel Topography

4.2.1 – Glancing angle depositions into microchannels: The GLAD technique was used to coat glass substrates with evaporated films of silicon dioxide. For this experiment, substrates were prepared, by lithographic methods, to include long microchannels, 4.5μm in depth and with widths of 50μm. The substrates were diced into pieces 3.5cm in length and 6mm in width, each carrying a microchannel parallel to its long axis.

The samples were positioned above a source of evaporating silicon dioxide with flux arriving at an angle of $\alpha = 85°$. In order to avoid severe shadowing from the walls of the microchannel, care was taken to ensure that the axis of the microchannels was directly lined up with the evaporation source, (see Figure 4.2).

Figure 4.3 shows SEM images of a film grown in this manner. This particular film is 4μm in thickness, reaching nearly to the top of the 4.5μm channel. On either side of the channel, small regions of slightly thinner film are visible. This is the unavoidable result of shadowing from columns growing outside (and above) the microchannel. These columns tend to hang over the edges of the channel, preventing those structures in the corners from receiving evaporant. The GLAD structures which were originally outside the microchannel have been removed by simply scraping over the channel with a sharp, flat razor blade, and some debris from this process remains visible in the images. (In the future, excess film could be removed more controllably by a photoresist liftoff process.)

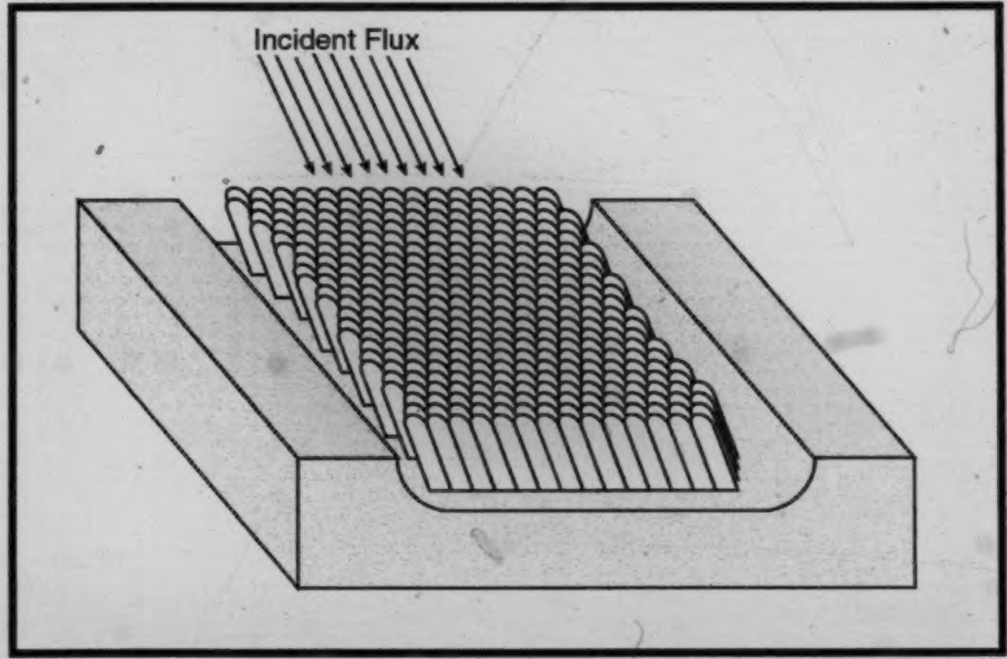

Figure 4.2 – Filling an etched microchannel by glancing angle deposition. Flux deposited at glancing incidence along the axis of a microchannel will encounter conditions similar to that of an ordinary flat surface. As a result, typical slanted post structures will be formed at the bottom of the channel.

In the figure, it may also be seen that the columns tend to form "fan" shapes. At their bases the structures are thin, however, over the course of the deposition they tend to spread out in a direction perpendicular to the incidence of flux. This anisotropy effect of deposition at highly oblique angles has been described previously,[13] and is thought to be an effect of self-shadowing.

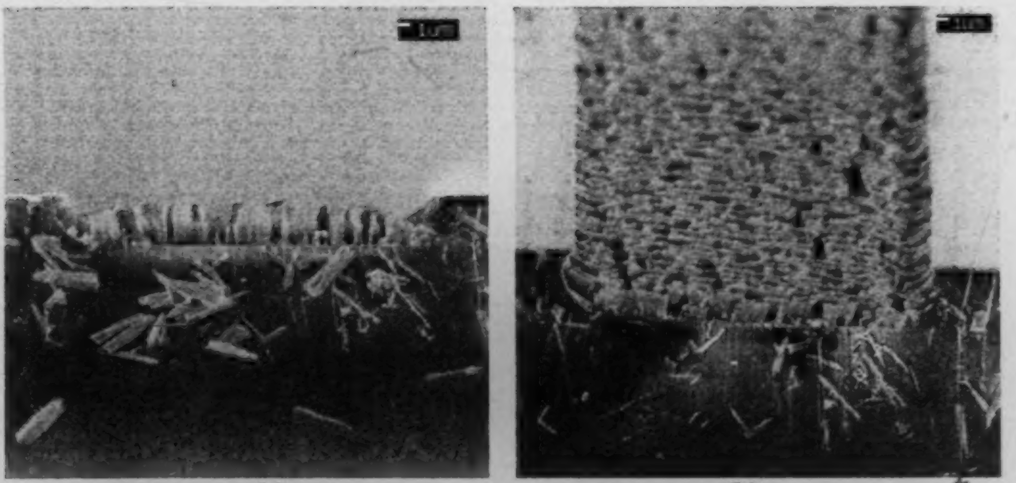

(a) (b)

Figure 4.3 – A microchannel filled with GLAD structures. By the process described in the text, the glass microchannel was filled with SiO_2 microstructures to a thickness of 4μm. The debris visible around the edges of the channel is a result of the cleaving of the substrate and would not normally be present in the film.

4.2.2 – Alignment issues: When attempting to fill microchannels by deposition at glancing incidence, shadowing from the channel walls is a severe problem. Misalignment between the axis of the microchannel and the direction of deposition leads to channels which are only partially filled. Greater deposition angles, deeper channels, and more severe misalignments all increase the fraction of the channel which is deprived of flux. In the worst case, flux arrives at glancing incidence perpendicular to the channel axis, and a large portion of the channel (subsequently denoted $s_{90°}$) lies in shadow. As the alignment improves (i.e., as the misalignment angle, γ, is reduced), the ray of atoms which just avoids the channel wall travels the same distance before striking the surface; however, it does so at an oblique angle, thereby reducing the shadowed width of the channel. In theory, at $\gamma = 0°$ no shadowing conditions whatsoever are encountered. (However, because the geometry of the PVD system introduces an angular flux distribution of approximately ±1.5°, even in a perfectly aligned system, γ is always greater than zero for some component of the incident flux.) A graphical depiction of this situation is presented in Figure 4.4. Using simple trigonometry, an equation can be developed for the width of the channel lying in the shadow of its walls, s, in terms of the channel depth, d, the angle of incidence, α, and the misalignment angle, γ. That is:

$$s = d\sin(\gamma)\tan(\alpha) \qquad (4.1)$$

The implications of this equation are as previously discussed: deep channels are difficult to fill, alignment is critical, and high angles of incidence are problematic. In addition, because most GLAD microstructures require substrate rotation during fabrication, (i.e., angles of γ not equal to 0°), the possibility of using this method to produce microchannels filled with GLAD microstructures other than simple slanted posts is precluded.

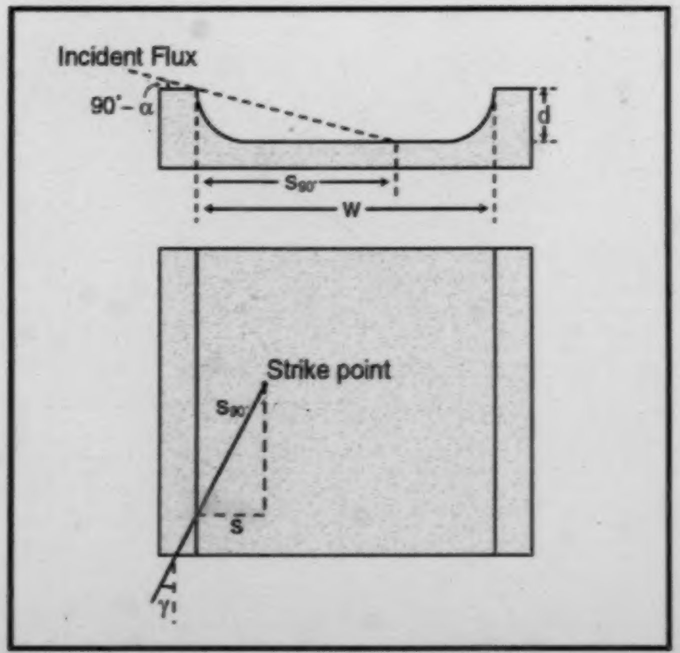

Figure 4.4 – The severity of misaligned depositions into microchannels. Any misalignment between the direction of deposition and the axis of the microchannel (γ) will lead to shadowing of the channel's interior by its walls. After a deposition at glancing incidence, the microchannel will then be only partially filled.

4.3 – Photolithographically Defined Channels

In an alternate process relying upon some of the photolithography techniques described in Section 3.3, it was found possible to produce microchannels filled with more arbitrarily shaped GLAD microstructures. In Figure 4.5, a previously presented structure is shown. (Figure 4.5a was also Figure 3.5). In the image, a microchannel filled with a high surface area helical film is delineated by two photoresist walls. The microchannel depicted in the figure is 935nm deep and, on average, about 29μm wide. The helices within the channel are each composed of 2.75 turns of 340nm pitch SiO_2. In total, the film is 935nm in thickness which is the full depth of the microchannels. As was previously mentioned, the photoresist walls tend to be somewhat uneven, however, the walls are complete along their length and no gaps for fluid to leak are visible along the sides. Since capped or sealed microchannels are potentially of use, [14] and since glass covers cannot be bonded to the photoresist walls of the channel, steps were taken to deposit a capping layer above the patterned films. This was accomplished by a second thin film deposition of the type described in Section 1.6.5 above the patterned film. The column tops form a cap as may be seen in Figure 4.6.

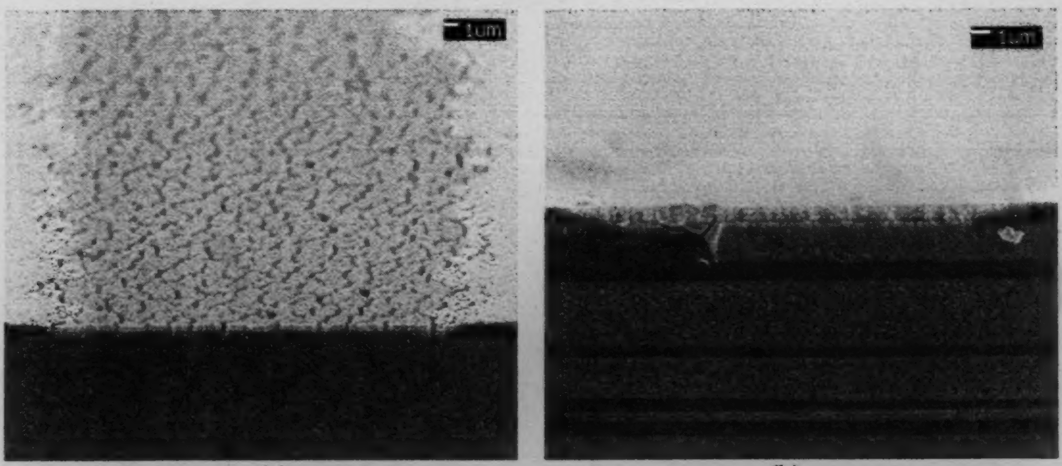

(a) (b)

Figure 4.5 – Lithographic microchannels. In (a) and (b) above, oblique and 90° views of a microchannel filled with GLAD structures is shown. The microchannel is 935nm in thickness and is composed of SiO_2 helices bounded by photoresist walls.

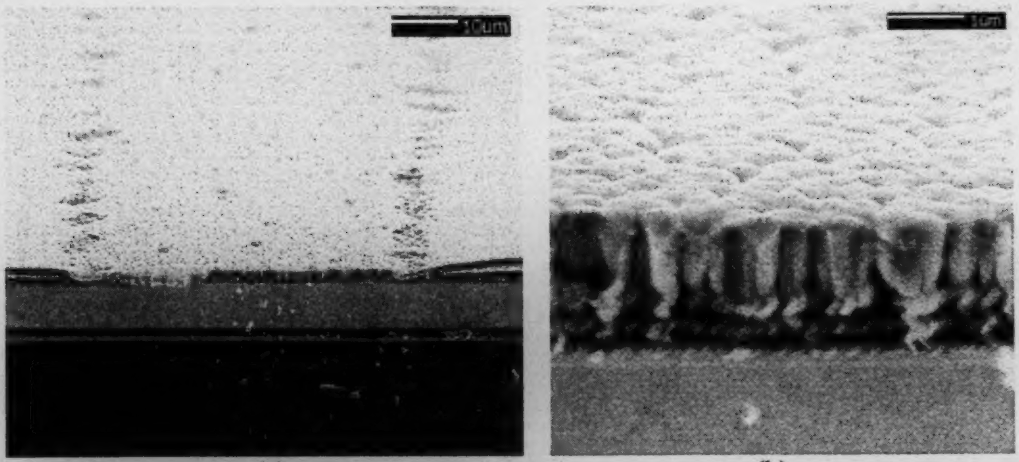

(a) (b)

Figure 4.6 – Capped lithographic microchannels. In (a) and (b) above, the confinement of fluid to a controlled volume is made possible by adding capping layers to lithographically defined microchannels. If the cap can be considered to be completely solid, then fluid is bound between the substrate and cap, and between the photoresist channel walls.

4.4 – Surface Area Measurement by Porosimetry

The primary goal of producing microchannels filled with GLAD structures is to enhance the system's overall surface area. By inspection, this goal has clearly been achieved, but a quantitative measure of the surface area enhancement is still favorable. For this purpose, a surface area/porosity sensor from TPL Inc. (Figure 4.7) was included along with the substrates during the deposition of the SiO_2 films in pre-etched microchannels.[15] Due to signal-attenuation limitations, this sensor could only be coated to 925nm, rather than the full 4μm before it was removed from the vacuum system. At 925nm, the vacuum chamber was vented, and the porosity sensor was removed without disturbing the etched glass substrates. The chamber was then returned to a high vacuum state, and the deposition was resumed until the desired 4μm thickness was reached.

The TPL Inc. porosity sensor is a surface acoustic wave (SAW) device.[16] Waves are launched from a set of interdigitated Au lines at one end of the sensor and propagate to the opposite end, where they are detected by a second set of interdigitated lines. The frequency of this system is determined by the mass of film and adsorbed gases residing on the surface of the sensor. Inside a vacuum chamber, the sensor is subjected to a prolonged period of outgassing at low pressure and high temperature which removes adsorbed gases and restores the sensor resonance to its maximum frequency. Thereafter, the partial pressure of nitrogen is slowly increased, and nitrogen begins to adsorb onto the exposed surfaces. As mass is added, the system resonance is shifted to lower frequencies, and by measuring the magnitude of the variation, the number of adsorbed nitrogen molecules can be calculated. Then, by applying the Brunauer-Emmett-Teller (BET) model of gas sorption, the number of molecules in a monolayer may be found and the surface area may be calculated.[17] A more thorough description of this process may be found in the report by Frye and Martin.[18]

The coated porosity sensor yielded a measured surface area of 119.5 μm^2 per μm^2 of surface, or 129.2 $(\mu m^2/\mu m^2)/\mu m$. Scaling linearly to the full thickness of the film in the microchannel gives an approximate surface area of 517 $\mu m^2/\mu m^2$. The validity of the linear scaling will be discussed in the next section.

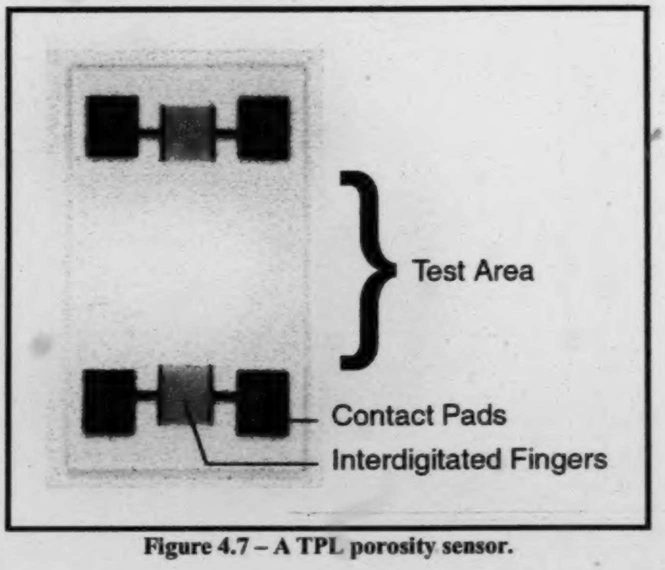

Figure 4.7 – A TPL porosity sensor.

4.5 – Surface Area Measurement by Simulation

Measuring the surface area enhancement of the lithographic microchannels was not possible by direct methods, however, some indication of performance was thought necessary. To this end, the 3D-FILMS simulation tool was again employed.[19,20] In Figure 4.8, a computer-generated film is shown which was simulated with deposition parameters matching those of the GLAD film within the lithographically patterned microchannels.

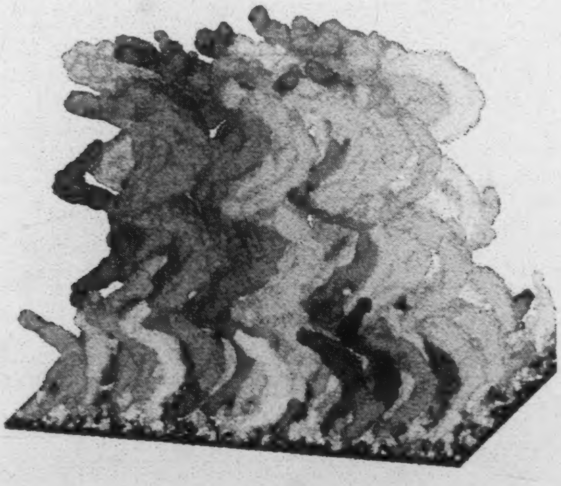

Figure 4.8 – Computer-generated simulation of a helical GLAD film. This film was modeled with parameters resembling that of the actual film used in the lithographic patterning of filled microchannels.

In a one cube thick cross-sectional slice of the model, the number of cubes on the outer edges of the columns was electronically counted, and from this, the exposed area of the slice was calculated. Dividing by the volume gave the differential surface area ($((\mu m^2/\mu m^2)/\mu m)$) at that point in the film. Plotting this parameter over the entire thickness of the film yields a graph of differential surface area, as is shown in the solid line plot of Figure 4.9.

In the initial phases of growth the differential surface area is very high. Competition and shadowing conditions have yet to be established and many small columns and nuclei are dispersed across the substrate. As certain columns begin to dominate, a gradual decrease in differential surface area is manifested because a reduced fraction of the columns continue growing. In the simulation, the differential surface area appears to approach a steady state value of about 47 ($\mu m^2/\mu m^2$)/μm. At the far right of the data set, the surface area drops abruptly to indicate the film surface.

The total surface area for the simulation is calculated by integrating the differential surface area over the complete thickness of the film, and in this case, 42 $\mu m^2/\mu m^2$ was calculated for the 0.8μm thick simulation. This is shown in the dashed line plot of Figure 4.9. Because the differential surface area is not constant over the entire thickness of the film there is clearly some uncertainty in the validity of the linear scaling used in the previous section. A linear scaling will always slightly overestimate the surface area in the upper portions of the film. Although imperfect, the shape of the integrated surface area curve does appear nearly straight, and the application of linear scaling laws is a reasonable approximation.

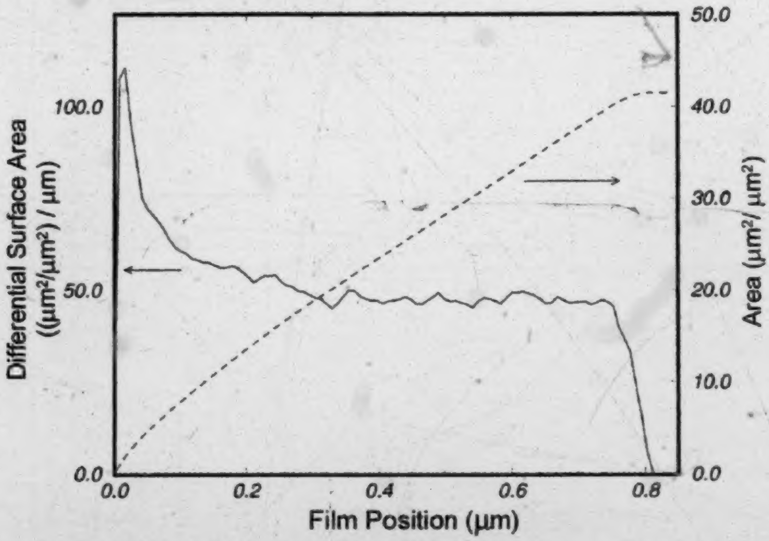

Figure 4.9 – Simulated surface area. The solid curve represents the differential surface area at points within a simulated thin film, and the dashed curve is its integral, the cumulative surface area.

Sections of this chapter have been reproduced by permission of The Electrochemical Society, Inc., from the paper entitled, "Microchannel surface area enhancement using porous thin films", which appeared in the May 2000 issue of the Journal of the Electrochemical Society.[21]

References

1) Y. Xiong, S.-R. Park, H. Swerdlow, Base stacking: pH-mediated on-column sample concentration for capillary DNA sequencing, *Anal. Chem.*, **70**, 3605-3611, (1998).

2) C. Backhouse, M. Camaano, F. Oaks, E. Nordman, A. Carillo, B. Johnson, S. Bay, DNA sequencing in a monolithic microchannel device, *Electrophoresis,* **21**(1), 150-156, (2000).

3) K. Fluri, G. Fitzpatrick, N. Chiem, D.J. Harrison, Integrated capillary electrophoresis devices with an efficient postcolumn reactor in planar quartz and glass chips, *Anal. Chem.*, **68**, 4285-4290, (1996).

4) D.J. Harrison, A. van den Berg, Micro Total Analysis Systems '98, (Kluwer Acedemic Publishers, Dordrecht, 1998).

5) B. He, N. Tait, F. Regnier, Fabrication of nanocolumns for liquid chromatography, *Anal. Chem.*, **70**, 3790-3797, (1998).

6) K. Hosoya, Y. Shirasu, K. Kimata, M. Tanaka, Molecularly imprinted chiral stationary phase prepared with racemic template, *Anal. Chem.*, **70**, 943-945, (1998).

7) M. Kempe, Antibody-mimicking polymers as chiral stationary phases in HPLC, *Anal. Chem.,* **68**, 1948-1953, (1996).

8) L. Schweitz, L.I. Andersson, S. Nilsson, Capillary electrochromatography with predetermined selectivity obtained through molecular imprinting, A*nal. Chem.*, **69**, 1179-1183, (1997).

9) D.W. Armstrong, J.M. Schneiderheinze, Y.-S. Hwang, B. Sellergen, Bubble fractionation of enantiomers from solution using molecularly imprinted polymers as collectors, *Anal. Chem.*, **70**, 3717-3719, (1998).

10) R. Boom, C.J.A. Sol, M.M.M. Salimans, C.L. Jansen, P.M.E. Wertheim-van Dillen, J. van der Noordaa, Rapid and simple method for purification of nucleic acids, *J. Clin. Microbiol.*, **28**(3), 495-503, (1990).

11) B. He, L. Tan, F. Regnier, Microfabricated filters for microfluidic analytical systems, *Anal. Chem.*, **71**, 1464-1468, (1999).

12) G. Ocvirk, E. Verpoorte, A. Manz, M. Grasserbauer, H.M. Widmer, High performance liquid chromatography partially integrated onto a silicon chip, *Anal. Methods Instrum.*, **2**(2), 74-82, (1995).

13) R.N. Tait, T. Smy, M.J. Brett, Structural anisotropy in oblique incidence thin metal films, *J. Vac. Sci. Technol. A,* **10**(4), 1518-1521, (1992).

14) M. Seto, M.J. Brett, Arrays of self-sealed microchambers and channels, *J. Mater. Chem.*, **12**, 2348-1351, (2002).

15) TPL Inc., Albuquerque, NM 87109.

16) D.J. Taylor, P.F. Fleig, S.L. Hietala, Technique for characterization of thin film porosity, *Thin Solid Films*, **332**, 257-261, (1998).

17) S. Brunauer, P.H. Emmett, E. Teller, Adsorption of gases in multimolecular layers, *J. Am. Chem. Soc.*, **60**, 309-319, (1938).

18) G.C. Frye, S.J. Martin, Materials characterization using surface acoustic wave devices, *Appl. Spectrosc. Rev.*, **26**(1&2), 73-149, (1991).

19) T. Smy, D. Vick, M.J. Brett, A.T. Wu, J.C. Sit, K.D. Harris, Three dimensional simulation of film microstructure produced by glancing angle deposition, *J. Vac. Sci. Technol. A,* **18**(5), 2507-2512, (2000).

20) T. Smy, D. Walkey, K.D. Harris, D. Vick, M.J. Brett, Simulation of thin film thermal properties using 3D-FILMS, *Thin Solid Films*, **391**, 88-100, (2001).

21) K.D. Harris, M.J. Brett, T.J. Smy, C. Backhouse, Microchannel surface area enhancement using porous thin films, *J. Electrochem. Soc.*, **147**(5), 2002-2006, (2000).

Chapter Five

Fabrication of Perforated Thin Films and Replica Thin Films

5.1 – Existing Technology

Descriptions of techniques for producing thin films perforated by organized arrays of pores are not uncommon in the literature. In lightly n-doped silicon wafers, for instance, anodic etching can be used to form cylindrical pores.[1,2] In this process, pore tips, having an abundance of holes (h^+), are able to accept electrons as required, enabling the dissolution of atoms into HF. At the walls, however, the formation of a passivated region by the depletion of electron acceptors prevents the pores from spreading in a transverse direction. The phenomena of anodic etching in aluminum has been studied to an even greater degree: Deep (>400μm) pores with aspect ratios around 500 have been achieved by redirecting the expansion energy in the conversion between Al and Al_2O_3 into the self-organization of two-dimensional hexagonal pore arrangements.[3-5] In addition, techniques involving an optical drill,[6] block co-polymers,[7] nuclear track etching,[8,9] templating from drawn glass fibers,[10] surface micromachining,[11] deep reactive ion etching (dRIE),[12] or even simple photolithography have all proven adequate in fabricating high-aspect ratio pores. Some biological organisms even perform a similar function, and a larger-dimension process known as replamineforming (the name being derived from "replication of amine form")[13] has been utilized in specific medical applications.[14,15]

Despite the prevalence of research in the area, most of the processes that have been described are generally restricted to the production of arrangements of pores extending through the material in a direction perpendicular to the substrate. Very little control over the pore shape is reported, and with few exceptions, the pores are predominantly circular in cross-section. Applications exist, however, for perforated films of a slightly different nature: photonic devices,[16] size-selective particle filters,[17] sensors,[18] or optically active devices[19] may all be realizable in the form of inverse GLAD films, i.e., thin films perforated by helical, chevron or other such shaped holes. Photonic devices warrant particular attention. In a recent issue of *Science*, a statement was made of square spiral microstructures: "in the case of silicon posts in air (direct structure), the full PBG can be as large as 15% of the center frequency, whereas for air posts in silicon (inverted structure) the maximum PBG is 24% of the center frequency."[16] Since PBG crystals are of vital importance to next-generation, all-optical computers, this statement lends immense justification to an investigation of inverted GLAD structures.

In this chapter, a four step process for fabricating these controllably perforated thin films is described which employs glancing angle deposition in conjunction with standard photolithography techniques. Subsequently in Chapter 6, applications for the films including humidity sensing and optical polarization rotation are discussed, and specific experimental results are presented in some detail.

5.2 – Fabrication of Perforated Thin Films

Perforated thin films (PTFs) are created by the four step technique illustrated in Figure 5.1.[20] Fabrication begins with the deposition of a template film by glancing angle deposition, (see Figure 5.1a). Most types of GLAD films may be utilized at this stage; the predominant limitations being that no capping layers may be present, and, because a negative structure is sought, the GLAD template must be of sufficient porosity to ensure the cast structure will be continuous and structurally sound. The second fabrication step is also familiar: a low viscosity material interpenetrates the GLAD structures, entirely filling in the pores, (see Figure 5.1b). Because any voids in the conglomerate structure would eventually be transferred into the perforated film, it is essential that great care be taken to ensure the totality of the filling process. After an effective fill, the template will be completely encapsulated by the cast material, and it is then necessary to remove a thin layer from the top of each filled film to expose the tips of the template structures to additional processing, (see Figure 5.1c). The more material removed, the thinner the resulting cast will be, and so to achieve the best reproduction of the template, it is important to etch back the filler only until the tips are first exposed. Finally, the template film must be removed from the cast, (see Figure 5.1d), and to accomplish this, the film is immersed in a solution designed to selectively attack the template film and preserve the filler. At this stage, isotropic etchants are preferred because they remove the template material regardless of location and crystallographic orientation. Directional etchants, such as reactive ion etching (RIE) or KI/I_2 silicon etchants, are likely to leave pockets of template material, or take inordinate lengths of time to etch the template. Upon the successful completion of these four steps, one is left with a cast of the original template in an alternate material.

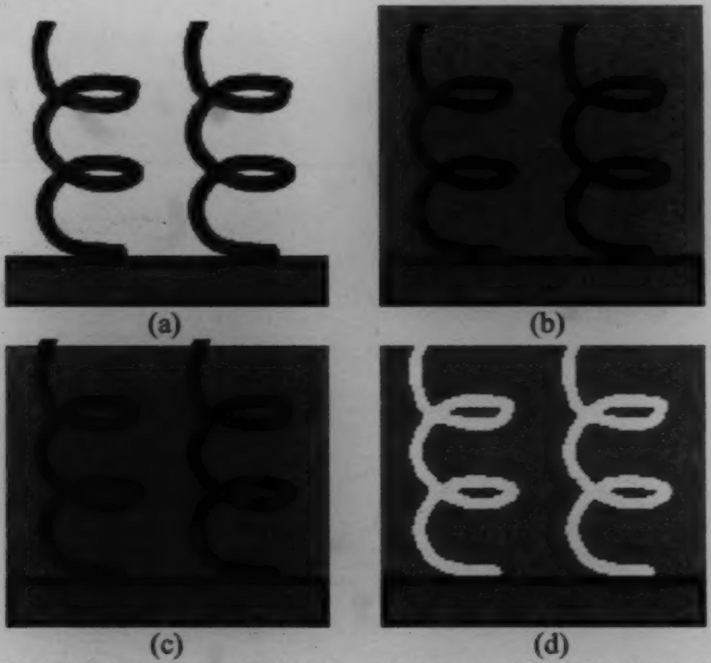

Figure 5.1 – Conceptual steps in the fabrication of a perforated thin film. A template film is first deposited (a), and subsequently filled with a low viscosity material (b). The filler is then etched back slightly (c), and then the original template is removed (d).

This process has successfully been developed using real thin films. In Figure 5.2, four SEM images acquired at stages of typical helically perforated thin film fabrication runs are included. The filler material used in each of the figures (and, except where otherwise noted, everywhere else in this chapter) was HPR504 photoresist. As a result of materials issues, a number of minor, additional processing steps were also required, and each will be discussed in the text.

In Figure 5.2a is a helical template film of SiO_2 which was deposited with a flux incidence angle of 85°. The film consists of 6 turns, each of 250nm helical pitch, for a total thickness of 1.5μm. From this oblique viewing angle, it may be seen that the film is quite porous; the helices stand as individual structures, and as was the necessity for an effective template, the network of voids appears to be continuous. The composition and general appearance of this film are typical of the PTF process, and a variety of films have been fabricated using templates of much the same nature. In the overwhelming majority of these films, SiO_2 acts as the original template material. The reasons for this choice are twofold: first, the engineering of SiO_2 microstructures by GLAD is a well understood process. The material's high melting temperature and low surface mobility make it an extremely favorable choice in which to design porosity, and so the ease of engineering known structures into its negative image is correspondingly great. Second, because SiO_2 is in common industrial usage as a gate oxide, pre-formulated commercial etchants are effective, inexpensive and readily available. Preliminary investigations using alternate template materials (such as MgF_2, Ti, Cr, and SiO) were also initiated, but due to the effectiveness of SiO_2 templates, this research was abandoned early on.

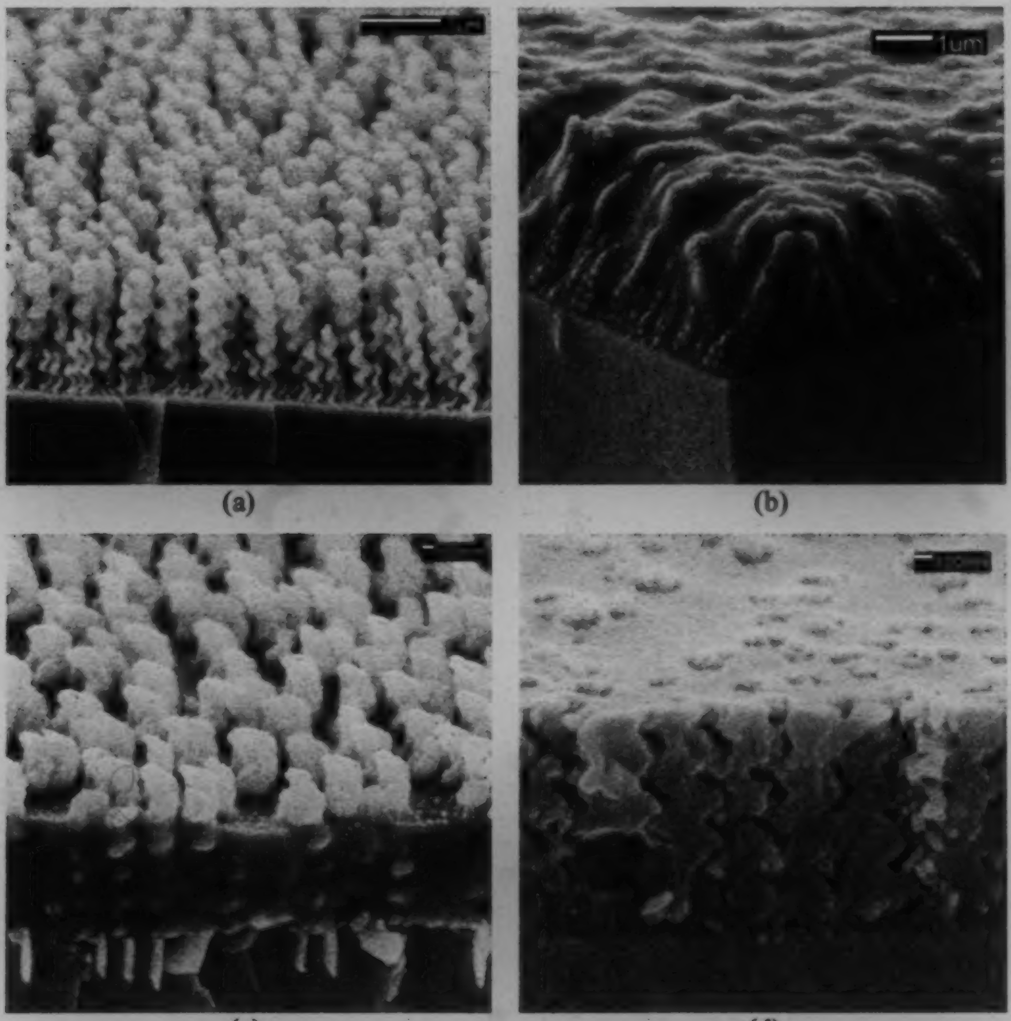

(a) (b)

(c) (d)

Figure 5.2 – Steps in the fabrication of a perforated thin film. To create a perforated film, an SiO_2 template (a) is filled with photoresist (b), exposed to UV, dipped in developer (c), and etched in BOE (d).

In Figure 5.2b, a film is presented which has been filled with photoresist. Since this process has already been thoroughly described, the image will not be discussed at length. I comment only that the SiO_2 template appears to be completely encapsulated, and that no regions devoid of photoresist are apparent. After filling the film, excess solvent was removed by heating the composite to 115°C under a rough vacuum for 90s.

The next step, although seemingly trivial, required a considerable research effort to surpass. In order to enable etchants to penetrate into the film, the template structures must be freed at their tips from photoresist encapsulation. There are a wide variety of solvents which are capable of removing quantities of photoresist, but in many cases complications arise preventing their use. Concentrated acetone or formulated photoresist removal solutions, for instance, generally act too rapidly for controllable photoresist removal, and reactive ion etching under all of the conditions studied has an extremely unpredictable effect upon the photoresist/SiO_2 structure. The method that was eventually proven to be effective involves a timed immersion in Shipley 354 Developer solution. Because HPR504 photoresist is a positive resist, only UV exposed material is developer soluble. Therefore, the photoresist/SiO_2 composites were all exposed to UV radiation before immersion. (Flood exposure in a mask aligner, hand-held UV lamps, and ambient UV radiation were all investigated and found to effectively expose the resist after varying lengths of time.) The range of developer immersion times from 0s to 10s was studied, and it was discovered that simply dipping the substrates in developer and immediately rinsing them with water minimizes the loss of film thickness while still allowing sufficient developer time to free the helix tips. Because a greater amount of control over the developer was thought to be advantageous, the effect of dilution of the 354 Developer was also investigated. 1:1, 1:2, and 1:4 solutions of 354 Developer in water were used to remove exposed resist atop GLAD structures, but unfortunately, after each of the tests, an extremely mottled texture was apparent in the remaining photoresist. As this phenomenon occurred using even the concentrated solution, the effect may simply be a random anomaly, yet in the SEM images, an apparent progression towards more uneven microstructures is perceptible as the dilution ratio is increased. Because undiluted developers were found to be wholly effective, experiments along this line were discontinued, but if a reduced photoresist removal rate becomes, in any way, critical, dilution experiments could easily be resumed.

For illustrative purposes, an overdeveloped film is shown in Figure 5.2c. 530nm of resist were removed from the top of the structure, leaving 775nm to make up the perforated film. Although the presence or absence of residual resist cannot be determined from the image, subsequently immersing the films in solutions of BOE adequately removes the SiO_2 from the photoresist, and therefore, it can be concluded that the structures were sufficiently free from resist. Initially, there was some concern that surface tension, inadequate diffusion or some other unexpected effect would prevent etchants from penetrating deeply into the resist and removing the entire template, but although this may occur with some template/filler/etchant combinations, no such behavior was observed in these perforated films. Also, because etch rates were unknown under these confined conditions, the first samples were soaked in BOE for up to fifteen minutes before being retrieved. After some experimentation, the etch time was reduced to approximately one minute per micrometer of template thickness, and sufficient etching to remove the entire template was observed.

In Figure 5.2d, a completed perforated thin film is depicted. The film is composed of 5¼ turns of 1.2µm thick photoresist, and it was the first ever successfully fabricated helically perforated thin film.

5.3 – Variants of Perforated Thin Films

The greatest advantage of the perforated thin films technique is the degree of control it grants over the pore structure of the resulting thin films. All of the features which can be engineered into a template film (assuming sufficient porosity) can be transferred into a perforated film, and in this section, a brief survey of some of these film architectures is provided.

5.3.1 – Alternate pitch helically perforated thin films: The pitch of the template is not an important factor in the successful production of a perforated film. In Figure 5.3, a large pitch, helical template film is presented along with a corresponding perforated film. Both the template (a) and its negative (b) consist of one turn, and the thicknesses are roughly equal. Because photoresist does not cleave along crystal planes as in an Si wafer, preparation for the SEM resulted in the resist breaking along the lines of minimum film strength, namely the helical voids. As a consequence, the photoresist presents a three-dimensional surface to the SEM rather than a flat face, and it is difficult to discern a specific void/resist/void pattern in the perforated film. However, a pattern of pores is clearly visible on the surface, and from the side, a definite helical pattern is in evidence, which supports the claim that a helical pore structure exists throughout the film.

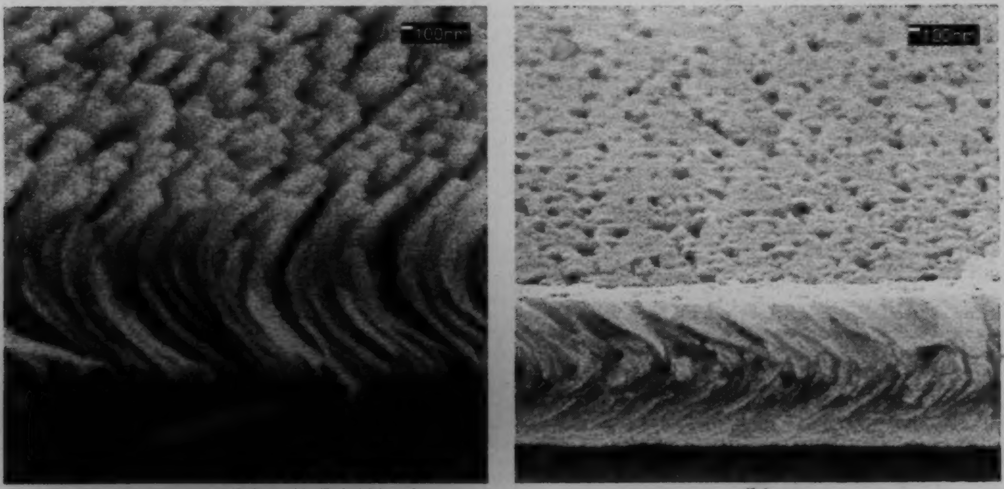

(a) (b)

Figure 5.3 – Large pitch helical perforations. By using the SiO_2 film in (a) as a template, the high pitch (1.6μm) helically perforated thin film shown in (b) was fabricated.

5.3.2 – Chevron perforated thin films: In the perforated thin film process, there is no inherent difference between a chevron template and a helical template. So long as the individual template microstructures are sufficiently separated as to permit the formation of a continuous photoresist matrix, it is practically possible to form a negative image by a process identical to that of Section 5.2.

In Figure 5.4a, a chevron template film is shown. The film is 3.0μm thick, and is composed of eight arms of SiO_2. By the process described above, the chevron perforated thin film of Figure 5.4b was created from this SiO_2 film. All eight chevron arms of the template may be seen in its negative image, and very little of the photoresist has been lost to the developer.

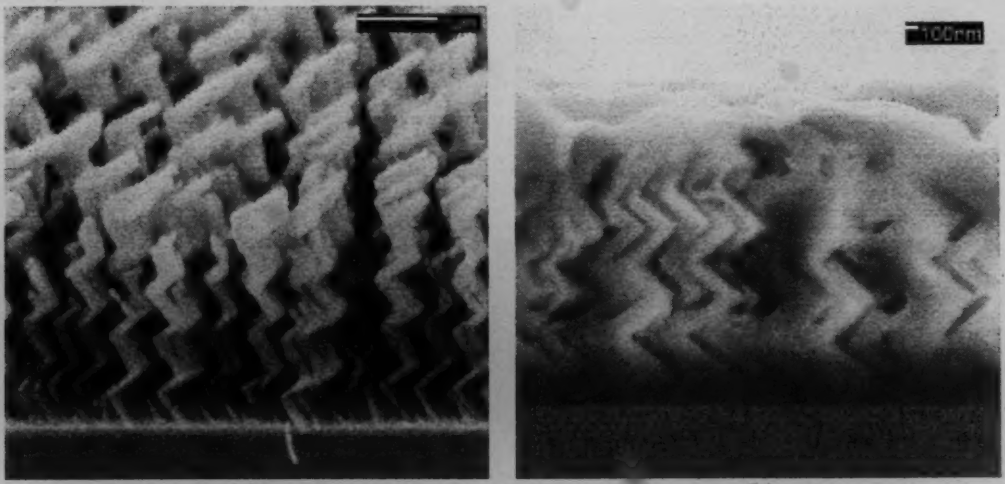

(a) (b)

Figure 5.4 – Chevron perforated thin films. A thin film with chevron shaped perforations can be fabricated by the technique described in Section 5.3.2. In this case, the SiO_2 film in (a) was used as a template for the perforated thin film in (b).

5.3.3 – Periodically perforated thin films: In Section 3.4, a technique for producing thin films of GLAD structures arranged into regular patterns was presented, and there is no physical restriction preventing their use as templates for perforated films. In Figure 5.5, a helical template consisting of 1.75 turns of 1.3μm pitch SiO_2 in a rectangular array is shown, and in Figure 5.5b the corresponding perforated thin film is shown. The negative image, in this case, shows a number of vacancies in the array where the BOE etchant was unable to remove the underlying template, and in addition, a significant amount of debris appears to be located in each of the helical pores. A portion is probably attributable to the preparation for SEM imaging, but whether the entire amount can be ascribed to this cause is unknown.

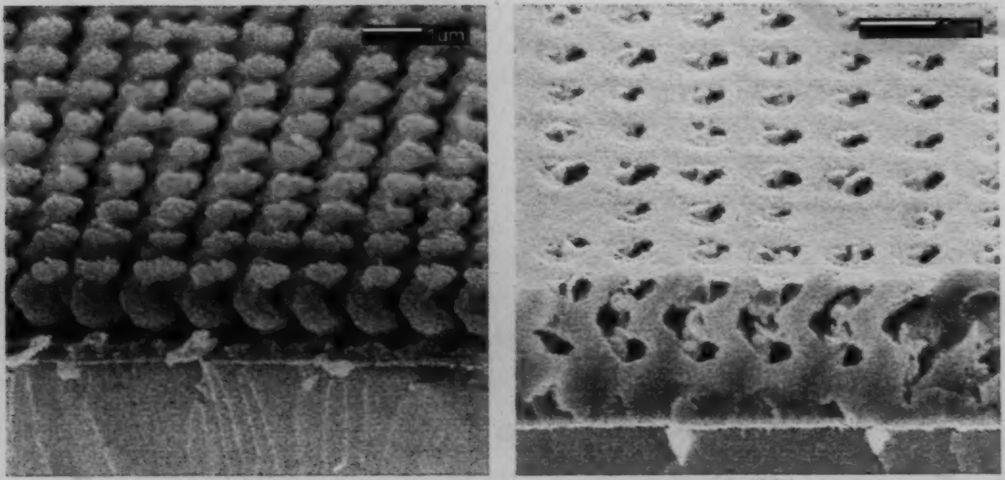

(a) (b)

Figure 5.5 – Periodic perforations. Using a periodic array of SiO_2 GLAD structures as a template leads to a perforated thin film with periodically arranged pores.

5.3.4 – Variations in filler material: Often applications exist for perforated films composed of materials other than photoresist. The structural strength of polymers, for instance, may be a limitation for some applications, and a more robust material would be preferred. Or, the surface chemistry and catalytic properties of a specific material may be critical in a porous thin film application. Therefore, in order to increase the versatility of the process a proof-of-principle investigation into the substitution of alternate filler materials was undertaken.

Provided sufficiently selective etchants can be obtained, any material that will flow into the voids of a GLAD film, completely eliminating the porosity, may be a suitable candidate for use as a perforated thin film filler. A substance apparently meeting these requirements is 400F methylsilsesquioxane spin-on-glass from Filmtronics.[21] In literature provided by the company, 400F is reported to "successfully smooth 1.1μm topographies by flowing from the tops of metal lines into the trenches and voids leaving an unnoticeable amount of 400F on top of the geometry and yielding excellent planarization qualities". These reflow and planarization capabilities suit the needs of the perforated thin film process.

The spin-on-glass was applied while spinning at 1.5krpm, and the rotation speed was then increased to 3.0krpm and held constant for 20s. Solvents were removed and reflow of the glass was then encouraged in a multi-step bake process. Wafers were sequentially heated to 80°C for 1 minute, 165°C for 2 minutes, 190°C for 2 minutes and 250°C for 1 minute. In order to prevent thermal shock-induced structural cracks in the SOG, the wafers were allowed to cool slowly by returning them to the 165°C hot-plate for 45s, and then to the 80°C hot-plate for 5 min. Two identical coats of 400F were applied by this procedure to helical GLAD films similar to that of Figure 5.2a. Afterwards, the spin-on-glass was cured by slowly heating the films to 390°C, holding at this temperature for 30 minutes, and slowly returning the system to room temperature.

The tips of the template microstructures were exposed by etching in an Oxford Instruments Plasmalab System100 ICP/RIE etch system,[22] the coated substrates being subjected to CF_4 plasma generated at 450W for 3 minutes. To remove the template, the films were then immersed in a BOE etch for 1 minute, and in Figure 5.6, a 1.2μm thick, 5 turn helically perforated film is presented which was produced by this method.

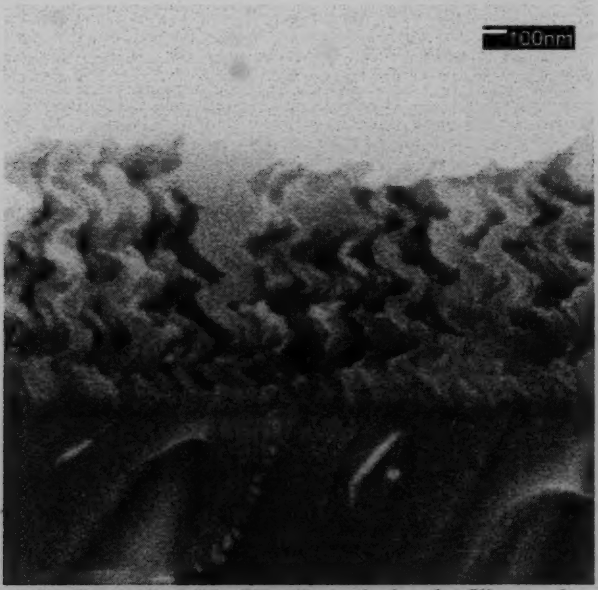

Figure 5.6 – Perforated spin-on-glass thin film. By replacing the filler, perforated thin films can be produced with alternate materials. Here, methylsilsesquioxane spin-on-glass was applied between the SiO_2 template helices.

5.4 – The Perforated Thin Films Process

As a summary, Table 5.1 may be consulted for the recipe that was found to be reliable in the production of perforated thin films composed of photoresist.

Step	Process	Description
1	Template Deposition	Deposit SiO_2 as required, ensuring the availability of sufficient porosity
2	Photoresist Fill	Spin 3mL of HPR504 photoresist into the template at 5250rpm
3	Softbake	Heat the substrate to 115°C for 90s to remove excess solvents
4	Photoresist Exposure	Allow the photoresist to expose overnight in ambient UV radiation
5	Etchback	Dip-immerse the substrate in 354 Developer, followed by an immediate rinse in water
6	Template Removal	Immerse the substrate in BOE for one minute for every μm of template material

Table 5.1 – Steps in the production of a perforated thin film.

5.5 – Replica Thin Films

5.5.1 – Materials limitations: It was previously shown that the GLAD technique is effective in producing high quality, reproducible, porous thin films. Density, microstructure, pore characteristics, surface area, column positioning and many other properties could all be chosen and engineered into thin films to suit particular applications. Unfortunately, the choice of materials has remained a limiting factor. Certain materials such as YSZ, SiO_2, and MgF_2 form well-defined structures; their growth patterns are consistent and well understood, the materials are easy to deposit, and controlled structures of a considerable thickness can be produced without encountering adverse growth behavior. In general, ceramics and fluorides tend to form excellent structures, while other useful materials, such as polymers and some metals, are much less amenable to the engineering of nanostructure. At least three effects contribute to the problem. First, in cases involving ionic or molecularly bonded materials (such as polymers), some chemical breakdown of the evaporant is likely to result from the large amounts of energy injected during deposition, which potentially leads to composition modification.[23] Second, contaminants such as oxygen in PVD processes can react with the growing film or incident vapor flux to form compounds or unintended impurities. Third, and possibly most important, surface mobility plays a critical role in the development of porous nanostructures. Materials having high surface mobility are generally less suited to forming high quality porous nanostructures than materials of lower mobility deposited under the same conditions. This effect is most prominent in metallic films. In images of GLAD thin films of low melting point metals (Figures 5.7a and 5.7b, for example), it often easy to discern undesirable features: the column diameter may increase markedly from substrate to surface, secondary nucleation or bifurcation is common, clump-like appearances are often manifest at the film surface, and agglomeration of a number of smaller columns into larger, less controlled structures is often observed. These are material-dependent effects, and it is difficult to overcome them by improved control of the deposition process. Fortunately, SiO_2 thin films form well-controlled structures, and they also act as effective templates for perforated thin films. Thus, by developing a double templating technique employing electrodeposition through PTFs, the structure of well-constructed SiO_2 templates may be transferred into replica films of alternate materials that are more difficult to fabricate by direct GLAD deposition.

5.5.2 – Electrodeposition of GLAD films: In an electrodeposition experiment, electron exchange reactions force ions to precipitate from solution to form a solid film on a conducting electrode.[24,25] In the case of Ni electrodeoposition, for instance, at a sufficient voltage, the reaction $Ni^{2+} + 2e^- \rightarrow Ni(s)$ takes place at a conducting cathode, while at the anode, the complementary decomposition reaction occurs to provide electrons. The net results are an increase in atoms upon the cathode, a matching reduction in atoms on the anode, and a measurable flow of current from cathode to anode.

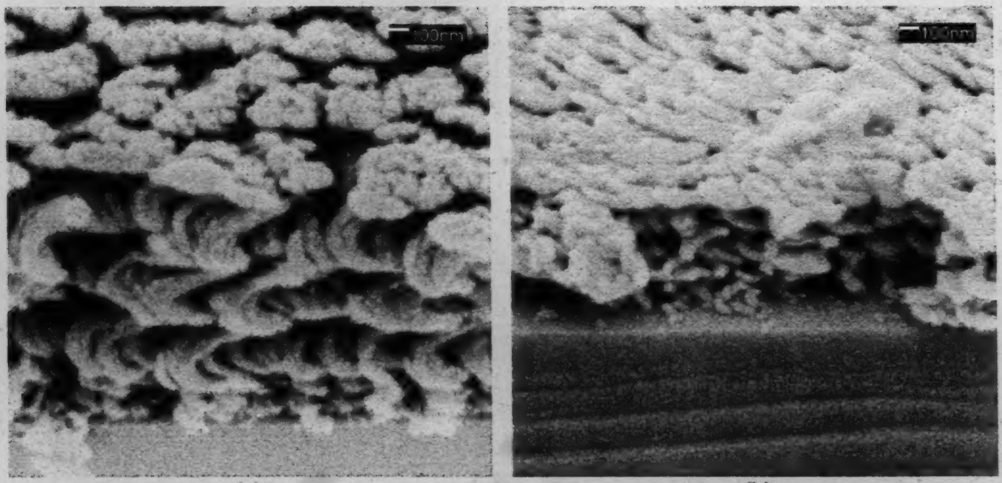

(a) (b)

Figure 5.7 – Motivation for alternate fabrication techniques. Because of bifurcation (a), or high atomic mobility (b), controlled characteristics are often difficult to engineer into thin films of Ni (a) of Cu (b).

To replicate GLAD-like films by electrodeposition, an apparatus pictured conceptually in Figure 5.8 was utilized. PTFs having the desired pore structure are fabricated above a pre-deposited metal cathode, and an electrical contact is made to a masked metal area. The wafer is held at a negative potential and placed in an ionic solution of the metal or alloy to be plated, while a positively biased anode is immersed nearby. After sufficient deposition to fill the template, the circuit is broken and electroplating is discontinued. The cast material is then removed (for example, a photoresist mold may be dissolved in acetone) to leave behind the shaped metal. Other research groups have employed similar casting processes to fabricate simple post or post perforated films in a variety of materials.[8,26-28]

This process has been successfully used to produce metallic thin films having roughly the same appearance as their SiO_2 templates. In Figure 5.9, a perforated thin film is shown situated above a Ti electrode. The film was formed from HPR504 photoresist using an SiO_2 template having six turns, each 340nm in pitch. The total photoresist thickness is 2.0μm, and the electrode is 780nm thick. This structure was immersed in Krohn Ni electroplating solution,[29] and the required electrical connections were formed. The electrodes were then biased, and a current-limited 180mA was allowed to flow for 300s. The processed film was then rinsed in acetone, and the structures shown in Figures

5.10a, and 5.10b were formed. This film is 1.2µm in thickness, and very closely resembles its template. (Compare to the structures of Figure 5.7.)

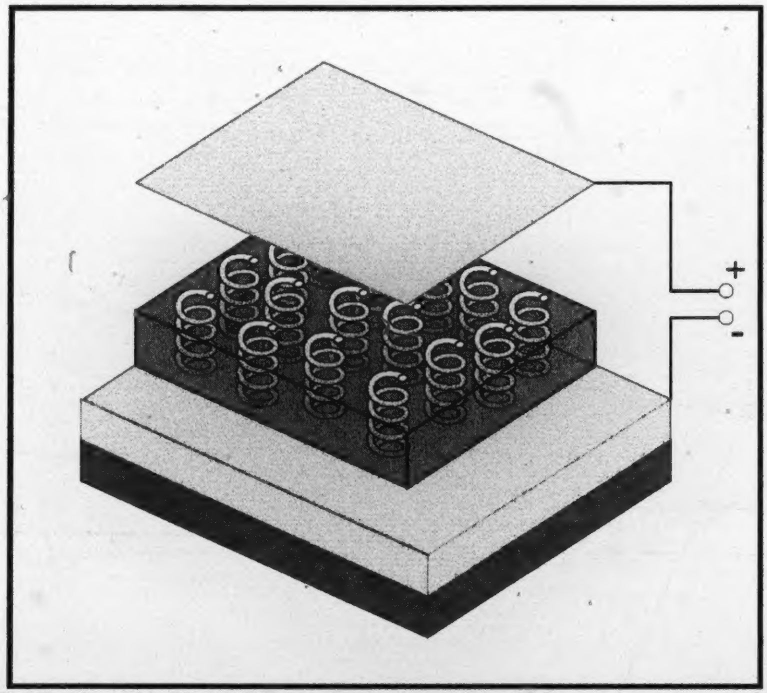

Figure 5.8 – Replication of a GLAD film by electrodeposition. Using an arrangement of electrodes and a perforated film, a thin film taking the shape of the original template may be electroplated through a photoresist matrix.

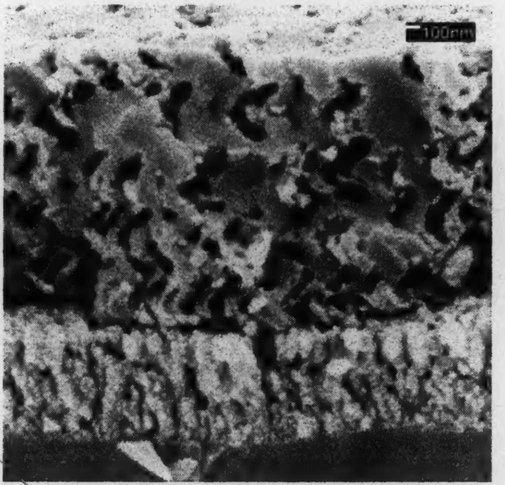

Figure 5.9 – Replica thin film template. Shown in the figure is the perforated film and Ti electrode structure which was used as the template for Ni electrodeposition.

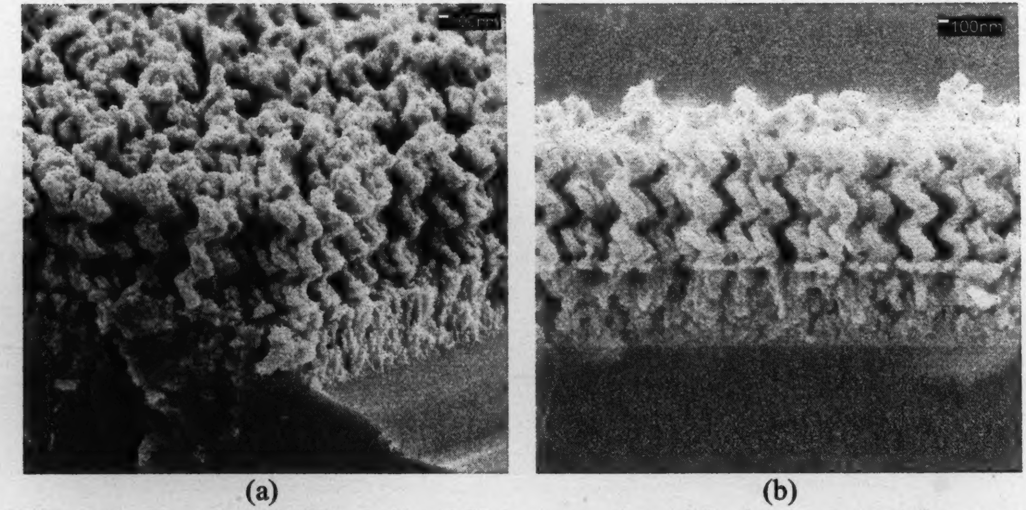
(a) (b)

Figure 5.10 – Ni replica thin film. In (a) and (b), images are shown following the electroplating process.

To confirm the effectiveness of the technique, a similar process was performed using a second template/perforated film combination and substituting Cu as the plating material. Because of some difficulties ensuring the existence of an adequate ionic current path between the anode and the photoresist coated cathode, the GLAD template deposition, in this case, was initiated in Cu, and only after ~50nm were deposited was the evaporant switched to SiO_2. In Figure 5.11a, the helical SiO_2 template of seven turns, each 250nm in pitch is shown. The film was deposited at $\alpha = 85°$ above a EB-PVD deposited Cu electrode. No adverse structural effects are apparent as a result of the transition from Cu to SiO_2 during the helical evaporation, and as a benefit, the copper regions acted as an etch stop during the fabrication of its perforated template film. The electrode/photoresist combination was immersed in Krohn Cu electroplating solution and connected to a grounded Cu anode. The cathode was biased at 2V and a current-limited 100mA was allowed to flow through the circuit for 60s. (These parameters were selected by trial-and-error experimentation.) In Figure 5.11b, the post-acetone rinse results are presented. This plated film is 1.9µm in thickness, and in structure, it is very similar to its template. The spherical projections above the Cu helices were the result of a slight overestimation of the appropriate plating time, allowing excess copper to "spill out" of its photoresist mold. Although the projections do not appear in the original template, rather than being detrimental, they may actually perform a beneficial function in certain circumstances. Given sufficient electrodeposition time after the mold has been filled, the projections may eventually form a solid cap above the helical layer, and in some situations, this has been a highly favorable property.[30,31]

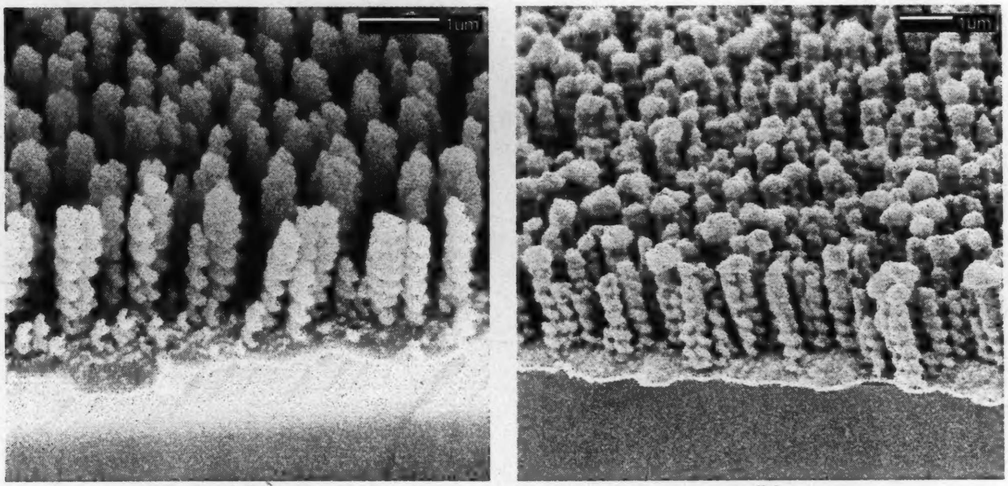

(a) (b)

Figure 5.11 – Cu replica thin film. The helical, SiO_2 GLAD film which was used as a template for Cu electrodeposition is shown in (a), and the end result appears in (b).

5.5.3 – Composition analysis: To verify the replica films' composition, EDX analyses of the electrodeposited films were undertaken. In both cases, the spectra showed the appropriate peaks for Ni or Cu (the helices) and Ti or Cu (the electrode). In addition, minor Si and Ir peaks from the substrate and the SEM conductivity coating were also in evidence. In Figure 5.12, a sample spectrum for an electroplated Ni film is provided. In the figure, the largest peaks are Ni and Ti, followed by Si, Ir and a small Fe peak. This Fe peak is likely a result of contamination from the steel contact clips, or from impurities in the electroplating solution or Ni anode. Due to non-homogeneous detection sensitivities for the various atomic species, the EDX intensity data should be considered as purely qualitative.

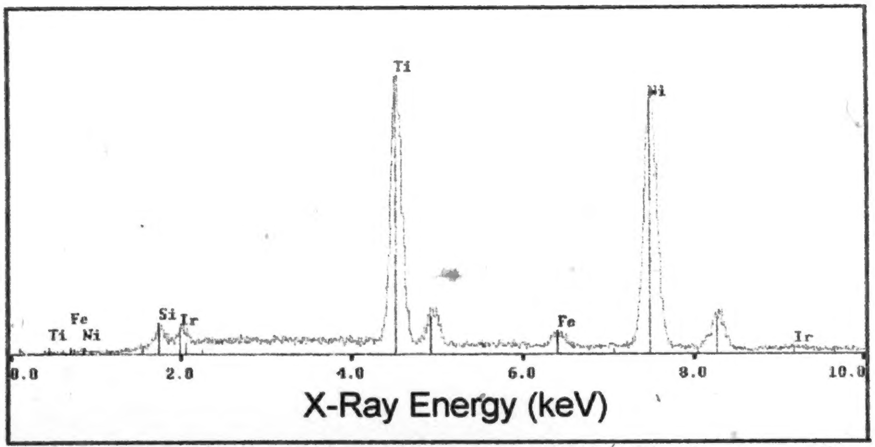

Figure 5.12 – EDX spectrum for electroplated Ni helices. Ni and Ti peaks corresponding to the electroplated helices and underlying electrode can be clearly identified in the image. Smaller peaks originate from the Si substrate and Ir conduction coating, but the source of Fe is unknown.

Portions of this chapter have been excerpted from the papers entitled, "Fabrication of perforated thin films with helical and chevron pore shapes", which was published in the June 2001 issue of Electrochemical and Solid-State Letters,[32] and "Fabrication and optical characterization of template-constructed thin films with chiral nanostructure", which is scheduled to appear in IEEE Transactions on Nanotechnology.[19] The Electrochemical and Solid-State Letters excerpts appear by permission of The Electrochemical Society, Inc., and the IEEE Transactions on Nanotechnology excerpts appear with the permission of the Institute of Electrical and Electronics Engineers, Inc.

References

1) J.E.A.M. van den Meerakker, R.J.G. Elfrink, F. Roozeboom, J.F.C.M. Verhoeven, Etching of deep macropores in 6 in. Si wafers, *J. Electrochem. Soc.*, **147**(7), 2757-2761, (2000).

2) V. Lehmann, The physics of macropore formation in low doped n-type silicon, *J. Electrochem. Soc.*, **140**(10), 2836-2844, (1993).

3) A.P. Li, F. Müller, U. Gösele, Polycrystalline and monocrystalline pore arrays with large interpore distance in anodic alumina, *Electrochem. Solid-State Lett.*, **3**(3), 131-134, (2000).

4) H. Masuda, H. Asoh, M. Watanabe, K. Nishio, M. Nakao, T. Tamamura, Square and triangular nanohole array architectures in anodic alumina, *Adv. Mater.*, **13**(3), 189-192, (2001).

5) C.G. Granqvist, Å. Andersson, O. Hunderi, Spectrally selective surfaces of Ni-pigmented anodic Al_2O_3, *Appl. Phys. Lett.*, **35**(3), 268-270, (1979).

6) A. Chelnokov, S. Rowson, J.-M. Lourtioz, V. Berger, J.-Y. Courtois, An optical drill for the fabrication of photonic crystals, *J. Opt. A: Pure Appl. Opt.*, **1**, L3-L6, (1999).

7) R. Mäki-Ontto, K. de Moel, W. de Odorico, J. Ruokolainen, M. Stamm, G. ten Brinke, O. Ikkala, "Hairy tubes": mesoporous materials containing hollow self-organized cylinders with polymer brushes at the walls, *Adv. Mater.*, **13**(2), 117-121, (2001).

8) C.R. Martin, Nanomaterials: a membrane-based synthetic approach, *Science*, **266**, 1961-1966, (1994).

9) R.L. Fleischer, P.B. Price, R.M. Walker, Nuclear Tracks in Solids, (University of California Press, Berkeley, CA, 1975).

10) R.J. Tonucci, B.L. Justus, A.J. Campillo, C.E. Ford, Nanochannel array glass, *Science*, **258**, 783-785, (1992).

11) T.A. Desai, D.J. Hansford, L. Kulinsky, A.H. Nashat, G. Rasi, J. Tu, Y. Wang, M. Zhang, M. Ferrari, Nanopore technology for biomedical applications, *Biomed. Microdev.*, **2**(1), 11-40, (1999).

12) F. Laerme, A. Schilp, K. Funk, M. Offenberg, Bosch deep silicon etching: improving uniformity and etch rate for advanced MEMS applications, *Technical Digest IEEE Int. Conf. MEMS*, 211-216, (1999).

13) A. Lakhtakia, R. Messier, M.J. Brett, K. Robbie, Sculptured thin films (STFs) for optical, chemical and biological applications, *Innovations Mater. Res.*, **1**, 165-176, (1996).

14) E. White, E.C. Shors, Biomaterial aspects of interpore-200 porous hydroxyapatite, *Dental Clin. North Amer.*, **30**(1), 49-67, (1986).

15) E.W. White, Biomaterials innovation: it's a long road to the operating room, *Mat. Res. Innovat.*, **1**, 57-63, (1997).

16) O. Toader, S. John, Proposed square spiral microfabrication architecture for large three-dimensional photonic band gap crystals, *Science*, **292**, 1133-1135, (2001).

17) T. Rheinländer, D. Roessner, W. Weitschies, W. Semmler, Comparison of size-selective techniques for the fractionation of magnetic fluids, *J. Magn. Magn. Mater.*, **214**, 269-275, (2000).

18) K.D. Harris, A. Huizinga, M.J. Brett, High-speed porous thin films humidity sensors, *Electrochem. Solid-State Lett.*, **5**(11), H27-H29, (2002).

19) K.D. Harris, J. Sit, M.J. Brett, Fabrication and optical characterization of template-constructed thin films with chiral nanostructure, *IEEE Trans. Nanotech.*, In Press, (2002).

20) K.D. Harris, K.L. Westra, M.J. Brett, Fabrication of helically perforated thin films, *Mat. Res. Symp. Proc.*, **636**, D9.37.1-D9.37.6, (2001).

21) Filmtronics Inc., Box 1521, Butler, PA, 16003.

22) Oxford Instruments, Plasma Technology, Fremont, CA, 94538.

23) M. Ohring, The Materials Science of Thin Films, p.84, (Academic Press, San Diego, CA, 1992).

24) F.A. Lowenheim, Modern Electroplating, (John Wiley & Sons Inc., New York, 1974).

25) Canning Handbook on Electroplating, (W. Canning Ltd., London, 1978).

26) S. Kawai, R. Ueda, Magnetic properties of anodic oxide coatings on aluminum containing electrodeposited Co and Co-Ni, *J. Electrochem. Soc.*, **122**(1), 32-36, (1975).

27) H. Masuda, H. Tanaka, N. Baba, Preparation of porous material by replacing microstructure of anodic alumina film with metal, *Chem. Lett.*, **1990**, 621-622, (1990).

28) H. Masuda, K. Nishio, N. Baba, Fabrication of porous TiO_2 films using two-step replication of microstructure of anodic alumina, *Jpn. J. Appl. Phys.*, **31**, L1775-1777, (1992).

29) Krohn Technical Products, Carlstadt, NJ, 07072.

30) K.D. Harris, M.J. Brett, T.J. Smy, C. Backhouse, Microchannel surface area enhancement using porous thin films, *J. Electrochem. Soc.*, **147**(5), 2002-2006, (2000).

31) M. Seto, K. Westra, M. Brett, Arrays of self-sealed micro-chambers and channels, *J. Mater. Chem.*, **12**, 2348-2351, (2002).

32) K.D. Harris, K.L. Westra, M.J. Brett, Fabrication of perforated thin films with helical and chevron pore shapes, *Electrochem. Solid-State Lett.*, **4**(6), C39-C42, (2001).

Chapter Six

Applications of Perforated Thin Films

6.1 - Introduction

Some forms of perforated and replica thin films reported in this thesis represent entirely new thin film microstructures. For example, after extensive literature searches, no prior descriptions of films containing networks of helical or chevron pores could be located, and consequently, applications for such structures also remain completely unexplored. Therefore, in this chapter, two applications for perforated thin films are described in detail, and the results of investigations involving real PTFs are discussed.

6.2 – Perforated Thin Film Humidity Sensors

6.2.1 – Existing GLAD humidity sensors: Extremely sensitive humidity sensors fabricated using the GLAD technique were recently reported in the literature.[1,2] The devices consisted of partially capped helical films of SiO grown on Si substrates, and with these films, variations in capacitance over five orders of magnitude and response times less than 1s were reported. Because the microstructure and pore size scales for PTFs are of approximately the same magnitude as GLAD structures, similar humidity sensing devices were thought to be possible using the perforated thin films technique. Performance equivalent to or exceeding that of GLAD sensors was not necessarily expected, but operational PTF humidity sensors were constructed and their relative performance was evaluated.

6.2.2 – Construction of a perforated thin film humidity sensor: The sensing film in a capacitive humidity sensor acts as a moisture trap. Atmospheric water condenses inside the film, causing the effective dielectric constant, k, to increase. The higher the humidity, the greater the water content, and the greater the shift in k that is registered. By measuring the capacitance between electrodes on either side of the dielectric, one is thus able to indirectly measure the ambient humidity.

A conceptual diagram of a perforated thin film humidity sensor is shown in Figure 6.1. A metal electrode is deposited on an arbitrary substrate, and a PTF is fabricated over the electrode. Above the porous layer, a second metal electrode is formed having gaps to allow vapor to penetrate into the bulk of the sensor. Leads are then attached to the upper and lower electrodes to complete the sensor.

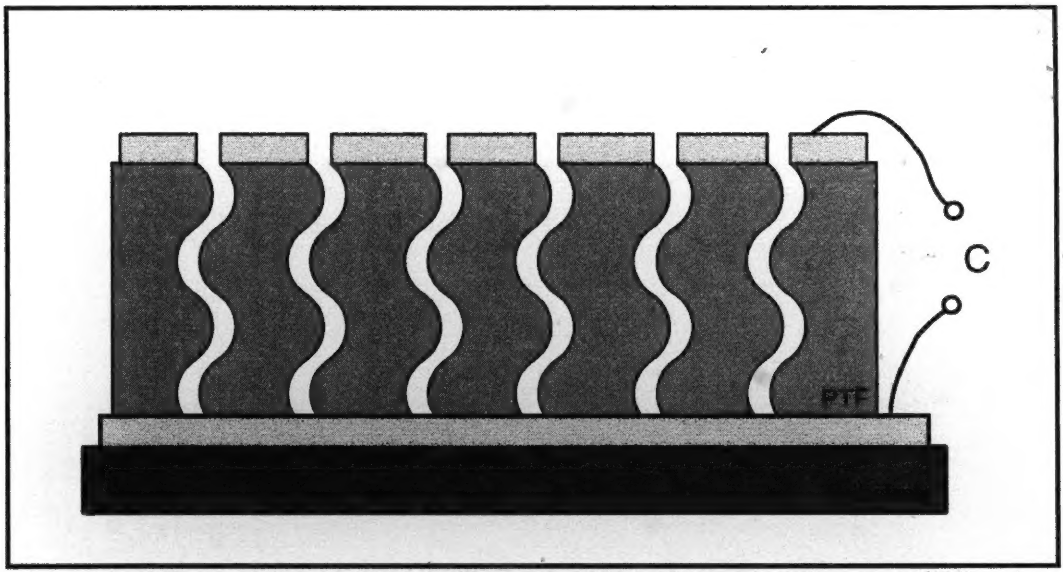

Figure 6.1 – Conceptual diagram of a helically perforated humidity sensor. Water vapour diffuses into the structure, altering the capacitance of the system. A measurement of capacitance may thus be used to gauge ambient humidity.

After several initial failures due to short-circuits between the metal electrodes, a practical process for fabricating these structures was realized. Cr electrodes were first deposited onto 4“ diameter Si wafers. The electrodes were 380nm thick, and they were found to be electrically continuous. Above the metal electrodes, a helical template, 1.38μm in thickness and composed of 3 turns, was deposited at 87°, and the film was filled and etched according to the PTF process.

During the deposition of the upper electrodes, a great deal of care was required in preventing short-circuits between the two metal layers. As an initial measure, hundreds of electrodes were formed in parallel, rather than relying on a single device of larger dimensions. To prepare these sensors, the upper electrode layer was deposited through a punched aluminum mask. Circular holes, 3mm in diameter and separated by 4.48mm in the two directions of a square array, were dispersed across the mask. As a proof of principle, the processing was only required to yield a single operating sensor. In order to prevent flux from penetrating directly to the lower electrode through crack or nodule defects in the structure, deposition through the mask occurred at a fixed azimuthal position (ϕ) and at $\alpha = 35^\circ$. In addition, the upper electrode was kept thin (215nm of Ti) to reduce the likelihood of short-circuiting between the upper and lower electrodes. Despite these measures, the majority of the on-chip devices were inoperative. A small minority, however, were fully functional and could be tested for humidity sensing properties. As an illustration of the characteristics of the physical sensors, a failed portion of the substrate was cleaved, and an SEM image is included as Figure 6.2. Both electrodes and the photoresist film are clearly identifiable in the image, and in addition, the breaks in the cap which were essential in allowing water to penetrate into the structure can also be seen. Because I was reluctant to destroy a working sensor, this particular device was non-operational, the failure mode probably involving the deposition of Ti atoms along structural cracks or defects during the evaporation of the upper electrode.

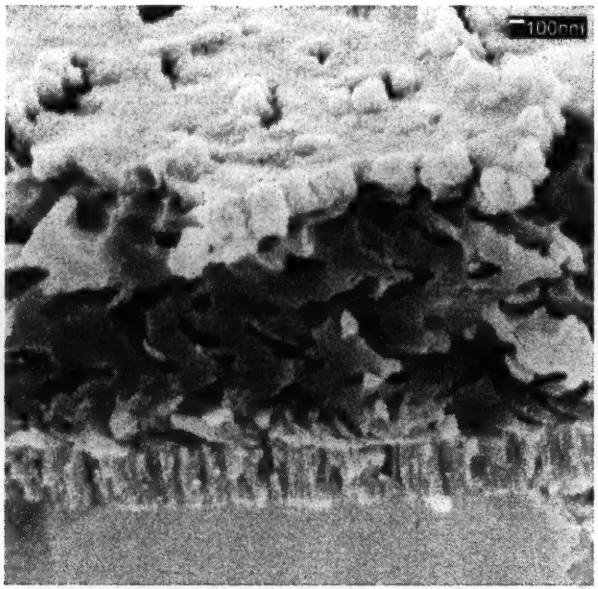

Figure 6.2 – The perforated thin film humidity sensor. A perforated thin film of photoresist is fabricated between metal electrodes, and the system capacitance is measured.

In order to evaluate the humidity sensing characteristics of the devices, electrical contacts with the two electrodes were required. At the lower electrode, this entailed attaching a lead using silver paint. At the upper electrode, however, silver paint was found to penetrate through the perforated film shorting out the electrode structure.

Instead, a simple pressure contact formed by pressing a spring-loaded, metal lead onto the upper electrode was employed.

6.2.3 – Sensor calibration: The substrate was placed in a humidity chamber which was designed specifically for these experiments, and the sensor capacitance was recorded as the humidity was swept between the relative humidity limits of the chamber. The results are located in Figure 6.3. (See Appendix A for a description of the operation and performance of the humidity chamber.)[2,3]

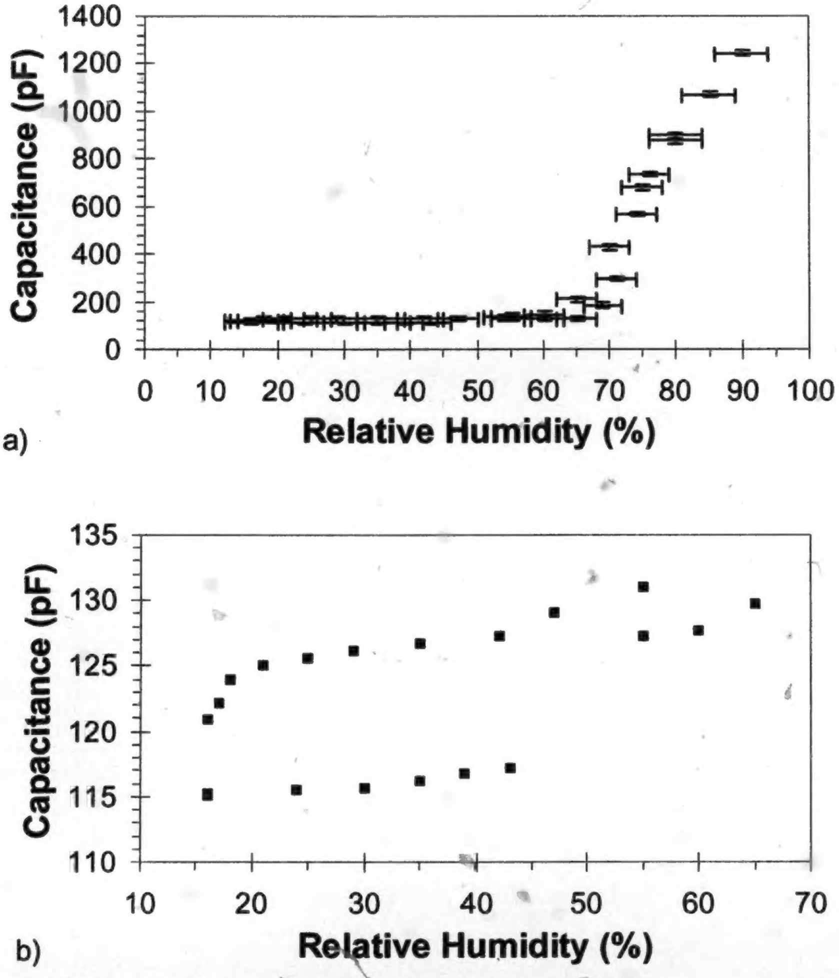

Figure 6.3 – Calibration of the PTF humidity sensor. The sensor capacitance was recorded at various chamber humidity values, and the results were plotted. The plot in a) represents the entire range of humidity values, while the plot in b) highlights variations over a limited range from 10-70%RH.

In the plot, the error bars in x (the humidity) are more substantial than those shown for y (the capacitance). Because the calibration takes place inside a humidity chamber, the PTF humidity sensors are being calibrated against a second device, in this case, a Vaisala RH/T probe.[4] In the specifications, the RH/T probe is reported as accurate to within 3% relative humidity between 20% and 80% RH, and to within 4% RH at all other humidity values. Therefore, this and most other commercial humidity sensors are inaccurate devices, and humidity chambers based upon them are correspondingly inaccurate. The measurement of capacitance with an RLC meter, by contrast, is well controlled, and therefore, the uncertainty on the y-axis is almost unnoticeable in the plot.

At low humidity values, the rise in capacitance with atmospheric moisture content is very slow. The slope is approximately linear, and by least-squares analysis, a rate of 0.33 pF/%RH can be estimated for this particular device. At roughly 62% an abrupt change occurs, and the sensor becomes remarkably sensitive over the remaining 62-90% range of the chamber. In this range, the linear regression slope is 46 pF/%RH.

6.2.4 – Response time: One of the most consistent drawbacks of the existing humidity sensor technologies, has been the inability of sensors to detect humidity changes on time scales less than about 1s.[5-11] However, since both GLAD and PTF humidity sensors consist of structures separated by large (>100nm) macropores, there are very few constrictions or long, extremely narrow pores, and the diffusion of water vapour into the structure is not impeded. Therefore, both sensor types were expected to exhibit extremely fast responses.

The sensor response time was tested by repeatedly subjecting the sensors to alternating bursts of moisture-saturated air and clean dry air from a pressure regulated supply. During the tests, the capacitive sensors were incorporated into an oscillator circuit, greater capacitance values leading to lower frequency oscillation. As part of a frequency-to-voltage converter, this signal was then converted to a digital signal and used to trigger one-shot inputs. Finally, the DC component of the output signal was extracted, and voltages proportional to the sensor capacitance were sent to an oscilloscope and recorded. (See Appendix B for a more detailed description of the testing circuit.)

Typical response curves for each sensor type are included in Figures 6.4a and 6.4b. In each case, a falling edge corresponds to the addition of water vapor to the system, while a rising edge occurs as dry air is added. The typical response of a GLAD sensor is found in Figure 6.4a, while that of a PTF sensor is found in Figure 6.4b. The average response time (between 10% and 90% of the final value) for a typical SiO GLAD humidity sensor to step-like variations in humidity was found to be 35ms as water vapor diffused into the sensor, and 25ms as vapor escaped. For the PTF sensor of Figure 6.2, the corresponding responses were 75ms and 175ms. In both cases, the performance of PTF sensors is exceeded by that of the original GLAD sensors, however, when the two are each individually compared to existing sensor technologies having response times on the order of one second, significant improvements are observed. The GLAD sensors respond in only 2.5% to 3.5% the time required of commercial sensors, while the PTF sensors respond within 7.5% to 17.5% of the time required for state-of-the-art commercial sensors.

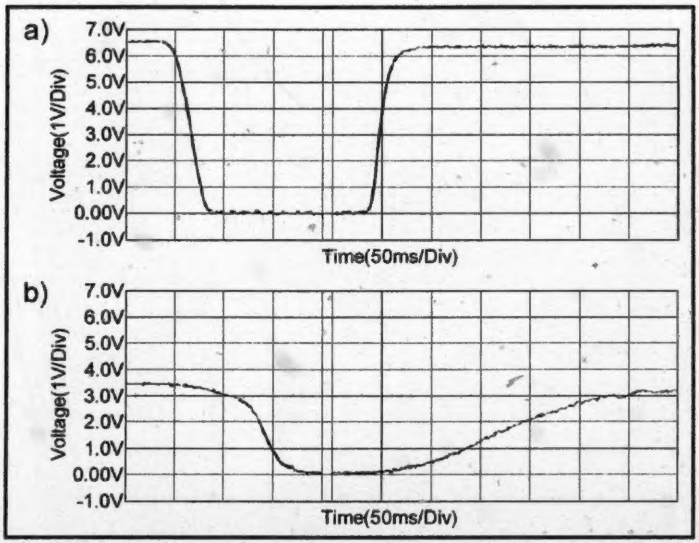

Figure 6.4 – Typical capacitance response curves. The response of a typical GLAD-based humidity sensor is shown in (a), while that of the PTF-based sensor described in this chapter is shown in (b).

6.3 – Optical Polarization Rotation by Perforated Thin Films

6.3.1 – Optical activity and theoretical considerations: Optically active thin films composed of materials which are not intrinsically optically active were first produced by Young and Kowal using oblique deposition onto rotating substrates.[12] The films studied in this case were non-porous fluorite films deposited at incidence angles between $\alpha = 30°$ and $\alpha = 60°$, and a maximum optical rotatory power of 0.155°/μm was recorded. When compared with common intrinsically optically active materials (such as quartz with an optical rotatory power of 21.3°/mm at 590nm) this represents a significant improvement. Some time ago, helically-nanostructured, porous GLAD films deposited at angles greater than $\alpha = 80°$ were also found to be optically active media.[13] Robbie, et al., reported a peak rotation of 2.1° for 560nm linearly polarized incident light.[13] Given the film thickness of 6.25μm, this represents an optical rotation of 0.33°/μm. More recently, similar chiral thin films with optical activity of up to 5.9°/μm were fabricated by a technique known as serial bideposition.[14,15] It is known that the optical activity in artificially produced media arises from the structural chirality of the films.[14,15] Thus, because the chiral structure of a helical template film can be transferred into a PTF, it is expected that the chiral optical properties are transferred as well.[16,17]

The origin of the optical rotation effect is as follows:[18,19] linearly polarized incident light may be visualized as a superposition of both right- and left-handed circularly polarized states. In an optically active medium, the index of refraction for the left-handed state differs from that of the right-handed state, and therefore, the two components move through the medium at different rates, creating a phase shift in the traveling wave. Assuming neither component is attenuated, the combination of light remains linear upon exiting the optically active medium, but it is phase rotated by an amount proportional to the thickness. The magnitude of the peak optical rotation is also determined in part by the refractive index contrast between the two materials forming the medium. (See Figure 6.5 for a definition of the positions of the materials.) In general, the greater the index difference between materials A and B, the greater the rotation observed.[20] The sign (direction) of rotation is determined by the combination of (a) the handedness of the columns or perforations, and (b) which of film materials A or B has the higher refractive index. For GLAD films used as templates in the fabrication of PTFs, the columns have refractive indicies ($n_A = n_{SiO2} \approx 1.47$) greater than that of the interstitial void regions which we assume to be filled with air ($n_B = n_{air} \approx 1.0$). After processing by the PTF technique, however, the formerly interstitial regions have a refractive index ($n_B = n_{filler} = n_{PR} \approx 1.6$)[21] greater than that of the newly etched helical perforations, which we again assume to be air-filled ($n_A = n_{air} \approx 1.0$). Using the standard sign convention, a left-handed film with $n_A > n_B$ produces a positive (clockwise, looking back at the light source) rotation of the plane of polarization of transmitted light. Its enantiomeric counterpart, a right-handed film having $n_A > n_B$, produces negative rotation. (The handedness of the films is controlled by the direction of rotation during evaporation; clockwise rotation generates right-handed (RH) helices, while counter-clockwise rotation generates left-handed (LH) helices.) PTFs are expected to exhibit rotation opposite in sign to the template films on which they are based due to the refractive index reversal of materials A and B. Thus, a left-handed PTF exhibits negative rotation, while a right-handed PTF exhibits positive rotation.

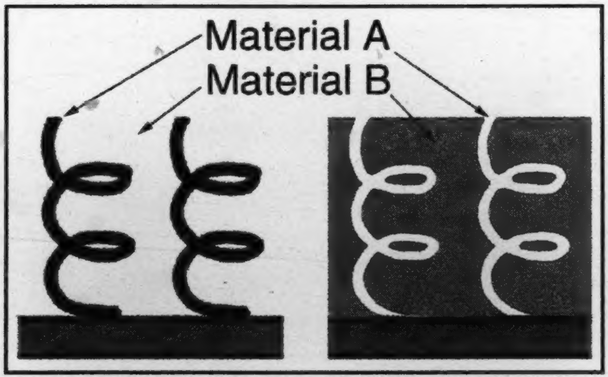

Figure 6.5 – Positions of the optical materials. Material A has a refractive index n_A, while material B has a refractive index n_B.

6.3.2 – Polarization rotation measurements: Four types of nanostructures were tested in these experiments: a RH helical film, a similar LH helical film, and the PTFs fabricated using each of these films as templates. Both template films were grown by EB-PVD of SiO_2 at $\alpha = 85°$. The RH film consisted of 12 turns of approximately 230nm helical pitch for a total thickness of 2.8μm. The LH film also had 12 turns but with a pitch of 320nm and total thickness of 3.8μm. Samples of each of the template films were filled with HPR504 photoresist to form the corresponding PTFs using the process described in Chapter 5. Because transparent substrates were required for the transmission mode measurements, the films were fabricated on glass substrates.

Rotation measurements (see Figure 6.6) were performed by the extinction (minimum transmission) technique using a PerkinElmer Lambda 900 spectrophotometer.[22] This method is based on the principle that light transmitted through two polarizers is minimized when the transmission axes are oriented at 90° to one another. With the addition of an optically active medium between the two polarizers, minimum transmission occurs when one polarizer is rotated slightly to compensate for the rotation caused by the optically active medium. The physical angle of rotation for that polarizer is then equal to the optical rotation caused by the medium. During a typical experiment, the analyzing polarizer is adjusted through a range of ±5.0° while wavelengths of light between 400nm and 1000nm are projected through the system. For each wavelength, the minimum detected intensity can be determined and plotted on a graph of rotation vs. wavelength. In every case encountered here, the measured rotation tended to become unstable at wavelengths above approximately 750nm. In order to simplify the presentation of the wavelength-dependent data, all the results which are quoted represent wavelength-averaged optical polarization rotations between 400nm and 650nm. Table 6.1 may be consulted for the results.[17]

Test Sample	Rotation (°)	Rotatory Power (°/μm)
Glass slide	-0.03	-0.00003
Photoresist coated glass slide	-0.07	-0.07
Left-handed template film	+0.49	+0.13
Right-handed template film	-1.53	-0.55
Left-handed perforated film	-1.48	+0.39
Right-handed perforated film	+3.93	+1.40

Table 6.1 – Polarization rotation of light by various films.

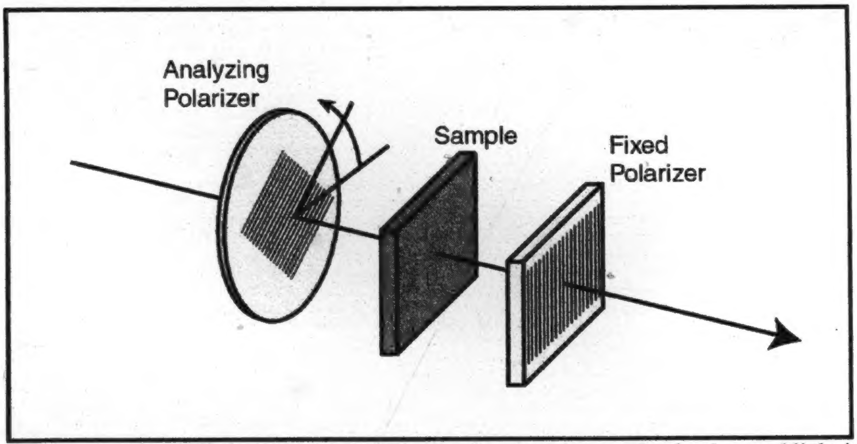

Figure 6.6 – The polarimeter concept. In the absence of a sample, the detected light intensity is minimized when the two polarizer crystals are crossed. On the insertion of an optically active sample, the analyzing polarizer must be adjusted to compensate for the optical activity of the sample. The magnitude of this adjustment describes the rotation from the sample.

The measurements for the four types of films yielded, in all cases, the expected qualitative results. The LH film produced positive rotation, while its corresponding perforated film caused negative rotation. For the RH film and its corresponding PTF, opposite rotations were observed. The magnitude of the optical rotation, however, is not well understood. In each case, the PTFs exhibited a stronger rotation than the original template films from which they were fabricated. For the LH and RH perforated films respectively, these rotations were 3.0 and 2.6 times stronger than those exhibited by their templates. Optical rotation was also measured for two control samples: a plain glass substrate of the same type used for the films, and a similar substrate coated with photoresist. Results for the control samples yielded no discernible rotation.

One contributing factor to the larger observed rotation in the PTFs may be the larger index contrast for the PTFs than the template films. For the PTFs, the index difference $|n_A - n_B| = |n_{air} - n_{PR}| \approx |1.0 - 1.6| = 0.6$ while for the template SiO_2 films, this difference is $|n_A - n_B| = |n_{SiO2} - n_{air}| \approx |1.47 - 1.0| = 0.47$. However, this index contrast for PTFs is only about 28% greater than that of the template films, thus suggesting that the index contrast alone cannot explain the entire effect. It was previously noted in Section 6.2 that water ($n_{water} = 1.33$) infiltrates porous films and condenses within them,[2] possibly leading to unwanted shifts in the optical characteristics of porous thin film media. If the index difference is recalculated for the PTFs and template films as above, but replacing

n_{air} with n_{water}, then the index contrast for PTFs is now 93% larger than that of the template films, which is more in keeping with the results shown. In addition, the surface chemistry (i.e., the hydrophilic or hydrophobic nature) of the two materials should be addressed. The difference in materials suggests that the template and perforated films are likely to adsorb different quantities of water into their voids at a given ambient humidity. As well, the template films, which generally have a lower areal density than the corresponding perforated films, are able to admit a greater total amount of water into their bulk. The precise manner in which water adsorbs onto the exposed surfaces and the effect this has on the optical rotation are both unknown, and therefore it is not surprising that the differences in magnitudes of the optical rotations between template and perforated films cannot be simply derived from differences in the index contrast. (The size and geometry of the equipment used precluded humidity control during optical characterization.)

Portions of this chapter have been excerpted from the papers entitled, "Fabrication and optical characterization of template-constructed thin films with chiral nanostructure",[23] which is scheduled to appear in IEEE Transactions on Nanotechnology, and "High-speed porous thin film humidity sensors",[24] which appeared in the November 2002 issue of Electrochemical and Solid-State Letters. The IEEE Transactions on Nanotechnology excerpts appear with the permission of the Institute of Electrical and Electronics Engineers, Inc., and the Electrochemical and Solid-State Letter was reproduced by permission of The Electrochemical Society, Inc.

References

1) A.T. Wu, M.J. Brett, Sensing humidity using nanostructured SiO posts: mechanism and optimization, *Sensors Mater.*, **13**(7), 399-431, (2001).

2) A.T. Wu, M. Seto, M.J. Brett, Capacitive humidity sensors with novel microstructures, *Sensors Mater.*, **11**(8), 493-505, (1999).

3) K.D. Harris, A. Huizinga, M.J. Brett, A simple and inexpensive humidity control chamber, *Meas. Sci. Technol.*, **13**, N10-N11, (2002).

4) Vaisala Oy, Helsinki, FIN – 00421.

5) U. Kang, K.D. Wise, A high-speed capacitive humidity sensor with on-chip thermal reset, *IEEE Trans. Electron Devices*, **47**(4), 702-710, (2000).

6) Y. Li, M.J. Yang, N. Camaioni, G. Casalbore-Miceli, Humidity sensors based on polymer solid electrolytes: investigation on the capacitive and resistive devices construction, *Sens. Actuators B*, **77**, 625-631, (2001).

7) A. Foucaran, B. Sorli, M. Garcia, F. Pascal-Delannoy, A. Giani, A. Boyer, Porous silicon layer coupled with thermoelectric cooler: a humidity sensor, *Sens. Actuators A*, **79**, 189-193, (2000).

8) K. Domansky, J. Liu, L.-Q. Wang, M.H. Engelhard, S. Baskaran, Chemical sensors based on dielectric response of functionalized mesoporous silica films, *J. Mater. Res.*, **16**(10), 2810-2816, (2001).

9) W. Qu, R. Green, M. Austin, Development of multi-functional sensors in thick-film and thin-film technology, *Meas. Sci. Technol.*, **11**, 1111-1118, (2000).

10) S. Chatterjee, S. Basu, D. Chattopadhyay, K.K. Mistry, K. Sengupta, Humidity sensor using porous tape cast alumina substrate, *Rev. Sci. Instrum.*, **72**, 2792-2795, (2001).

11) L.M. Zambov, C. Popov, M.F. Plass, A. Bock, M. Jelinek, J. Lancok, K. Masselia, W. Kulisch, Capacitance humidity sensor with carbon nitride detecting element, *Appl. Phys. A*, **70**, 603-606, (2000).

12) N.O. Young, J. Kowal, Optically active fluorite films, *Nature*, **183**, 104-105, (1959).

13) K. Robbie, M.J. Brett, A. Lakhtakia, Chiral sculptured thin films, *Nature*, **384**, 616, (1996).

14) I. Hodgkinson, Q.H. Wu, B. Knight, A. Lakhtakia, K. Robbie, Vacuum deposition of chiral sculptured thin films with high optical activity, *Appl. Opt.*, **39**(4), 642-649, (2000).

15) Q. Wu, I.J. Hodgkinson, A. Lakhtakia, Circular polarization filters made of chiral sculptured thin films: experimental and simulation results, *Opt. Eng.*, **39**(7), 1863-1868, (2000).

16) M.J. Brett, J.C. Sit, S.R. Kennedy, K.D. Harris, D.J. Broer, Optical behaviour of chiral thin film – liquid crystal composite materials, *Proc. SPIE*, **4658**, 112-118, (2002).

17) M.J. Brett, M.O. Jensen, J.C. Sit, S.R. Kennedy, K.D. Harris, D.J. Broer, Fabrication and optical behaviour of chiral thin film materials, *Soc. Vac. Coaters Annu. Tech. Conf. Proc.*, **45**, 238-244, (2002).

18) E. Hecht, Optics, pp. 309-314, (Addison Wesely, Reading, MA, 1990).

19) S.F. Mason, Optical activity and molecular dissymmetry, *Contemp. Phys.*, **9**, 239-256, (1968).

20) A. Lakhtakia, Enhancement of optical activity of chiral sculptured thin films by suitable infiltration of void regions, *Optik*, **112**(4), 145-148, (2001).

21) Pers. Comm., K. Westra, (2002).

22) PerkinElmer Instruments, Markham, ON, L3R-8E5.

23) K.D. Harris, J.C. Sit, M.J. Brett, Fabrication and optical characterization of template-constructed thin films with chiral nanostructure, *IEEE Trans. Nanotec*h., In Press, (2002).

24) K.D. Harris, A. Huizinga, M.J. Brett, High-speed porous thin film humidity sensors, *Electrochem. Solid-State Lett.*, **5**(11), H27-H29, (2002).

Chapter Seven

Sensor Applications of GLAD Thin Films

7.1 – Electrochemical Sensors

7.1.1 – The electrochemical sensor application: Prompted by an interest in probing the environment for dangerous levels of toxic gases, a great deal of research has been directed towards the production of increasingly effective sensors for gases such as H_2S and SO_2. In past literature, a number of sensing techniques have been described: electrochemical sensors employing liquid electrolytes[1,2] or solid polymer electrolytes (SPEs),[3-6] capacitance sensors,[7] and surface acoustic wave (SAW) sensors[8-9] are prominent examples. However, the detection threshold of many devices lie in the range of low-ppm or high-ppb. In the past, few designs have been capable of detecting trace gases in the low-ppb concentrations required of industrial emissions sensors.

Electrochemical sensors are currently gaining increasing favor. Their relatively high sensitivity, low power usage, selectivity to a single gas species, and their potentially small size and portability has led to sensor designs in applications such as fuel cells (methanol sensors),[10] petroleum refining (hydrogen sensors),[11] the identification of damaged transformers (acetylene sensors),[12] and most prominently, various devices for environmental monitoring.[13-19] Recently, effective electrochemical detection of SO_2 and H_2S has also been observed, with sensitivities reported in the low-ppb range.[6]

7.1.2 – Functionality of an electrochemical sensor: Electrochemical sensors operate by detecting the oxidation or reduction of the species of interest.[20] A typical sensor is arranged with a high conductivity acid or solid polymer electrolyte electrically connecting a sensing and a reference electrode. A bias which varies depending on the gas being detected is applied at the sensing electrode, and in the presence of the correct gas, chemical reactions occur at each electrode, leading to a net movement of electrons. In the amperometric mode,[21] the current detected between the electrodes is proportional to the dissolved gas concentration. In the case of H_2S, the primary reactions are:

At the sensing electrode:

$$H_2S + 4H_2O \longrightarrow SO_4^{2-} + 10H^+ + 8e^-$$

At the counter electrode:

$$2O_2 + 8H^+ + 8e^- \longrightarrow 4H_2O$$

And in total:

$$H_2S + 2O_2 \longrightarrow H_2SO_4$$

In a two-electrode configuration, current flowing through an electrochemical cell causes voltage variations at the electrodes.[22] To maintain the electrode potentials at fixed values, one must operate in a three-electrode configuration using a potentiostat to measure current. A potentiostat is an amplifier instrument that controls the potential difference between the sensing and reference electrodes by injecting current into the cell through a third electrode (called the counter electrode).[23] Voltage variations are eliminated between the reference and sensing electrodes because no current flows along this path. In this system, the measured variable is the counter electrode/sensing electrode current required to maintain the sensing electrode potential at the chosen value. Within the context of this section, the electrochemical sensors under consideration are all designed in a three-electrode configuration.

In many electrochemical cell designs, electrical contact between the electrolyte and the electrodes, and confinement of the electrolyte to the interior of the cell has been an issue.[24] Liquid electrolytes often leak from the housing in a dangerous manner, while solid polymer based systems do not effectively coat the electrodes. Solid polymer electrolytes, in addition, tend to trap a portion of the target gas within them, preventing accurate detection at the sensing electrode.[25] Furthermore, once all the gas has been removed from the environment, a fraction remains dissolved in the solid polymer. This component then escapes from the polymer slowly, significantly increasing the time for the oxidation current to return to the zero level.

The sensors described in this section address the problems through the incorporation of a porous GLAD electrolyte carrier layer. The layer consists of a porous hydrophilic film having a natural affinity for the electrolyte. The electrolyte penetrates the film by capillary action and, given a connected reservoir of electrolyte, continuously replenishes its supply. This eliminates the need for solid polymer electrolytes.

7.1.3 – Sensor production: The new, electrochemical gas sensors were fabricated in a three stage process. In the first deposition step, platinum counter and reference electrodes were deposited onto glass substrates. The substrates, 4" x 4" Corning 0211-type glass squares, were cleaned of organic residue in a solution of 3:1 H_2SO_4:H_2O_2. Type HPR504 photoresist was then spun onto the cleaned substrates, and using standard photolithograpy techniques, inverse images of the desired electrodes were patterned into the photoresist. The entire substrate was then sputter coated with 2000Å of platinum and immersed in an acetone bath. All of the platinum situated above photoresist coated areas was removed in this manner. This process is known as lift-off, and it is depicted graphically in Figure 7.1a-7.1e. The large substrate was then diced into smaller pieces, each having a distinct reference and counter electrode.

The second stage of sensor fabrication involves the deposition of the porous electrolyte carrier. In our system, the electrolyte carrier was composed of SiO_2 helices, as deposited by glancing angle deposition (Figure 7.1f-g). SiO_2 was chosen because it is strongly hydrophilic and well characterized. By deposition through a shadowmask, the GLAD film was confined to a circular area 21mm in diameter surrounding the reference and counter electrode structures. Two types of films were investigated. In each case, the helical portion of the films was deposited at an angle of 85° from the substrate normal, however, the degree of capping was varied between the two sensors. In the first type, the helical films were capped to a minimum incidence angle of 60°, resulting in a surface coverage of approximately 91%, while in the second type, capping continued to 0°, resulting in an estimated surface coverage of greater than 99%. (These percentage values were calculated using a graphics package known as NIH Image. The cross-sectional SEM images were first digitized using threshold and smoothing functions, leaving bright (greyscale value 0) or dark (greyscale value 255) pixels corresponding to the column and void regions. The average pixel brightness was then calculated from the digital image and divided by 255 to arrive at the percentage surface coverage.) These two sensor types will be referred to as 60° and 0° sensors. SEM images of each are shown in Figure 7.2.

At this stage in development, the hydrophilic nature of a porous GLAD film of SiO_2 was confirmed. To ensure the electrolyte carrier was functioning as expected, drops of distilled water were placed on the film with an eyedropper. The drops spread rapidly into the film, wetting all surfaces. Drops of dilute H_2SO_4 acted in the same manner.

Provision of a fixed reservoir above the film allowed any electrolyte removed by evaporation to be replaced quickly and automatically with fresh electrolyte.

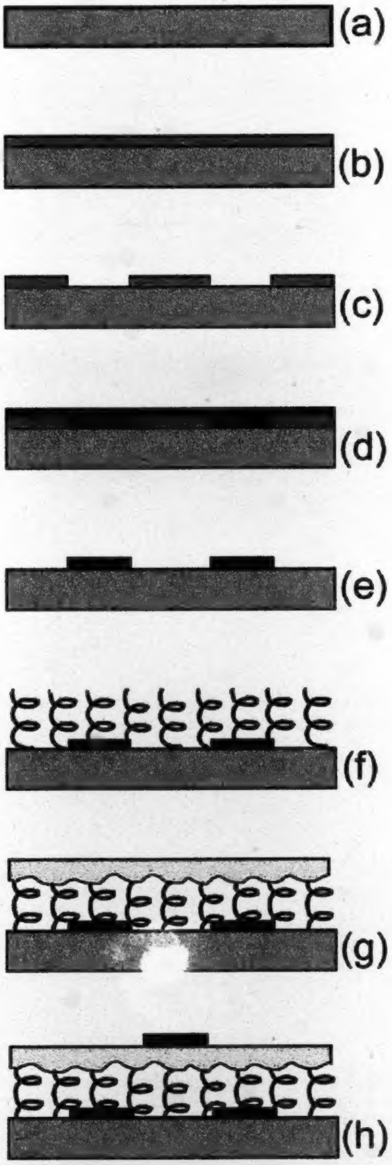

Figure 7.1 – Steps in the production of GLAD electrochemical gas sensors. Fabrication begins with a clean Si wafer (a), onto which a thin layer of photoresist is spun (b). This layer is then patterned (c) and coated in Pt (d). Immersion in acetone removes all photoresist, leaving patterned platinum electrodes (e). Subsequent steps involve the deposition of SiO_2 helices (f), an SiO_2 cap (g) and finally, the Pt working electrode (h).

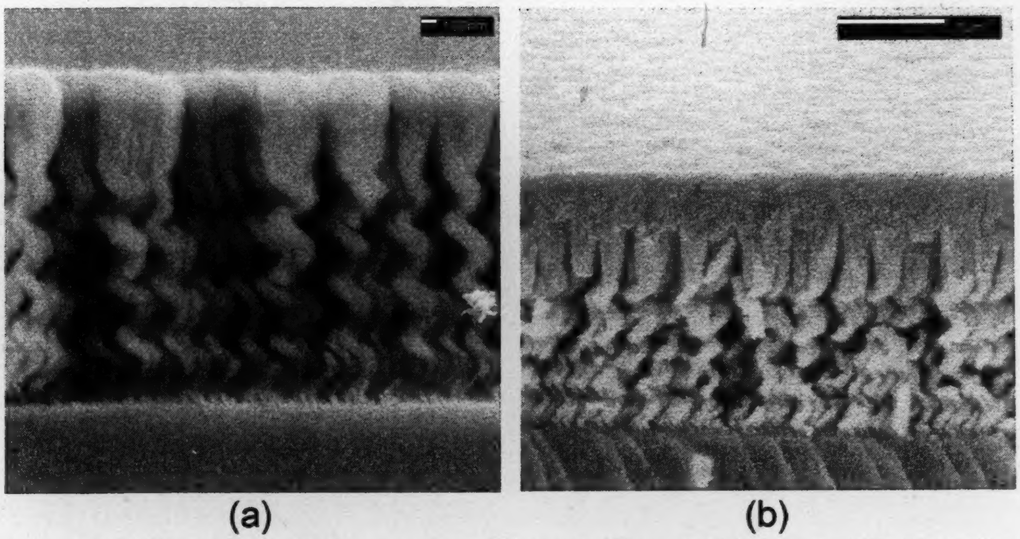

Figure 7.2 – SEM images of the porous electrolyte carrier films. In (a) is a porous SiO_2 GLAD film capped to 60° and in (b) is a similar film capped to 0°.

After GLAD deposition, the sensing electrode was deposited onto the capped GLAD film. By sputtering Pt through a second shadowmask, the sensing electrode was confined to an area between the counter and reference electrodes (Figure 7.1h). Since the GLAD layers are highly porous, there was some concern over the electrical continuity of films deposited above it, however, the Pt sensing electrodes deposited over GLAD films capped to both 60° and 0° were tested and found to be electrically conducting over their entire length. Unfortunately, sensors capped only to angles greater than 60° were not found to be sufficiently continuous to allow functioning electrodes to be deposited. A schematic diagram, with dimensions, of a completed sensor is shown in Figure 7.3.

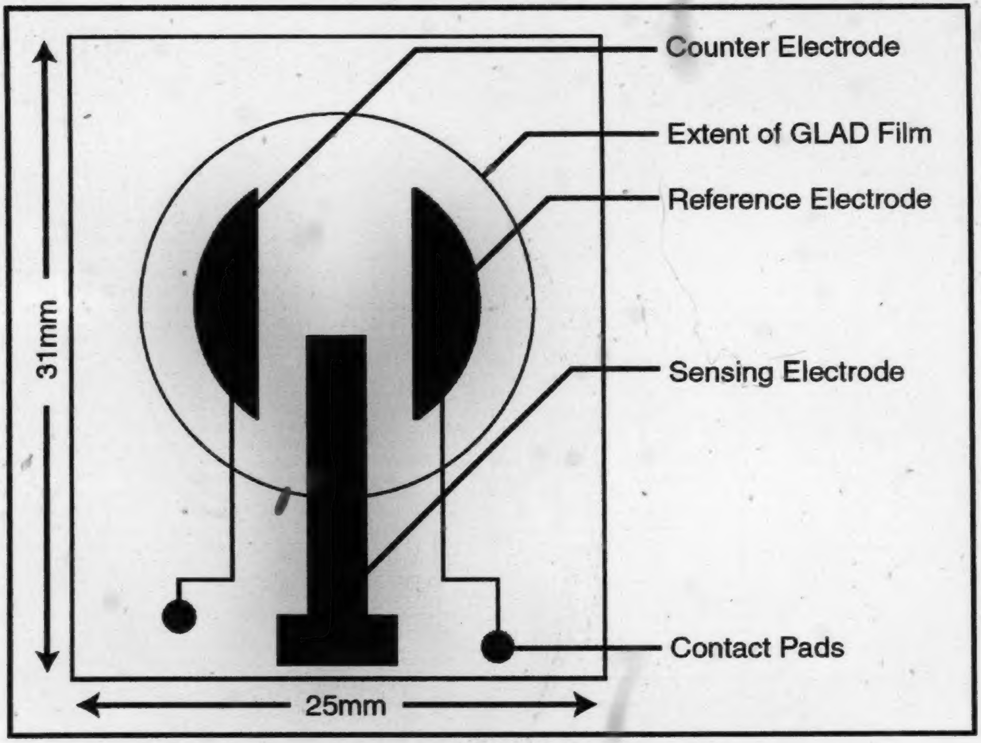

Figure 7.3 – Schematic diagram of an electrochemical sensor.

7.1.4 – Electrochemical testing: Prior to testing, each of the sensors was immersed in a 20% solution of H_2SO_4 for at least two hours in order to saturate the GLAD layer with electrolyte. After soaking in acid, the region surrounding the contact pads was carefully wiped free of electrolyte, wires were attached to the Pt contacts and the sensors were inserted in a gas-tight housing. Through inlet and vent ports in the housing, SO_2 infused gas was passed over the cell at flow rates between 25cc/min and 50cc/min. The gases of the desired H_2S and SO_2 concentrations were prepared by diluting, with mass flow controllers, appropriate amounts of nominal 2ppm H_2S or SO_2 with air. The input gas was maintained at 100% saturated humidity using a sparger.

All sensor response experiments were conducted by constant potential amperometry. With a potentiostat connected to the contact pads of the electrodes, a constant potential of 50mV with respect to the reference was maintained at the sensing electrode and under these conditions, the oxidation current was continuously recorded by computer. These tests were completed by A. Dalmia from PerkinElmer's research laboratories in Framingham, MA.

7.1.5 – SO_2 test results: Typical sensor responses to the application of an SO_2 sample are presented in Figures 7.4 and 7.5. In each case, 200ppb SO_2 infused air was introduced into the environment of the gas sensor for 60 seconds and abruptly removed. The response of the 60° sensor is shown in Figure 7.4, and in Figure 7.5, the response from the fully capped sensor is shown.

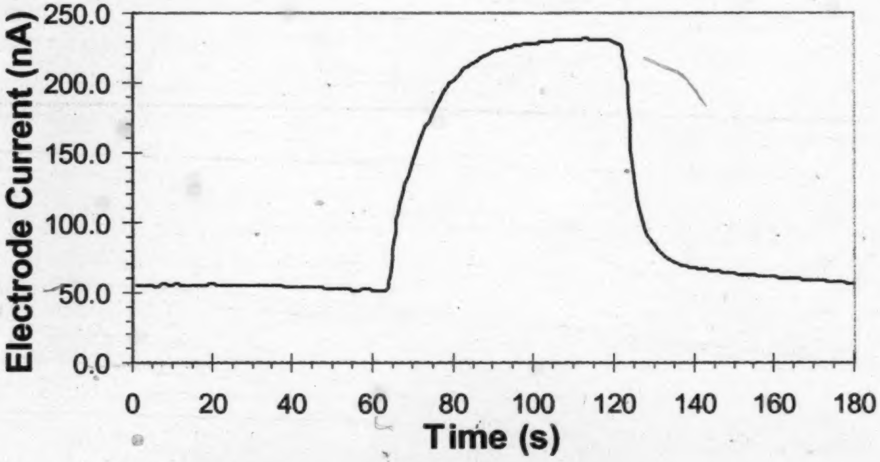

Figure 7.4 – Typical SO_2 oxidation current response for the 60° sensor. 200ppb SO_2 infused air was introduced into the vicinity of the 60° SO_2 sensor for 60s.

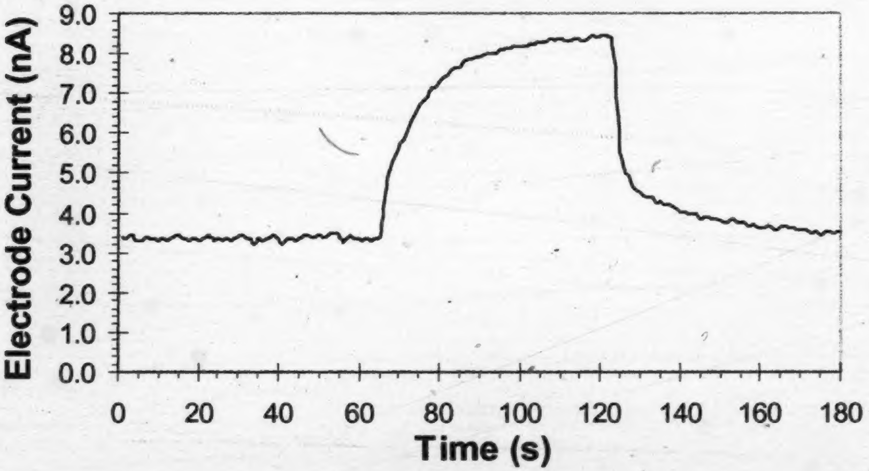

Figure 7.5 – Typical SO_2 oxidation current response for the 0° sensor. 200ppb SO_2 infused air was introduced into the vicinity of the densely capped (0°) SO_2 sensor for 60s.

At 200ppb, the densely capped film has a peak oxidation current response 5nA above its zero level, and the response of the less densely capped film is 179nA above its zero level. Clearly, the 60° sensor responds to SO_2 more strongly than the densely capped sensor. In either device, the capping layer acts as a membrane through which SO_2 must diffuse before dissolution of into the electrolyte may take place. The more permeable the membrane, the greater the fraction of atmospheric SO_2 that is able to diffuse through the cap, and the greater the signal that is recorded at the electrodes. In the 60° sensor, molecules penetrate through spaces between the columns, and an abundance of sample is present at the electrodes, while in the 0° sensor, the dense cap restricts the penetration of SO_2, and an associated reduction in oxidation current is observed.

The 60° sensor also responds to SO_2 faster than the 0° sensor. Using the time taken for the oxidation current to reach 90% of its maximum, the rise times of the 60° and 0° films were found to be 19s and 22s, respectively. Similarly, for the 60° and 0° sensors the time taken to return to 10% of the peak response was, respectively, 19s and 25s. Again, the diffusion of SO_2 across the cap is likely responsible for the slightly poorer performance of the 0° sensor. With such an effective barrier, a greater time is required to establish steady state concentrations of SO_2 within the electrolyte, and the achievement of the peak oxidation current is delayed in more densely capped sensors.

The ultimate sensitivity of these sensors to low levels of SO_2 is related to noise in the oxidation current measurements. In the 60° film, the background current varies by as much as 175pA, whereas in the 0° film, the background noise is only 30pA. However, if sensor response is considered, the nearly six-fold increase in noise is offset by a factor of 36 increase in signal. If a minimum signal to noise ratio (SNR) of 3 is considered the limit of reliable detection, one may estimate the threshold detection limits for the 60° and 0° sensors to be respectively, 0.6ppb and 4ppb.

Although less densely capped sensors consistently outperform their more densely capped counterparts, practical difficulties prevent the implementation of devices capped to even greater angles. For example, electrodes deposited on sensors capped to only 70°

were found to be electrically discontinuous along their length, and measurements on sensors of this type yielded no useful results.

7.1.6 – H_2S test results: Behaviour similar to that observed during SO_2 detection was also observed for H_2S gas. In a manner similar to the addition of SO_2, 200ppb H_2S gas was introduced into the vicinity of each GLAD sensor, and in Figures 7.6 and 7.7, typical response curves for the 60° and 0° sensors are included. As before, the 60° sensor is more sensitive to a given concentration than the 0° sensor, delivering a peak current 176nA above the zero level after the addition of 200ppb H_2S. The 0° sensor responds with a peak current 36nA above the zero level. The 60° sensor also responds faster than its counterpart, having rise and fall times of 21s and 30s, as compared to 29s and 33s measured for the 0° sensor. The zero level noise was once again lower in the fully capped device than in the more porous device. For the 0° sensor, the peak-to-peak noise was 78pA, while that of the 60° sensor was 92pA. Again, considering a SNR of three to be the threshold for reliable detection, one finds that the 60° and 0° sensors are capable of detecting 0.3ppb and 1.3ppb of H_2S gas.

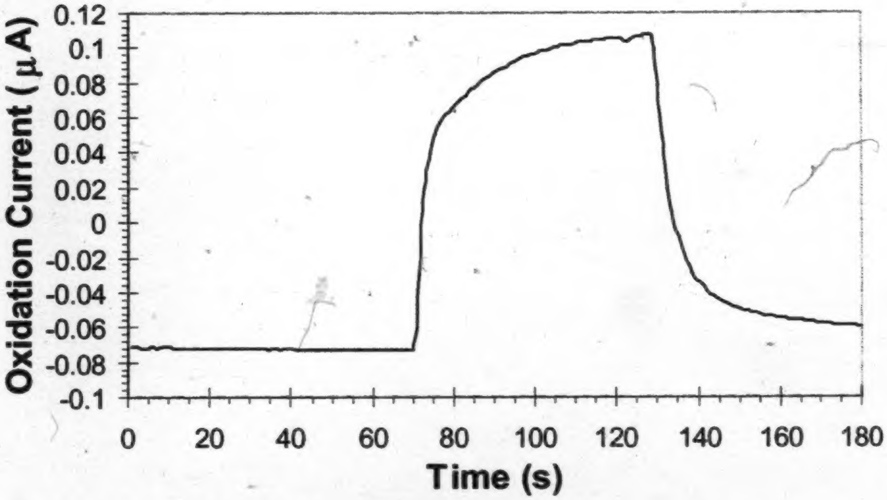

Figure 7.6 – Typical H_2S oxidation current response for the 60° sensor. 200ppb H_2S infused air was introduced into the vicinity of the 60° sensor for 60s.

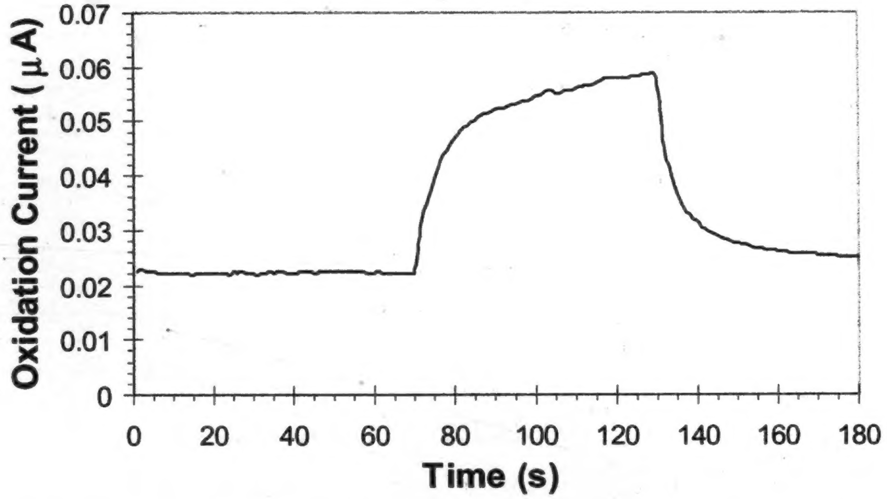

Figure 7.7 – Typical H_2S oxidation current response for the 0° sensor. 200ppb H_2S infused air was introduced into the vicinity of the densely capped (0°) SO_2 sensor for 60s.

7.1.7 – Advantages of GLAD gas sensors: These sensing structures provide sensitivity to trace gases on a level comparable to and often exceeding the existing state-of-the-art, lab-tested sensors.[6] But as an additional benefit, the absence of a solid polymer electrolyte prevents the trapping of gases within the sensor structure itself. This may lead to two advantages. First, since the target gas is removed from the structure quickly, the return-to-zero time in these sensors may be improved over SPE-based devices. Second, due to deterioration, the possibility exists that the sensor response to various trace gases may change over the lifetime of the sensor, and the initial sensor calibration at the point of manufacture may become inaccurate. The absence of an SPE binding gas within its structure may enable the implementation of a coulometric self-calibration scheme to correct this problem. After introducing a known quantity of gas into the vicinity of the sensor, the current may be recorded. Integrating over time, one is able to count the number of reactions taking place at the electrodes, and if such a known sample were periodically administered to each sensor, a device may be constantly recalibrated. Solid polymer electrolytes prevent this because gas particles trapped in the electrolyte are unaccounted for.

7.2 – Microcalorimetric Sensors

7.2.1 – The automotive hydrocarbon sensor application: Recently, environmental concerns have begun to prompt increasingly stringent government legislation regulating automotive fuel economy and emissions. Current rules not only mandate lower total emissions, but also require on-board diagnostics for monitoring vehicle exhaust. In order to satisfy these requirements, new and improved exhaust gas sensors are continually being developed to serve as part of the engine feedback control and emissions monitoring systems. Notable examples of the new technology include hydrocarbon sensors, whose primary use lies in the measurement of the efficiency of an engine's catalytic conversion.

Because it is reasonably inert, platinum has long been utilized as the material of choice for electrodes or catalysts. In a wide variety of applications (such as electrochemical sensors,[26,27] direct methanol fuel cells,[28-30] and electrochemical deposition systems[31]), thin film catalysts are already employed, but in each case, enhanced surface area has the potential to make significant improvements to the technology. Hydrocarbon sensors are a notable example: to rapidly detect hydrocarbons at low concentrations (as found in automotive emissions)[32], technologies such as silicon-based microcalorimeters have been developed.[33,34] These devices are simply resistance elements for temperature measurement patterned on two thin Si membranes. One membrane is covered with a catalyst material, while the other is left bare to establish a reference temperature. The oxidation of hydrocarbons at the surface of the catalyst coated membrane elevates the temperature with respect to that of the reference, thus providing a measure of the concentration of the hydrocarbons present. To achieve sufficient sensitivity from this type of sensor, it is crucial to incorporate a catalyst having a high activity and a large surface area, and in addition, all of the materials should be suitable for integration onto small, micromachined silicon devices. Obviously, these constraints pose challenges for catalyst development. Conventional catalyst materials, such as noble metals dispersed over high surface area alumina,[35-37] are not easy to integrate with standard microfabrication techniques and, furthermore, do not adhere well to the Si-based structures. However, alternate catalyst coatings such as sputtered noble metal films which adhere well and are easy to prepare also tend to have surface areas that are orders of magnitude too small for sensors adequate to hydrocarbon sensing applications.

In this section, the GLAD technique is utilized in the preparation of platinum thin films for calorimetric hydrocarbon sensors, and a preliminary investigation of the catalytic properties of such films is included.

7.2.2 – GLAD hydrocarbon sensors: For this experiment, Pt thin films of helical nanostructure were deposited onto silicon wafers. During the evaporations, the surface normal of the wafers was maintained at $\alpha = 85°$, and the system base pressure was approximately 1×10^{-4} Pa. An example of the resulting Pt films, shown in Figure 7.8a, consists of 1.2 turn helices, 215nm in pitch. The total thickness is 260nm.

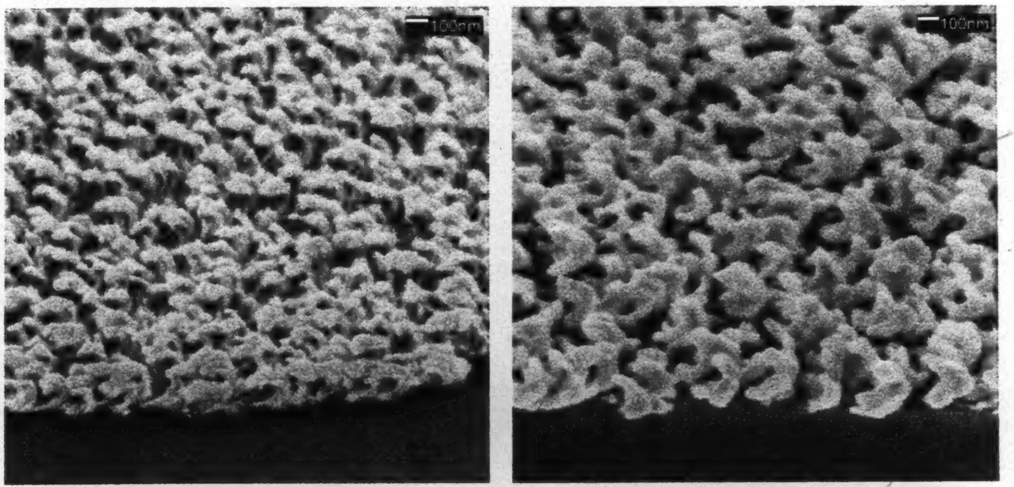

(a) (b)

Figure 7.8 – Catalytic test films. SEM images of the Pt GLAD film (a) prior to and (b) following annealing at 600°C.

After deposition, each specimen to be tested was cleaved from the wafer and, in an effort to stabilize the grain and microstructure of the film, annealed in air at a minimum temperature of 600°C for one hour. SEM images of the same Pt samples were taken both before and after annealing (Figures 7.8a and 7.8b), and the annealed Pt films showed three notable differences when compared to the as-deposited films. First, smaller Pt columns and nuclei on the substrate of the as-deposited film had agglomerated during the anneal process, leaving the substrate clear of the "undergrowth" that is common in GLAD films. (This "undergrowth" is the result of competition between small columns during the initial stages of film growth, before self-shadowing becomes well established.) Second, the helices themselves suffered some reflow such that the helical structure was barely evident, or completely destroyed. Finally, the film thickness has declined slightly from 260 nm to 230 nm. However, as may be seen in Figure 7.8b, the annealed films did maintain a high geometrical surface area.

By measuring the mass of a small (~145mm^2) Si substrate both prior to and following the chemical removal of the film, the density of the Pt coatings was estimated as 23.8% of the known bulk density of Pt. This is indicative of significantly increased porosity in the GLAD films and is consistent with values obtained for GLAD films fabricated of other materials.

Attempts to measure the surface area of these specific films by the method described in section 4.4 were unsuccessful due to SAW device failures; however, similar films composed of different materials were found to have surface areas ranging from 24 (for 110nm thick TiO_2 films) to 517 (for the 4.5μm thick SiO_2 films of Section 4.4) times the geometrical area of the sample. Because they are very thin, the films described here likely have surface areas in the lower end of this range.

7.2.3 – Catalytic testing: Representative samples of the Pt GLAD films deposited on Si substrates were evaluated for their catalytic performance in a gas flow reactor. (These tests were performed by J. McBride and K. Nietering of the Physics Department of the Ford Research Laboratory in Deerborn, MI.) For the microcalorimetric sensor application described above, conversion efficiencies for typical automotive exhaust species (CO, H_2, CH_4, C_3H_6, C_3H_8 and NO_x) are commonly measured as a function of temperature. In this initial set of experiments, data were acquired with either 0.5% CO, 0.1% C_3H_6, or 0.1% C_3H_8 as the combustible species. Computer operated mass flow controllers were used to combine the combustible components with oxygen at a redox ratio of 0.5 and N_2 as a carrier gas to bring the total gas flow to 250sccm. A fine thermocouple located adjacent to the sample measured its temperature. The reaction furnace was ramped at 10°C/min to ~500°C and then allowed to cool slowly back to room temperature. Concentrations of the combustible species were measured downstream of the reactor with gas analyzers from Rosemount Analytical.[38] Then, from the measured gas concentrations, the conversion efficiencies were determined.

For gas flow conditions typical of the intended microcalorimeter, observed conversion efficiencies can depend upon the geometric size and orientation of the sample in the gas flow stream. To address this issue, care was taken to mount every sample in an identical fashion in a quartz reactor having a rectangular, rather than circular, cross section. (This is illustrated below in Figure 7.9.) Identically sized samples were then compared against a reference sample in a systematic, repeatable fashion. The reference catalyst consisted of a 1cm^2 longitudinal slice removed from a commercially available automotive honeycomb monolith. This sample is a ceramic-supported Pd-based catalyst, which was chosen due to its high catalytic activity, high surface area and known noble metal dispersion patterns. "Supported" refers to systems where small clusters of catalytic atoms are dispersed on the surface of another material. The support tends to have high surface area, leading to a large catalyst surface area, and in many cases, chemical interactions between the support and catalyst are involved in the catalytic reaction. Non-supported, in contrast, refers to catalytic materials having a physical structure, not including the substrate, formed entirely of the catalyst itself. These materials are most often mechanically continuous and are not reliant upon the substrate during reactions.

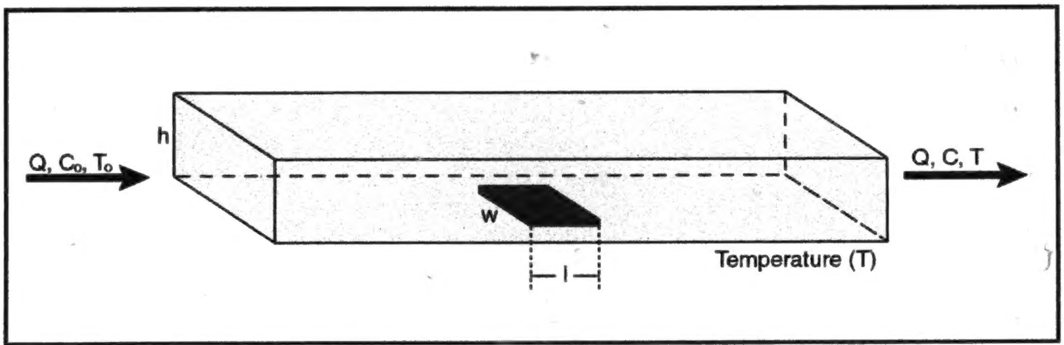

Figure 7.9 – The gas flow reactor. With the test film placed in the center of a rectangular chamber, a known concentration of hydrocarbon gas is forced in.

In the configuration of our gas flow reactor, a particular sample's conversion efficiency, η, may be theoretically derived by combining a number of fundamental, gas behavior equations.[39-41] The result is:

$$\eta = \sqrt{\frac{2D_o lw}{hQ}\left(\frac{T}{T_o}\right)^{0.75}} \left[1 - \exp\left(-\frac{\kappa_o T_o lwh}{Q}\frac{e^{-E/kT}}{T}\right)\right] \quad (7.1)$$

where D_o is the coefficient of binary molecular diffusion; l, w and h are the dimensions of the reactor; Q is the volumetric flow rate of the gas; T is the gas temperature in the reactor; T_o is the gas temperature at the mass flow controllers; κ_o is the rate constant for the reaction; E is the activation energy for the reaction; and k is Boltzmann's constant. (Refer to Appendix C for a derivation of this equation.)

At low temperatures, reactions are energy limited and the conversion efficiency increases dramatically with temperature. At higher temperatures, however, the reaction becomes mass transport limited, and the efficiency increases only modestly with temperature.[42] In a useful catalyst, the transition between the energy and mass transport limited regions occurs at a reasonably low temperature, ensuring that the catalyst is active over as large a fraction of potential operating conditions as possible. This is particularly relevant in the case of automotive catalysts: because the majority of automobile emissions occur during the "cold start" period of operation, before the engine has attained an optimum temperature, it is desirable to minimize the range of temperatures which are considered "cold".[43] Therefore, the most relevant measurable parameter is the "light-off temperature", defined as the temperature at which the conversion efficiency reaches half of the mass transport limited value.[44] The light-off temperature is related to the catalyst activity and the number of catalytic sites available on the sample, with a low light-off temperature being indicative of a good catalyst.

7.2.4 – The helical microstructure: Light-off curves for a Pt GLAD sample are shown in Figure 7.10. The data sets for each combustible species were collected independently, beginning with CO and followed subsequently by C_3H_6 and C_3H_8. These species were chosen for the initial tests since they most closely represent the primary constituents found in automotive exhaust. Among them, CO is the easiest to catalyze, C_3H_6 is representative of the "fast-burning" family of unsaturated hydrocarbons, and C_3H_8 is representative of the "slow-burning" family of saturated hydrocarbons.[45] Data were acquired with excess oxygen (*R*=0.5) in the gas stream to avoid peculiarities that might arise near stoichiometry, either from the limited accuracy of the mass flow controllers or from the underlying kinetics of the reaction.

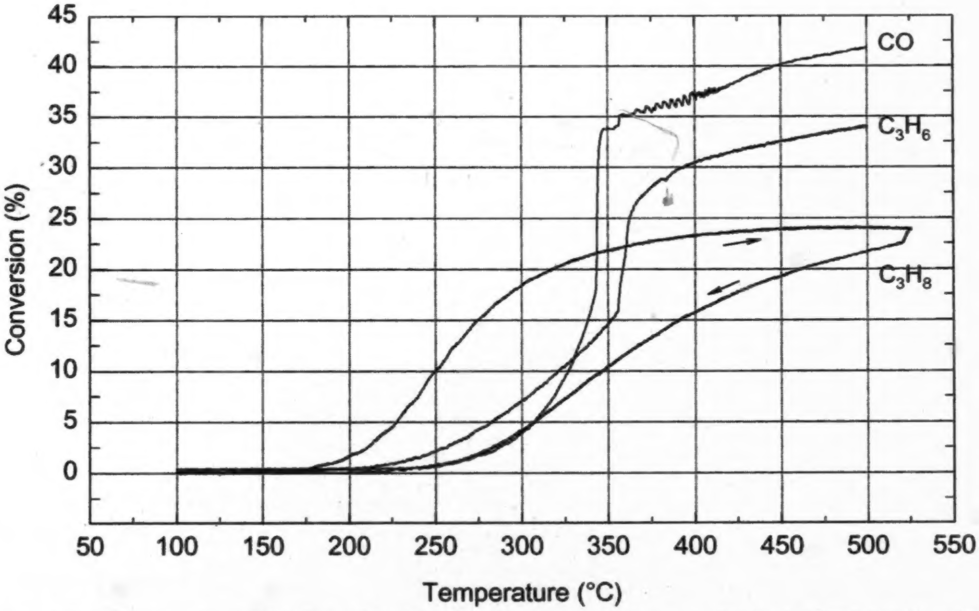

Figure 7.10 – Conversion efficiency of the Pt GLAD sample. Data were obtained at *R*=0.5 with 0.5% of CO, or 1000ppm of C_3H_6, or 1000ppm of C_3H_8 in a N_2 carrier gas at a flow rate of 250sccm.

The Pt GLAD catalyst shown in Figure 7.8b "lights-off" in CO at ~340°C, and for temperatures between 360°C and 420°C oscillations are observed in the CO conversion efficiency. (This is consistent with other observations of catalyzed CO conversion, since self-sustained CO oscillations on crystalline and polycrystalline Pt surfaces are well known and documented extensively in the literature.)[46] The catalyst lights off in C_3H_6 at ~360°C, a slightly higher temperature than for CO, and for C_3H_8, the catalyst lights off at ~270°C. In contrast to CO and C_3H_6, hysteresis is observed in the C_3H_8 conversion rate as the sample is cooled. Furthermore, each subsequent run (not shown in the figure) yields a reduced efficiency, until ultimately no conversion whatsoever is observed. In an attempt to identify the mechanism responsible for the reduction of efficiency, SEM analysis was once again employed, but no remarkable observations could be made. No evidence of additional column agglomeration could be found, and surface carbon deposits were not visible in the images. Despite this, it is likely that the catalytic surfaces have been fouled by contaminants during the conversion reactions. Extremely thin layers of non-catalytic materials are generally sufficient to inhibit catalytic activity while remaining invisible to SEM analysis. After repeated test cycles, a surface residue may build up on the GLAD structures, rendering them increasingly less efficient in conversion reactions. This is a phenomenon warranting further study. The test results are also found in tabular format in Table 7.1.

Sample	CO Light-off	C_3H_6 Light-off	C_3H_8 Light-off
Pt GLAD	340°C	360°C	270°C
Sputtered Sample	365°C	385°C	295°C
Honeycomb Catalyst	255°C	265°C	undetermined

Table 7.1 – Results of the catalytic test experiments.

Because conditions of enhanced shadowing will be in effect as long as substrates are held at highly oblique angles, thicker Pt films deposited by the GLAD technique will have greater surface areas. Thus, through the addition of catalytic sites, a thicker film leads to an increased rate constant, κ_o, and in turn, this may lead to improved conversion efficiencies and reduced light-off temperatures. If, however, conversion is limited by the diffusion of reactants through the porous structure to the catalytic sites, as occurs at high temperature, increasing the number of sites will not necessarily improve the conversion.

7.2.5 – Control samples: Other, non-supported Pt film samples exhibit behavior similar to that observed for the Pt GLAD film. The results from a Ford Research Laboratory standard 50nm thick Pt film deposited on Si by sputtering at normal incidence are shown in Figure 7.11. Because this film was deposited at normal incidence, atomic shadowing was not a dominant film growth factor, and the film lacks the enhanced surface area of the GLAD sample. The light-off profiles display the same general form as those seen from the GLAD sample, and characteristics such as the appearance of high temperature oscillations in the CO conversion rate, the hysteresis in C_3H_8 conversion, and the reduction and eventual cessation of C_3H_8 conversion are all present in the data gathered from the sputtered sample. This sample was, however, less active, having average light-off temperatures ~25°C higher than those of the GLAD sample.

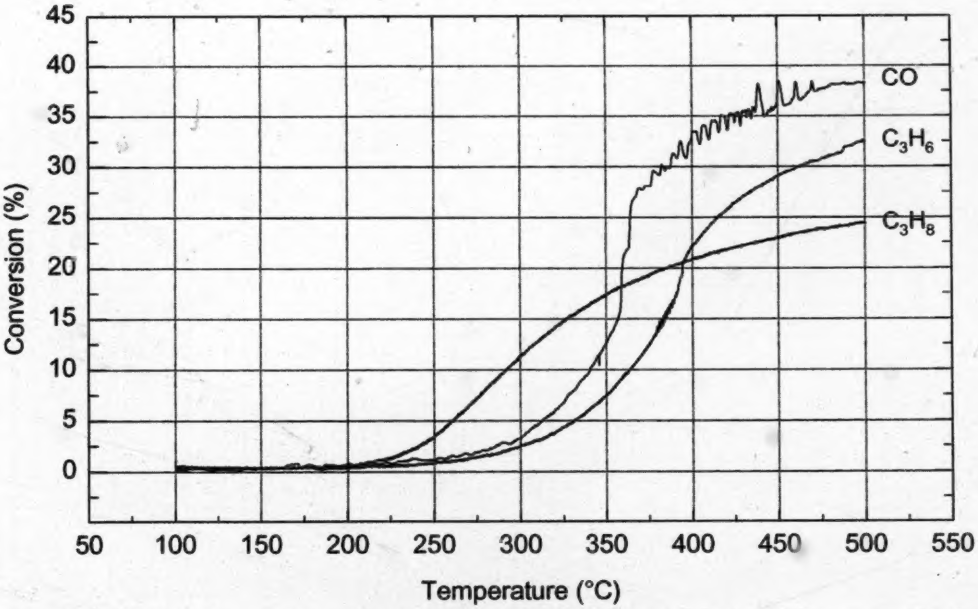

Figure 7.11 – Conversion efficiency of the sputtered sample. Experimental conditions were identical to those described in Figure 7.10.

Supported Pt catalysts have exhibited significantly better catalytic performance than either the GLAD or sputtered Pt samples.[47,48] Results, for example, were also collected from a more conventional catalyst, formed from Pt dispersed on high surface area alumina powder. This data is shown in Figure 7.12. For CO and C_3H_6, light-off temperatures were, respectively, 255°C and 265°C. For C_3H_8, the light-off temperature was more difficult to assess, since the conversion efficiency for this species is relatively poor and didn't reach its mass transfer limit during the test. Unlike the unsupported Pt samples, results from these supported films are reasonably reproducible and do not exhibit significant degradation in performance upon extended exposure to C_3H_8. Other noticeable differences include less abrupt light-off transitions and the lack of oscillations in the high temperature CO conversion efficiency. However, it must be recalled that these materials are not as compatible with silicon microfabrication techniques.

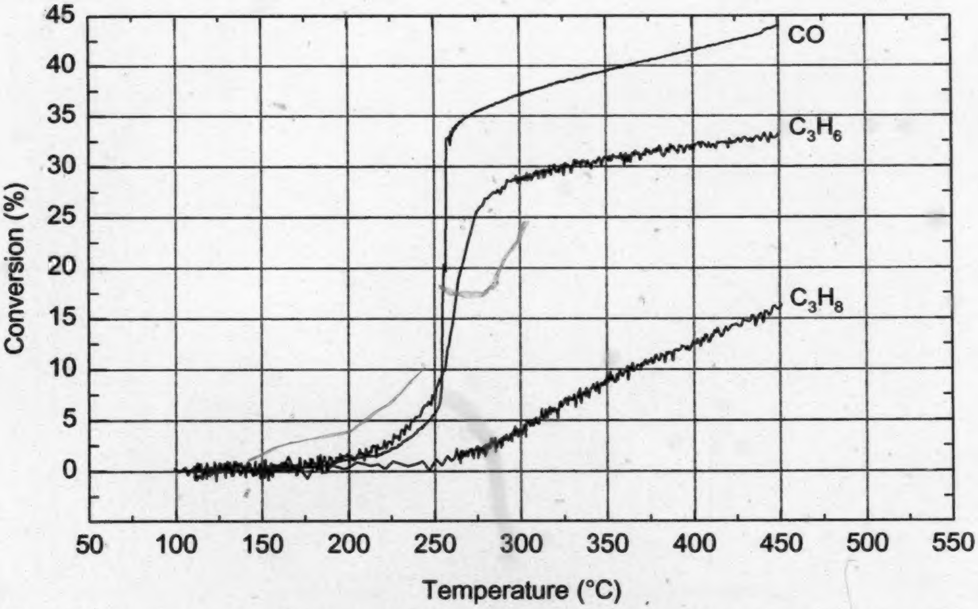

Figure 7.12 – Conversion efficiency of an alumina supported Pt catalyst. Experimental conditions were the same as those described in Figure 7.10.

7.2.6 – Comparison of results: Many of the differences observed between the unsupported (GLAD and sputtered) and supported Pt catalysts can be attributed to the size and microstructure of the Pt particles in the samples. Supported catalysts are characterized by small, well-dispersed Pt grains, while the unsupported catalysts are characterized by much larger grains and a higher degree of crystallinity. In addition, metal-support interaction can play an important part in the catalytic reaction,[49] as the support is often capable of storing oxygen and performing other catalysis-enhancing functions.[50] For catalysts intended as automotive sensors, however, supported systems are not applicable, and materials which are compatible with existing microfabrication techniques must be utilized exclusively. As such, that GLAD based catalysts demonstrate improvements over simple sputtered films actually represents a significant discovery, despite the fact that traditional systems perform better than either.

Sections of this chapter have been excepted from the paper entitled, "Fabrication of porous platinum thin films for hydrocarbon sensor applications", which appeared in the April, 2001 issue of Sensors and Materials.[51]

References

1) D.R. Shankaran, S.S. Narayanan, Chemically modified sensor for amperometric determination of sulphur dioxide, *Sens. Actuators B*, **55**, 191-194, (1999).

2) A.W.E. Hodgson, D. Pletcher, S. Sotiropoulos, A new approach to the design of amperometric gas sensors, *Sens. Actuators B*, **50**, 181-185, (1998).

3) S-D. Choi, W-Y. Chung, D-D. Lee, SO_2 sensing characteristics of Nascion electrolytes, *Sens. Actuators B*, **35-36**, 263-266, (1996).

4) J.F. Currie, A. Essalik, J-C. Marusic, Micromachined thin film solid state electrochemical CO_2, NO_2 and SO_2 gas sensors, *Sens. Actuators B*, **59**, 235-241, (1999).

5) Y. Jianhua, Y. Pinghua, M. Guangyao, A fully solid-state SO_x ($x = 2, 3$) gas sensor utilizing Ag-β" alumina as solid electrolyte, *Sens. Actuators B*, **31**, 209-212, (1996).

6) A.W.E. Hodgson, P. Jacquinot, P.C. Hauser, Electrochemical sensor for the detection of SO_2 in the low-ppb range, *Anal. Chem.*, **71**, 2831-2837, (1999).

7) M. Horn, J. Pichlmaier, H-R. Tränkler, Physical description of the principle of an SO_2 sensor, *Sens. Actuators B*, **24-25**, 400-402, (1995).

8) A. Leidl, R. Hartinger, M. Roth, H-E. Endres, A new SO_2 sensor system with SAW and IDC elements, *Sens. Actuators B*, **34**, 339-342, (1996).

9) Y.J. Lee, H.B. Kim, Y.R. Roh, H.M. Cho, S. Baik, Development of a SAW gas sensor for monitoring SO_2 gas, *Sens. Actuators A*, **64**, 173-178, (1998).

10) S.A.C. Barton, B.L. Murach, T.F. Fuller, A.C. West, A methanol sensor for portable direct methanol fuel cells, *J. Electrochem. Soc.*, **145**(11), 3783-3788, (1998).

11) Y. Tan, T.C. Tan, Sensing behavior of an amperometric hydrogen sensor: theoretical modeling and experimental verification, *J. Electrochem. Soc.*, **142**(6), 1923-1929, (1995).

12) L.R. Jordan, P.C. Hauser, Electrochemical sensor for acetylene, *Anal. Chem.*, **69**, 2669-2672, (1997).

13) N. Funazaki, S. Kume, A. Hemmi, S. Ito, Y. Asano, S. Yamashita, Development of catalytic electrochemical gas sensor for arsine, *Sens. Actuators B*, **B13**, 466-469, (1993).

14) N. Nakano, S. Ogawa, Preparation of thin gold-film electrode for an electrochemical gas sensor for phosphine and arsine, *Sens. Actuators B*, **B21**, 51-55, (1994).

15) M.J. Madou, T. Otagawa, Fast response time microsensors for gaseous and vaporous species, U.S. Patent No. 4,812,221, (1989).

16) J.R. Stetter, J. Maclay, Spin coating of electrolytes, U.S. Patent No. 4,795,543, (1989).

17) H. Yan, C.-C. Liu, A solid polymer electrolyte-based electrochemical carbon monoxide sensor, *Sens. Actuators B*, **B17**, 165-168, (1994).

18) A. Yasuda, N. Yamaga, K. Doi, T. Fujioka, S. Kusanagi, A planar electrochemical carbon monoxide sensor, *J. Electrochem. Soc.*, **139**(4), 1091-1095, (1992).

19) M.C. Simmonds, M.L. Hitchman, H. Kheyrandish, J.S. Colligon, N.J. Cade, P.J. Iredale, Thin sputtered platinum films on porous membranes as working electrodes in gas sensors, *Electrochimica Acta.*, **43**, 3285-3291, (1998).

20) R-I. Stefan, J.F. van Staden, H. Y. Aboul-Enein, Electrochemical Sensors in Bioanalysis, (Marcel Dekker, Inc., New York, 2001).

21) K.S. Alber, J.A. Cox, P.J. Kulesza, Solid-state amperometric sensors for gas phase analytes: a review of recent advances, *Electroanalysis*, **9**, 97-101, (1997).

22) A.A. Schneider, T.B. Scheffler, Potentiostat circuit for electrochemical cells, U.S. Patent No. 5,466,356, (1995).

23) R.K. Galwey, K.K. Kanazawa, Potentiostat for use with electrochemical cells, U.S. Patent No. 4,227,988, (1980).

24) Pers. Comm., Dr. O. Prohaska, PE Applied Biosystems Inc., (1999).

25) Pers. Comm., Dr. A. Dalmia, PE Applied Biosystems Inc., (1999).

26) L.B. Kriksunov, D.D. Macdonald, Amperometric hydrogen sensor for high-temperature water, *Sens. Actuators* B, **32**(1), 57-60, (1996).

27) J.D. Canaday, A.K. Kuriakose, T.A. Wheat, A. Ahmad, J. Gulens, B.W. Hildebrandt, Bonded solid protonic conductor/platinum electrochemical cells, *Solid State Ionics*, **35**(1-2), 165-175, (1989).

28) B. Beden, J.M. Leger, C. Lamy, Modern Aspects of Electrochemistry, **22**, (Plenum Press, New York, 1992).

29) A.J. Aplleby, F.R. Foulkes, Fuel Cell Handbook, (Van Nostrand Reinhold, New York, 1989).

30) H.P. Dhar, On solid polymer fuel cells, *J. Electroanal. Chem.*, **357**, 237-250, (1993).

31) J.M. Elliott, G.S. Attard, P.N. Bartlett, J.R. Owen, N. Ryan, G. Singh, A generic approach to electrodes with novel controllable continuous nanoarchitechtures, *J. New Mat. Elect. Syst.*, **2**(4) 239-241, (1999).

32) J. Franzen, R. Frey, H. Nagel, Fast monitoring of motor exhaust components by resonant multi-photon ionisation and time-of-flight mass spectrometry, *J. Mol. Struct.*, **347**, 143-152, (1995).

33) M. Zanini, J.H. Visser, L. Rimai, R.E. Soltis, A. Kovalchuk, D.W. Hoffman, E.M. Logothetis, U. Bonne, L. Brewer, O.W. Bynum, M.A. Richard, Fabrication and properties of a Si-based high-sensitivity microcalorimetric gas sensor, *Sens. Actuators A*, **48**, 187-192, (1995).

34) S.J. Gentry, T.A. Jones, The role of catalysis in solid-state gas sensors, *Sens. Actuators*, **10**, 141-163, (1986).

35) Y-F. Y. Yao, The oxidation of CO and hydrocarbons over noble metal catalysts, *J. Catal.*, **87**, 152-162, (1984).

36) G. Winterstein, M. Stahn, M. Voigt, G. Kühn, Ceramic honeycomb structures, **75**(9), 8-16, (1998).

37) B. Beguin, E. Garbowski, M. Primet, Stabilization of alumina toward thermal sintering by silicon addition, *J. Catal.*, **127**, 595-604, (1991).

38) Rosemount Analytical Inc., Process Analytic Division, Orrville, OH, 44667.

39) E. Butkov, Mathematical Physics, p. 298, (Addison-Wesley, Reading, MA, 1968).

40) R.J. Wijngaarden, A. Kronberg, K.R. Westerterp: Industrial Catalysis – Optimizing Catalysts and Processes, p.57, (Wiley-VCH, Weinheim, Germany, 1998).

41) S.R. Radel, M.H. Navidi, Chemistry, pp. 645, 666, (West, St. Paul, MN, 1994).

42) M.F.M. Zwinkels, S.G. Järås, P.G. Menon, T.A. Griffin, Catalytic materials for high-temperature combustion, *Catal. Rev. – Sci. Eng.*, **35**(3), 319-358, (1993).

43) J. Sun, N. Sivashankar, Issues in cold start emission control for automotive IC engines, *Proc. Am. Control. Conf.*, **3**, 1372-1376, (1998).

44) C.P. Please, P.S. Hagan, D.W. Schwendeman, Light-off behavior of catalytic converters, *SIAM J. Appl. Math.*, **54**(1), 72-92, (1994).

45) S.R. Radel, M.H. Navidi, Chemistry, pp.1114-1125, (West Publishing Co., St. Paul, MN, 1990).

46) R. Imbihl, G. Ertl, Oscillatory kinetics in heterogeneous catalysis, *Chem. Rev.*, **95**(3) 697-733, (1995).

47) S.R. Nakouzi, C.K. Narula, J.R. McBride, K.E. Nietering, J.H. Visser, A.A. Adamczyk, Novel concept prototype of low-power-consumption electrically heatable catalyst, *AIChE J*,. **44**(1), 184-187, (1998).

48) V.V. Khatko, E.M. Logothetis, R.E. Soltis, J.W. Hangas, J.R. McBride, Proceedings of the MTEC 2000 International Conference on Sensors and Transducers, 1, (MTEC, Birmingham, UK, 2000).

49) C.W. Hill, M.S. Nasher, A.I. Frenkel, J.R. Shapely, R.G. Nuzzo, Carbon support effects on bimetallic Pt-Ru nanoparticles formed from molecular precursors, *Langmuir*, **15**, 690-700, (1999).

50) E. Mamontov, T. Egami, R. Brezny, M. Koranne, S. Tyagi, Lattice defects and oxygen storage capacity of nanocrystalline ceria and ceria-zirconia, *J. Phys. Chem. B*, **104**, 11110-11116, (2000).

51) K.D. Harris, J.R. McBride, K.E. Nietering, M.J. Brett, Fabrication of porous platinum thin films for hydrocarbon sensor applications, *Sensors Mater.*, **13**(4), 225-234, (2001).

Chapter Eight

Thermal Barrier Coatings

8.1 – Traditional Thermal Coatings

Thermal barrier coatings (TBCs) are thin films comprised of low thermal conductivity materials which are applied to surfaces to be protected from intense heat.[1] Currently, the most prevalent use for TBCs lies in the protection of turbine engine components from high temperature failure.[2] In these systems, increased operating temperatures lead to greater fuel efficiency and reduced emissions, but they also lead to increasingly hostile working environments, and recently, in efforts to improve engine performance, critical components are often required to operate in environments at or above their normal melting temperatures.[3] Failure by thermal fatigue or oxidization is thus a critical problem, and temperature reduction schemes must be implemented for any components undergoing super-melting-point operation. Therein lies the role of the TBC: the sensitive components are coated with films of low thermal conductivity materials, effectively isolating them from the high temperature environments in which they operate.

Two prominent types of thermal barrier coatings have historically been applied to the problem. In the first, a layer of zirconia stabilized by the inclusion of yttria (i.e., yttria stabilized zirconia, or YSZ) is applied to critical surfaces by plasma spraying.[4] This tends to produce a highly porous microstructure (Figure 8.1a), and since the thermal conductivities for the known gases are generally considerably lower than that of bulk zirconia, the ability of heat to propagate across such a structure is low. However, YSZ and its substrate generally exhibit significantly different thermal expansion coefficients, and after repeated cycles of heating and cooling, induced stresses within the coating tends to cause cracking and spallation in the structure, rendering it ineffective.[5,6]

In a second deposition technique, stress induced deterioration is somewhat alleviated by the presence of a columnar microstructure. By EB-PVD, such a microstructure is produced, having grain boundaries oriented perpendicular to the substrate.[7-9] (Figure 8.1b) Some reduction of the residual film stress is observed because the microstructure is more laterally compliant.[9,10] Unfortunately, due to the lack of porosity in the structure, the thermal conductivity is somewhat greater than that of plasma sprayed coatings.[10]

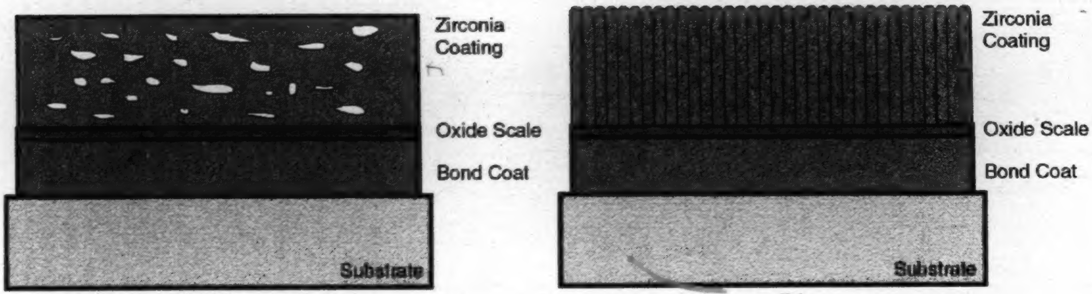

(a) (b)

Figure 8.1 – Traditional TBC schemes. In (a), a YSZ coating is plasma sprayed onto a prepared substrate, and in (b) the YSZ coating is electron beam evaporated. Each coating has innate advantages and disadvantages.

In applying the existing technologies, one is forced to choose between two mutually exclusive benefits. Engineers are permitted either greater operating temperatures and increased fuel efficiency at the expense of frequent part replacements, or extended component lifetimes at slightly reduced engine temperatures. In an effort to overcome this limitation and improve the thermal conductivity of TBCs while still allowing for the provision of expansion stress relief, an alternate structure can be proposed which is attainable by glancing angle deposition. Consider the illustration shown in Figure 8.2. First, as is the norm for glancing angle depositions, this microstructure would be deposited by EB-PVD, and therefore, all of the structural advantages of that technique should be realized in this microstructure. Because the grains in the solid capping layers are columnar in nature, the films will be laterally compliant, and expansion stress relief is available.[10] Second, even the incorporation of a few percent chevron porosity leads to significant reductions in the thermal conductivity of any structure,[11,12] and here porosity is present in abundance. Dense layers are included to provide some strength to the film, but they are also intended to prevent energy transfer by the movement of gaseous molecules between the ambient environment and the inner regions of the film. All the advantages of EB-PVD coatings are theoretically realized in this structure, and porous regions are expected to increase the thermal resistance. Thus, we have a potentially advantageous thermal barrier coating.

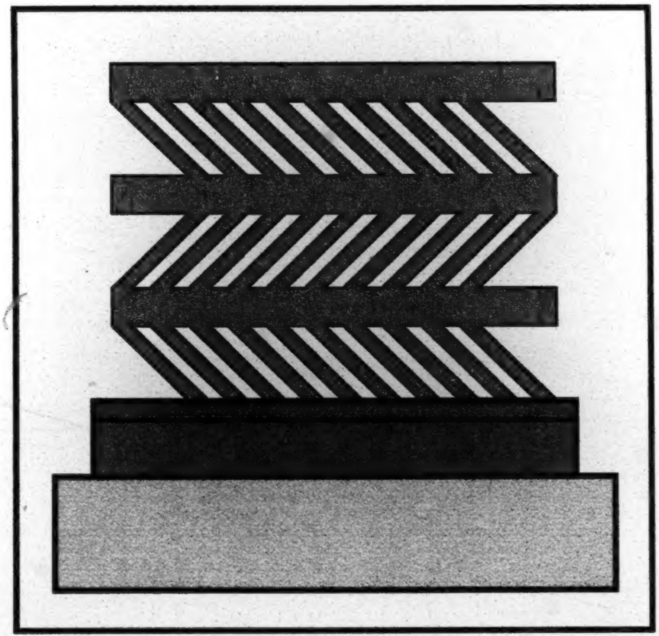

Figure 8.2 – The GLAD TBC microstructure. Because the coating is deposited by EB-PVD, expansion stress relief is available, yet due to the high porosity, the thermal conductivity is low.

8.2 – Deposition of YSZ Thin Films

In order to confirm that porous structure could be introduced into YSZ thin films, GLAD films of each of the standard microstructures were deposited from a YSZ evaporant source. Each of these films was deposited by EB-PVD with a flux incidence angle of 85° at base pressures less than 1mPa. Because zirconia has an extremely high melting temperature (2800°C), adatoms (or admolecules) have very little surface mobility, and well-controlled features are formed at glancing incidence. As an example, a porous thin film, 10μm thick and composed of posts slanted at an angle of approximately 60° from the vertical is shown in Figure 8.3a. Note the thin, fibrous nature of the growing columns and the limited columnar broadening despite the thickness of the particular film.

In all, six microstructures were deposited from the zirconia source: slanted posts, posts, helices, chevrons, capping layers, and as will be the focus of this chapter, the thermal barrier microstructure.[13] All of the films exhibited the high porosity and structural control which was sought, and they are expected to be highly compatible with thermal barrier applications. The critical film of the set is shown here as Figure 8.3b. In total, this film is 3.3μm thick, having alternating regions of porous and dense zirconia. From the substrate to the surface, the alternating layers are 1.2μm, 0.8μm, 0.5μm and 0.8μm in thickness. In the lowermost layer, the slanted posts have not grown in a direction parallel to the plane of the figure, and the column angle appears smaller than in reality. By weighing a portion of this film on its substrate, etching off the film and reweighing, the average density of the film was estimated as 42% of bulk density.

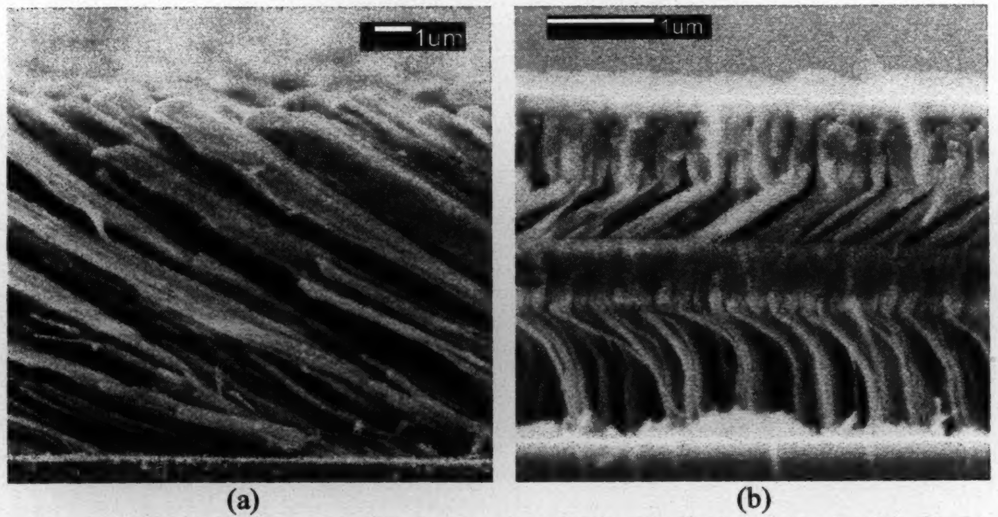

Figure 8.3 – GLAD structures of YSZ. In (a), a slanted posts thin film is presented, and in (b), the proposed thermal barrier coating.

It has been reported that layers of GLAD thin films may be stacked one atop the next to create thick multilayered structures,[14,15] however, most of these films were purely conceptual.[16] Therefore, in addition to being the first GLAD thin film designed for low thermal conductivity, the thin film of Figure 8.3b also represents one of the first multilayered GLAD structures to be achieved.

8.3 – Theoretical Thermal Conductivity Estimates

8.3.1 – Theoretical considerations: Attempts to theoretically predict the effectiveness of GLAD thin films in providing reduced thermal conductivity were undertaken in two distinct forms: mathematical modeling and simulation. In either case, the GLAD TBC structure is viewed as a complex network of thermal resistors, and from this structure, an analysis to determine the thermal characteristics of the system as a whole is undertaken.

In a heat flow problem, thermal resistors are analogous to the familiar resistive components of electrical circuits. Thermal resistance corresponds to electrical resistance, heat flow is analogous to current, and temperature is likened to voltage. Thus, using formulas common to circuit analysis, the resistance of a given region of a thermal barrier coating can be calculated, and the performance of a GLAD film with respect to conventional films can be estimated.

In Figure 8.4, a representation of one GLAD TBC bilayer is presented. In the porous regions, a large number of thermal resistors lie in parallel, but in the densest region only a single resistor representing the thermal characteristics of a large area is necessary (see inset). To arrive at a single, geometrical formula for resistance, the TBC must be broken into three distinct regions, denoted t_1, t_2, and t_3 in the figure. Each region has an thickness depending upon the deposition parameters, and in addition, the actual growth characteristics of GLAD thin films, including post broadening, cap evolution, and column angle, must be considered independently for each region. The total resistance of the system is a series combination of the three separate regions.

In order to arrive at meaningful equations, a number of simplifications are necessary. First, one must assume that no heat conduction occurs through the porous regions. In reality, air (or whatever combination of gases fills the voids in the structure) has a finite thermal conductivity, and a temperature difference across an air filled region will lead to heat flow through it. However, the thermal conductivities of all known gases are orders of magnitude smaller than that of zirconia, and so any heat flowing through voids in the structure will be negligible when compared to heat flow through the solid regions. Second, because I am without firm information regarding the grain structure of these films, I have assumed that the solid portion of a coating is composed of only a single grain. Grain boundaries have a deleterious effect on the thermal conductivity,[17,18] and therefore neglecting this contribution may lead to a slight overestimation of the coating's thermal conductivity. Finally, I have assumed that all heat flow occurs by heat conduction through the film rather than by convection currents or thermal radiation. Because the void regions are miniscule, the neglect of the convective component is justifiable, but unfortunately, a significant radiative heating effect in thermal coatings has been identified and cannot be accounted for by simple thermal resistance calculations.[19] In order to include this contribution, it would be necessary to solve Laplace's equation with a z-dependent heat generation term throughout the thickness of the film.

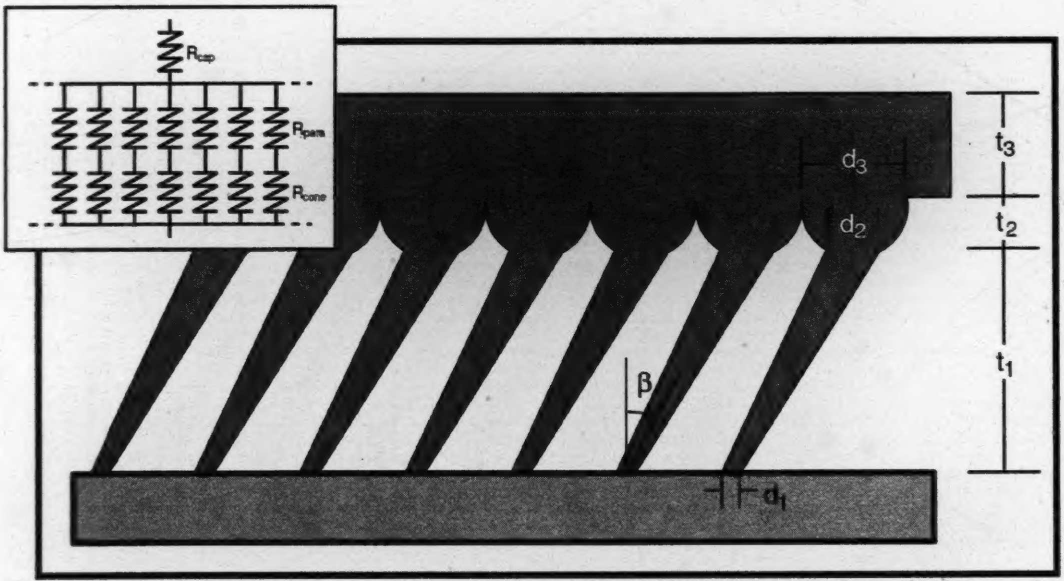

Figure 8.4 – Factors in the theoretical determination of thermal resistance. The thermal resistance of a TBC microstructure can be calculated by considering the film in three separate sections of thickness t_1, t_2 and t_3.

The equation for the perpendicular thermal resistance of a given area of material is:

$$R = \int_{z_1}^{z_2} \frac{\rho(z)}{A(z)} dz \qquad (8.1)$$

where $\rho(z)$ is the thermal resistivity at a particular position, z, within the film, A(z) is the cross-sectional area through which heat may be conducted at the same position, and z_1 and z_2 are the bounds of the region under analysis. Because the evaporant is not altered during a typical deposition, we will assume the thermal resistivity is a constant, ρ, throughout the film.

In the region nearest the substrate, the structures are inclined, truncated cones having diameter d_1 at their bases and d_2 at their tips. The cross-sectional area through which heat may flow is always circular, and thus the area (as per equation (8.1)) must be defined by:

$$A_{cone}(z) = \frac{\pi}{4} d(z)^2 \qquad (8.2)$$

where d(z) is the diameter of the conducting area at the position, z, within the film. The equation describing d(z) within the film is a simple linear relation:

$$d(z) = \left[\frac{(d_2 - d_1)}{t_1} \cos(\beta) \right] z + d_1 \qquad (8.3)$$

To calculate the thermal resistance of an inclined, truncated cone, one combines equations (8.3), (8.2) and (8.1) and integrates over the full thickness of the layer. The result is:

$$R_{cone} = \frac{4\rho t_3}{\pi d_2 d_3 \cos(\beta)} \qquad (8.4)$$

The second region can be approximated as a collection of truncated paraboloids, where in each individual structure, the cross-sectional area through which heat may flow is always circular. In this case, it is most convenient to define the area by:

$$A_{para}(z) = \pi r(z)^2 \qquad (8.5)$$

where r(z) is the radius of the heat conducting region. As before, we integrate over the thickness of the paraboloid to calculate its resistance. In a slice through a single structure perpendicular to the substrate, the equation of the curve defining the bounds of the paraboloid will take the form:

$$(r-h)^2 = 4p(z-k) \qquad (8.6)$$

where (r, z) are points on the parabola, (h, k) are the coordinates of the vertex, and p is the distance between the vertex and focus. Repositioning the origin in the center of the lower truncated face, we can define the coordinates of two points on the surface, $(r_2, 0)$ and (r_3, t_2), where r_2 and r_3 are respectively $d_2/2$ and $d_3/2$. With this, an equation for r(z) at any point on the surface can be developed:

$$r(z)^2 = \frac{(r_3^{\,2} - r_2^{\,2})}{t_2}\left[z + \frac{r_2^{\,2} t_2}{r_3^{\,2} - r_2^{\,2}}\right] \qquad (8.7)$$

Now, the equation for resistance (8.1) can be integrated in cylindrical coordinates, and the resistance of any one structure can be found:

$$R_{para} = \frac{\rho}{\pi}\left(\frac{t_2}{r_3^{\,2} - r_2^{\,2}}\right)\ln\left[\frac{r_3^{\,2}}{r_2^{\,2}}\right] \qquad (8.8)$$

In the dense capping region, both A(z) and ρ(z) are constant, and it is a simple matter to integrate equation (8.1) to find the thermal resistance:

$$R_{cap} = \frac{\rho t_3}{A} \qquad (8.9)$$

Now, by combining the three equations (8.4), (8.8) and (8.9) in series, and assuming that there are n heat conducting cone/paraboloid structures in the porous regions of an arbitrary area under analysis, A, we can arrive at the total resistance of the TBC structure:

$$R_{TBC} = \rho\left[\frac{t_3}{A} + \frac{8}{n\pi}\left(\frac{t_2}{d_3^{\,2} + d_2^{\,2}}\right)\ln\left(\frac{d_3}{d_2}\right) + \frac{4t_1}{n\pi d_2 d_1 \cos(\beta)}\right] \qquad (8.10)$$

And so, one can see that thicker films, finer structures, and greater column inclinations lead to more pronounced thermal resistance.

Because expression (8.10) is dependent upon A, the results are most useful when compared to a second, more traditional thermal coating of equal thickness. As was mentioned previously, modern turbine engine coatings consist of ZrO_2 films which have been electron beam deposited at normal incidence, (see Figure 8.1b). Because these films represent the current state-of-the-art, they will serve as effective benchmarks, and because they were deposited at normal incidence, it is a simple matter to estimate their resistance:

$$R_{trad} = \frac{r(t)}{A} \qquad (8.11)$$

The formulae may now be used to compare the theoretical performance of GLAD TBC films to traditional coatings using the geometrical parameters of physical GLAD TBCs. In the film of Figure 8.3b, there are two separate TBC bilayers, and in order to analyze the film, each must be considered separately and the two results added together in series. Estimates of all the necessary geometrical parameters (taken from SEM images) and the results of the thermal calculations are shown in Table 8.1. The final result may be found in the lowermost box, labeled "Total".

Layer	Parameter	Value	Layer	Parameter	Value
Upper	n	42	Lower	n	42
Upper	β	55°	Lower	β	55°
Upper	A	$4\mu m^2$	Lower	A	$4\mu m^2$
Upper	t_1	565 nm	Lower	t_1	520 nm
Upper	t_2	270 nm	Lower	t_2	150 nm
Upper	t_3	565 nm	Lower	t_3	1190 nm
Upper	d_1	210 nm	Lower	d_1	195 nm
Upper	d_2	120 nm	Lower	d_2	90 nm
Upper	d_3	90 nm	Lower	d_3	75 nm
Upper	R_{TBC}	$\rho(4.32\mu m^{-1})$	Lower	R_{TBC}	$\rho(9.68\mu m^{-1})$
Total	R_{TBC}	$\rho(14.0\mu m^{-1})$			

Table 8.1 – Measured parameters for TBC calculations.

The equation is simpler for the case of the dense film, and the result is $R_{trad} = \rho(0.82\mu m^{-1})$. When this is compared to the GLAD TBC, we see:

$$\frac{R_{TBC}}{R_{trad}} = 17.1$$

Therefore, the theory predicts a substantial improvement in thermal resistance when GLAD films are applied in thermal barrier applications. Unfortunately, a great deal of uncertainly is introduced in measuring all the parameters required by the resistance equations, and in order to circumvent the difficulty and develop more accurate models of the TBC films, it is necessary to move to computer-based, stochastic simulations of the thermal properties. With computer models, the simulated films assume something nearer the true shape of their physical counterparts, and heat flows can be determined on a much smaller scale. As a result, it is possible to calculate the thermal resistance to much greater accuracy, provided an accurate virtual representation of a physical film can be created.

8.3.2 – Thermal conductivity measurement by simulation: In a simulation, the inherently complex structure of a GLAD film presents a challenging heat flow-modeling problem. First, a realistic, three-dimensional model of the film's physical structure must be created, and then the heat flows within the model must be calculated before the thermal properties can be resolved.

In addressing the first problem, the 3D-FILMS simulation package was again employed,[20,21] and a virtual model of a thin film consisting of 1.0μm of YSZ deposited at 82° and with a 300nm YSZ capping layer was created. (This simulated thin film is shown in Figure 8.5a.) Using 3D-FILMS, the cap density was found to be 91%, the density of the porous layer was approximately 46%, and the total average film density was 56%.

In the second part of the problem, a solution of the heat flow equation for a 3D-FILMS simulation requires a numerical finite difference analysis of Laplace's equation. As before, the model for the steady state temperature distribution was developed assuming the absence of heat sources and sinks, and that convection, radiation and conduction through the void regions were negligible components of the total heat flow. To solve Laplace's equation, the blocks forming the virtual model were used to form a thermal network of miniature resistors, and a solution was found by iterating until the heat flow in each element had zero divergence.

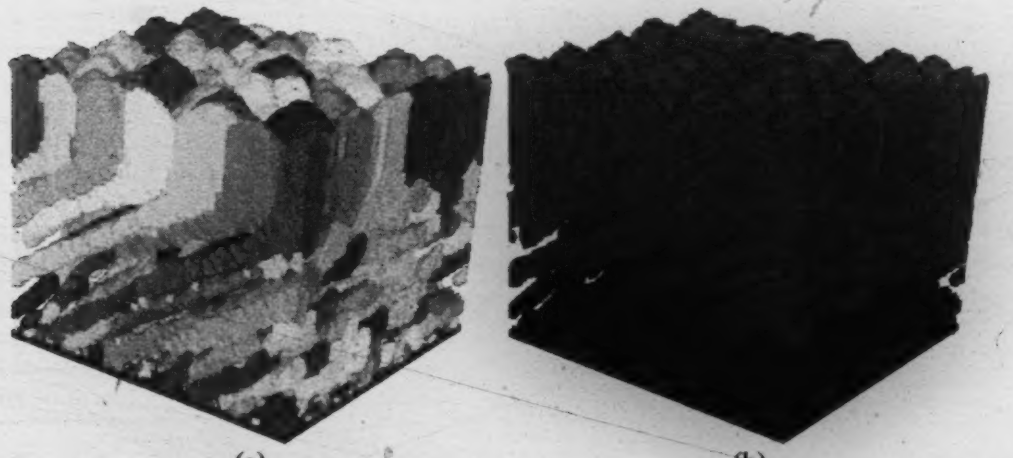
(a) (b)

Figure 8.5 – Simulated GLAD TBCs. In (a), a virtual representation of a thermal barrier coating is depicted which, under known boundary conditions, will produce the temperature gradient shown in (b).

To determine the thermal resistance of the simulated film in Figure 8.5a, Dirichlet boundary conditions were imposed between the top and bottom of the simulated film and the resulting heat flows were calculated. A false-color depiction of the temperature distribution is shown in Figure 8.5b. In the associated temperature plot, Figure 8.6, two distinct zones are visible, corresponding to the porous and cap regions of the simulated film. As expected, the temperature gradient is clearly much more severe in the porous region than in the cap. The 3D-FILMS thermal simulator predicts a thermal conductivity within the GLAD film of only 18% that of a simulated, homogeneous thin film of equal thickness. Thus, we have a second indication of the viability of GLAD thin films as effective thermal barriers. The discrepancy between the two theoretical results is due to a number of factors, including differences in the scale of calculation and differences in the thin films under analysis. (The simulation experiments were performed at Carleton University by T. Smy.)

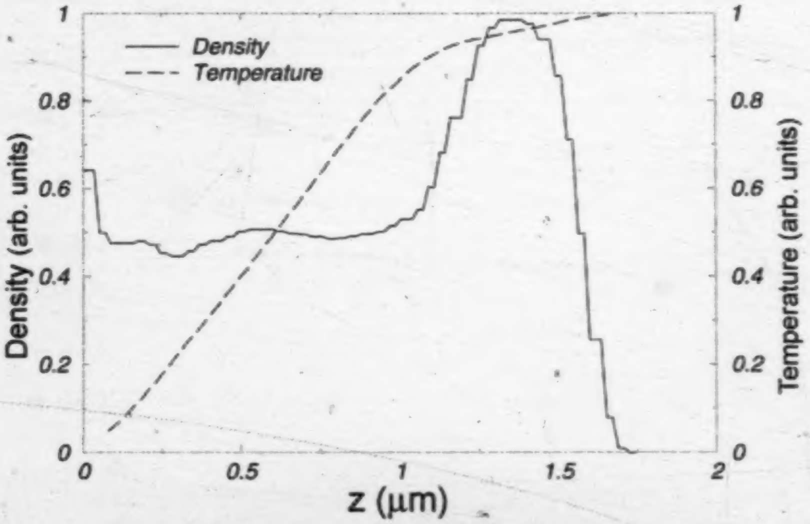

Figure 8.6 – Density and temperature within the simulated thin film. In the porous region, the temperature decreases much more rapidly than in the cap.

8.4 –Thermal Conductivity Measurements

For the GLAD TBC, all of the thermal properties that have been determined to this point have been attained by indirect means, i.e., geometrical approximations and computer simulations. While these methods allow us to predict the behavior of a proposed film, or possibly to understand the characteristics of an optimized TBC, a particular thermal barrier can never truly be judged effective until actual energy flows through an actual thin film, and the physical thermal constants are measured. To correct this deficiency, two different measurement techniques were employed (the mirage method and the 3ω method), and in this section, each technique is described and the results of each measurement are presented.

8.4.1 – The mirage effect: In the mirage method, a focused heating laser is aligned perpendicular to the test film, and a confined spot on the sample surface is temporarily energized. Temperature distributions are immediately induced both in the bulk of the sample and in the air above it, and as the energy dissipates, the spatial and temporal behavior of the gradient is described by the three-dimensional thermal diffusion equation.[22] Distributions of air temperature lead to distributions in the refractive index, and a second probe laser directed nearly parallel to the plane of the sample surface will be deflected by these gradients. The amplitude and phase shift (relative to the heating pulse) are recorded as a function of the horizontal distance between the pulse and probe lasers, and the data are fitted to solutions of the 3-D diffusion equation. Appropriate boundary conditions on heat flux and temperature continuity allow us to obtain the thermal diffusivity α. A figure illustrating the technique is shown in Figure 8.7, and additional details of the mirage method may be found elsewhere.[23-26]

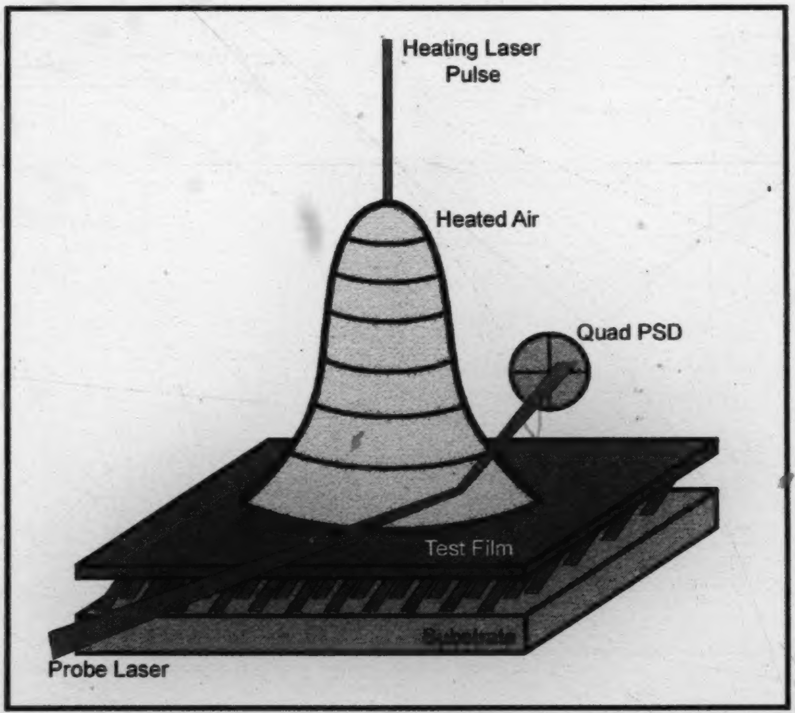

Figure 8.7 – The mirage technique. A pulsed laser heats the surface of the TBC creating temperature gradients in the air above. The temporal and spatial characteristics of the gradient are probed by a second laser and fitted to the diffusion equation.

8.4.2 – The 3ω technique: The three-omega (3ω) method is a self-calibrating AC electrical technique, wherein a known amount of electrical power heats a specimen, and the thermal conductivity, κ, is measured. To introduce heat into the sample, the method employs an evaporated metallic strip in intimate contact with the film surface.

Although a variety of materials and geometries could be utilized, a typical strip consists of aluminum having the dimensions 4mm x 30μm x 200nm, and it is formed either by photolithography or shadowmasking. Heat is introduced into the vicinity of the strip by an electrical signal with an angular frequency ω, which, because heating is based on the square of the input voltage, induces oscillatory thermal gradients in the bulk of the sample at a frequency 2ω. Since the resistivity of a thin film is a function of temperature, the thermal oscillations are probed by measuring variations in the resistance of the strip.[27] A 2ω temperature oscillation driven by an AC current at ω produces voltage oscillations at 3ω. The voltage amplitude at the third harmonic can be measured with a lock-in amplifier, and a fit to a function involving frequency yields κ. The 3ω technique is illustrated in Figure 8.8, and additional details are presented by Cahill and Pohl.[27]

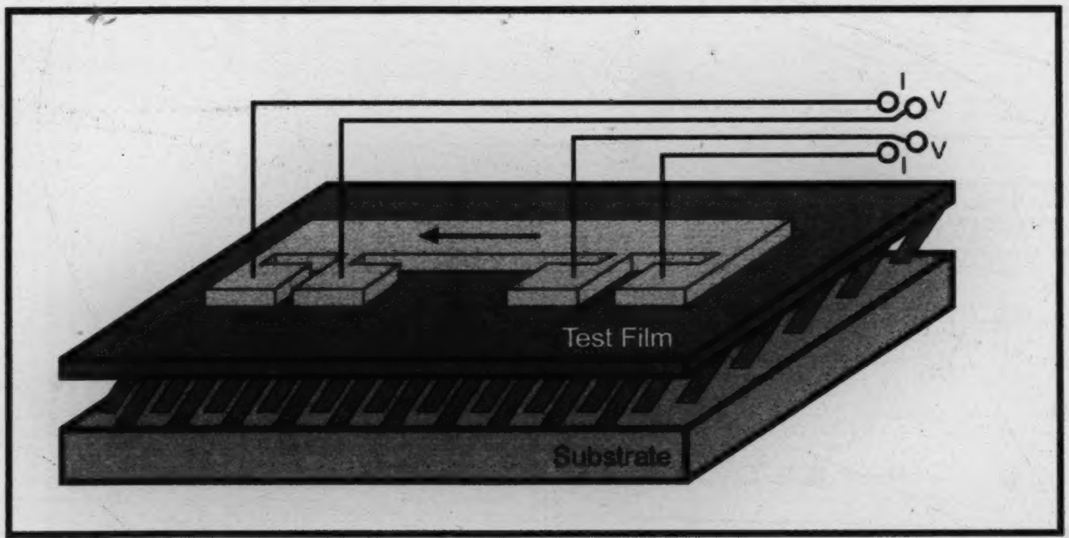

Figure 8.8 – The 3ω technique. AC current flows along a metallic strip, heating the film and inducing voltage oscillations. The oscillations are measured to determine thermal constants.

8.4.3 – Test results: Two different specimens were evaluated at the National Institute of Standards and Technology in Gaithersburg, MD by E. Gonzalez using one or both of the measurement methods. The first specimen studied was a dense, 1μm thick film of YSZ which was intended to resemble a typical, state of the art, thermal barrier coating. It was deposited by EB-PVD at normal incidence. Using the Mirage method, the room temperature thermal diffusivity value obtained for this sample was 0.53mm^2/s ±

0.07mm^2/s, which is within 21% of the reported average values for pure ZrO_2 (0.67mm^2/s at 303K).[28] The reduced diffusivity recorded here is not surprising in light of a number of effects: Y_2O_3 incorporated in the film will have an unknown contribution to the combined conductivity, and unless substrate heating is utilized, limited adatom diffusion, even in normally deposited films, invariably leads to the incorporation of some porosity within deposited zirconia. Thus, a measured diffusivity less than that of bulk specimens is not unreasonable.

Both measurement techniques were employed to evaluate the sample of Figure 8.3b. The values obtained with the Mirage method and the 3ω method were respectively 0.08mm^2/s ± 0.01mm^2/s and 0.05mm^2/s ± 0.01mm^2/s. These values are 15% and 9% that of the dense sample, which supports claims that this TBC structure is of high thermal resistance. These results are shown in Table 8.2.

Test Method	Dense Sample	GLAD TBC
3ω Technique	untested	0.05 mm^2/s
Mirage Technique	0.53 mm^2/s	0.08 mm^2/s

Table 8.2 – Results of the thermal diffusivity measurements.

Because the values are near the effective sensitivity limit of the test methods, a cumulative uncertainty of 10% was estimated in the measurement technique itself. In this case, we have less confidence in the mirage results because the thermal diffusion length scales achieved on these specimens are comparable to the size scales of the heating and the probe beams, thus approaching experimental conditions that are no longer valid. In both cases, as the conductivity of the specimen decreases, it approaches the conductivity of the air above the specimen, which results in a decreased detection sensitivity. In addition, both test methods heat the surface of the TBC and subsequently track changes in the surface temperature, but because thermal conductivity is greatest in the capping regions, the majority of diffusion will occur in these areas, and the results obtained will overestimate the thermal conductivity of the TBC system as a whole. In reality, we measure an upper bound of the thermal conductivity. Other sources of error include the difficulty in accurately determining density and thickness in the ceramic thin films.

The calculation of thermal conductivity from thermal diffusivity in an inhomogeneous, multilayered thin film is also a difficult problem. In a homogeneous film, thermal conductivity is related to diffusivity by the relation: $\kappa = \alpha\rho C_p$. However, this simple relation is not necessarily valid in thin films of more complex structure. Despite this, the thermal conductivity in these films will certainly be dependent upon the thermal diffusivity, and thus, a reduction in diffusivity to 9% that of dense films is evidence for an associated large reduction in thermal conductivity.

Thermal barriers in real life applications will, very likely, consist of additional layers, intended to protect against corrosion or aid in bonding.[29] They will also, very likely, be thicker and operate at temperatures well above 300K.[30] As such, these measurements do not represent the thermal conductivity or diffusivity of TBCs in their ultimate applications. They are, however, useful as a relative comparison between films. If the dense, control film represents the approximate structure of the YSZ portion of a currently acceptable TBC film, it may clearly be seen that films produced by GLAD allow a significant reduction in thermal conductivity over films currently considered acceptable.

Sections of this chapter have been excepted from the paper entitled, "Porous thin films for thermal barrier coatings", which appeared in volume 138 of Surface and Coatings Technology.[31]

References

1) B.Z. Janos, E. Lugscheider, P. Remer, Effect of thermal aging on the erosion resistance of air plasma sprayed zirconia thermal barrier coating, *Surf. Coat. Technol.*, **113**, 278-285, (1999).

2) G.W. Goward, Progress in coatings for gas turbine airfoils, *Surf. Coat. Technol.*, **108-109**, 73-79, (1998).

3) W. Beele, G. Marijnissen, A. van Lieshout, The evolution of thermal barrier coatings – status and upcoming solutions for today's key issues, *Surf. Coat. Technol.*, **120-121**, 61-67, (1999).

4) S.M. Meier, D.K. Gupta, The evolution of thermal barrier coatings in gas turbine engine applications, *ASME* 92-GT-203, 1-9, (1992).

5) M. Gell, E. Jordan, K. Vaidyanathan, K. McCarron, B. Barber, Y. Sohn, V.K. Tolpygo, Bond strength, bond stress and spallation mechanisms of thermal barrier coatings, *Surf. Coat. Technol.*, **120-121**, 53-60, (1999).

6) K.A. Khor, Y.W. Gu, Thermal properties of plasma-sprayed functionally graded thermal barrier coatings, *Thin Solid Films*, **372**, 104-113, (2000).

7) T.E. Strangman, Columnar grain ceramic thermal barrier coatings, US Patent No. 4,321,311, (1982).

8) H. Xu, S. Gong, L. Deng, Preparation of thermal barrier coatings for gas turbine blades by EB-PVD, *Thin Solid Films*, **334**, 98-102, (1998).

9) C.A. Johnson, J.A. Ruud, R. Bruce, D. Wortman, Relationships between residual stress, microstructure and mechanical properties of electron beam-physical vapor deposition thermal barrier coatings, *Surf. Coat. Technol.*, **108-109**, 80-85, (1998)

10) D.D. Hass, A.J. Slifka, H.N.G. Wadley, Low thermal conductivity vapor deposited zirconia microstructures, *Acta. Mater.*, **49**, 973-983, (2001).

11) G.H. Marijnissen, A.H.F. van Lieshout, G.J. Ticheler, H.J.M. Bons, Thermal barrier coating ceramic structure, U.S. Patent No. 5,876,860, (1999).

12) S. Gu, T.J. Lu, D.D. Hass, H.N.G. Wadley, Thermal conductivity of zirconia coatings with zig-zag pore microstructures, *Acta. Mater.*, **49**, 2539-2547, (2001).

13) K.D. Harris, D. Vick, M.J. Brett, K. Robbie, Improved microstructures for thermal barrier coatings produced by glancing angle deposition, *Mat. Res. Soc. Symp. Proc.*, **555**, 97-101, (1999).

14) A. Lakhtakia, R. Messier, M.J. Brett, K. Robbie, Sculptured thin films (STFS) for optical, chemical and biological applications, *Innovat. Mater. Res.*, **1**(2), 165-176, (1996).

15) J.C. Sit, Thin film/liquid crystal composite optical materials and devices, Ph.D. Thesis, University of Alberta, (2001).

16) M. Suzuki, Y. Taga, Integrated sculptured thin films, *Jap. J. Appl. Phys.*, Part 2, **40**(4A), L358-L359, (2001).

17) E.J. Gonzalez, G. White, L. Wei, Effects of microstructural evolution on the thermal conductivity of α-Al_2O_3 prepared from nano-size γ-Al_2O_3 powder, *J. Mater. Res.*, **15**(3), 744-750, (2000).

18) F.-C. Chou, J.R. Lukes, C.-L. Tien, Heat transfer enhancement by fins in the microscale regime, *Trans. ASME*, **121**, 972-977, (1999).

19) R. Siegel, C.M. Spuckler, Analysis of thermal radiation effects on temperatures in turbine engine thermal barrier coatings, *Mater. Sci. E.*, **A245**, 150-159, (1998).

20) T. Smy, D. Vick, M.J. Brett, S.K. Dew, A.T. Wu, J.C. Sit, K.D. Harris, Three dimensional simulation of film microstructure produced by glancing angle deposition, *J. Vac. Sci. Technol. A,* **18**(5), 2507-2512, (2000).

21) T. Smy, D. Walkey, K.D. Harris, D. Vick, M.J. Brett, Simulation of thin film thermal properties using 3D-FILMS, *Thin Solid Films*, **391**, 88-100 (2001).

22) M. N. Özişik, Boundary Value Problems of Heat Conduction, pp. 5-7, (Dover Publications Inc., New York, 1968).

23) D. Josell, E.J. Gonzalez, G.S. White, Correcting errors in the theory for mirage-effect measurements, *J. Mater. Res.*, **13**(5), 1117-1119, (1998).

24) P.K. Kuo, E.D. Sendler, L.D. Farvo, R.L. Thomas, Mirage-effect measurement of thermal diffusivity. Part II: theory, *Can. J. Phys.*, **64**, 1168-1171, (1986).

25) L. Wei, M. Vaudin, C.S. Hwang, G. White, J. Xu, A.J. Steckl, Heat conduction in silicon thin films: effect of microstructure, *J. Mater. Res.*, **10**(8), 1889-1896, (1995).

26) L.C. Aamodt, J.C. Murphy, Thermal effects in photothermal spectroscopy and photothermal imaging, *J. Appl. Phys.*, **54**(2), 581-591, (1983).

27) D.G. Cahill, R.O. Pohl, Thermal conductivity of amorphous solids above the plateau, *Phys. Rev. B*, **35**, 4067-4073, (1986).

28) Y.S. Touloukian, R.W. Powell, C.Y. Ho, M.C. Nicolaou, Thermophysical Properties of Matter, **10**, (Plenum Publishing, New York, 1973).

29) C. Leyens, U. Schulz, B.A. Pint, I.G. Wright, Influence of electron beam physical vapor deposited thermal barrier coating microstructure on thermal barrier coating system performance under cyclic oxidation conditions, *Surf. Coat. Technol.*, **120-121**, 68-76, (1999).

30) P.G. Klemens, M. Gell, Thermal conductivity of thermal barrier coatings, *Mater. Sci. E.*, **A245**, 143-149, (1998).

31) K.D. Harris, D. Vick, E.J. Gonzalez, T. Smy, K. Robbie, M.J. Brett, Porous thin films for thermal barrier coatings, *Surf. Coat. Technol.*, **138**, 185-191, (2001).

Chapter Nine

Conclusions and Recommendations

9.1 – Summary

In this thesis, a number of new capabilities have been added to the repertoire of glancing angle deposition, and various applications for the technology have been pursued. The thesis can essentially be broken into two sections concerning, 1), fabrication involving GLAD (Chapters 1-5) and, 2), applications of the technology (Chapters 6-8). In the first section, a number of extensions to the existing technique were developed which may provide future researchers with a greater range of choices in tailoring GLAD films to their particular applications. After an introductory chapter, a discussion of chevron thin films and inconsistencies in their column angles was presented, and a new method for producing the films with constant column angles was developed. In Chapter 3, a new, graded density microstructure was formed, whereby deposition was initiated at a low angle and subsequently increased until shadowing became the dominant growth mechanism and structures typical to glancing angle deposition were created. A second structure composed of two alternating materials was also formed, and potential applications in the field of photonic bandgap crystals were discussed. Because photolithography is a critical microfabrication technique, a great deal of time was also spent in developing a compatible process for patterning GLAD thin films. The project was successful, and images of lines of GLAD structures as narrow as 2.5μm were presented along with a reliable procedure for creating additional patterned wafers. Motivated by on-chip chemistry requirements, an investigation of methods of depositing high surface area structures within the confines of microchannel geometries was also undertaken. Two methods of producing such systems were detailed in Chapter 4, and in both cases, the surface area amplification brought about using GLAD films was found to be considerable. In a final demonstration of the versatility of the GLAD process, perforated thin films were then discussed. Using templating techniques, the inverse (or negative) of a GLAD film was created in thin films of photoresist or spin-on-glass. Various perforation shapes were formed, and images of each were included with the thesis. As an extension of the process, these films were then used as double templates, and replicas of the original films in alternate materials were electrodeposited through PTFs. Helical thin films of nickel and copper (a notoriously difficult material to deposit by GLAD) were created in this manner, and other materials are expected to be compatible with the process.

In the second part of the thesis, GLAD films in a number of specific applications were investigated. Devices based on perforated thin films, for instance, were found to act as effective high-speed humidity sensors and as optical polarization rotation devices. Furthermore, H_2S and SO_2 sensors employing GLAD microstructures as an electrolyte reservoir were found to be extremely sensitive electrochemical sensors. Helical Pt films were also found to catalyze conversion reactions for a selected group of hydrocarbons, and performance exceeding than of flat sputtered films was attained. In the final section, the thermal properties of GLAD microstructures were probed, and films were evaluated for application to the thermal barrier coating problem. In these experiments, thermal constants vastly superior to conventional coatings were measured by each of four techniques.

9.2 – Recommendations

As always, innovation leads to more questions than answers, and countless additional avenues of exploration were uncovered during the experiments described in these pages. Concerning the adhesion promotion microstructure, for example, the thin films were successfully fabricated, some simple theoretical calculations were performed, and preliminary adhesion experiments were undertaken, yet time constraints prevented a more thorough investigation of the practical performance of these structures. In the future, the research could be extended by using a scratch testing apparatus to gauge the adhesion. In this type of measurement, a stylus is repeatedly dragged across positions on the film surface with a constantly increasing pressure, and subsequent SEM analyses are used to determine the critical breaking pressure of the structures under test. Performing these tests on an adhesion promoting thin film and a control sample would provide an indication of the effectiveness of the adhesion layer.

Because perforated thin films with highly controllable pore shapes are entirely new structures, this field in particular is filled with opportunities. For example, Schmid, et al., have filled anodic alumina films with metal nanoclusters, creating individually addressable assemblies of nanowires for electronic behavior studies,[1] and Masuda, et al., have formed free-standing membranes from porous alumina precursors.[2,3] Neither technique appears fundamentally incompatible with our perforated thin films process, and in addition, glancing angle deposition provides a much greater range of pore shapes than the standard techniques. It is possible that helical or chevron shape-derived phenomena may be discovered with similar investigations using perforated thin films.

Two additional experiments seem especially pertinent. First, a long-prized goal of the GLAD research effort has been to observe mechanical actuation or resonance in a GLAD film,[4,5] and perforated thin film technology may provide a route to achieving this goal. By spin-filling a perforated thin film or using activated growth from the film walls, a replica thin film may be formed of a low viscosity, hydrophilic polymer. By choosing the correct perforated thin film and polymer, the resulting film will be helical and composed of an extremely low spring constant material. With greater displacements brought about by reduced spring constants, measurements similar to those of M. Seto may now produce observable mechanical actuation in GLAD thin films and new device applications.[4,5] This is depicted in Figure 9.1.

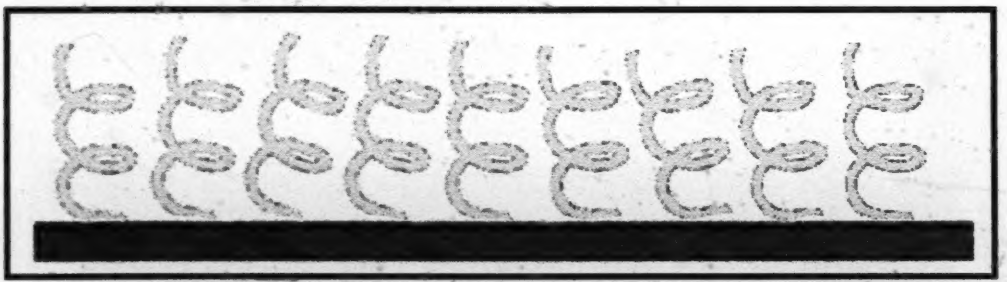

Figure 9.1 – Actuated polymer thin film. By filling a perforated thin film with a polymer and removing the PTF template, a low spring constant material may be fabricated which may potentially be mechanically actuated.

A second experiment is shown in Figure 9.2. By "lifting-off" a perforated film, a membrane may be created, and structures of this nature are extremely useful in analytical chemistry applications. Size-selective,[6-8] or chirally-selective[9,10] filters may be realized and specific separation procedures developed. The first positive indication of separation would only require a suspension of various-sized colloidal particles (or, in the case of chiral separations, a racemic solution) to be filtered through the membrane, and a composition analysis to be performed on the filtered solution. If only a portion of the constituents of the original mixture are present in the filtered solution, then useful devices may be possible.

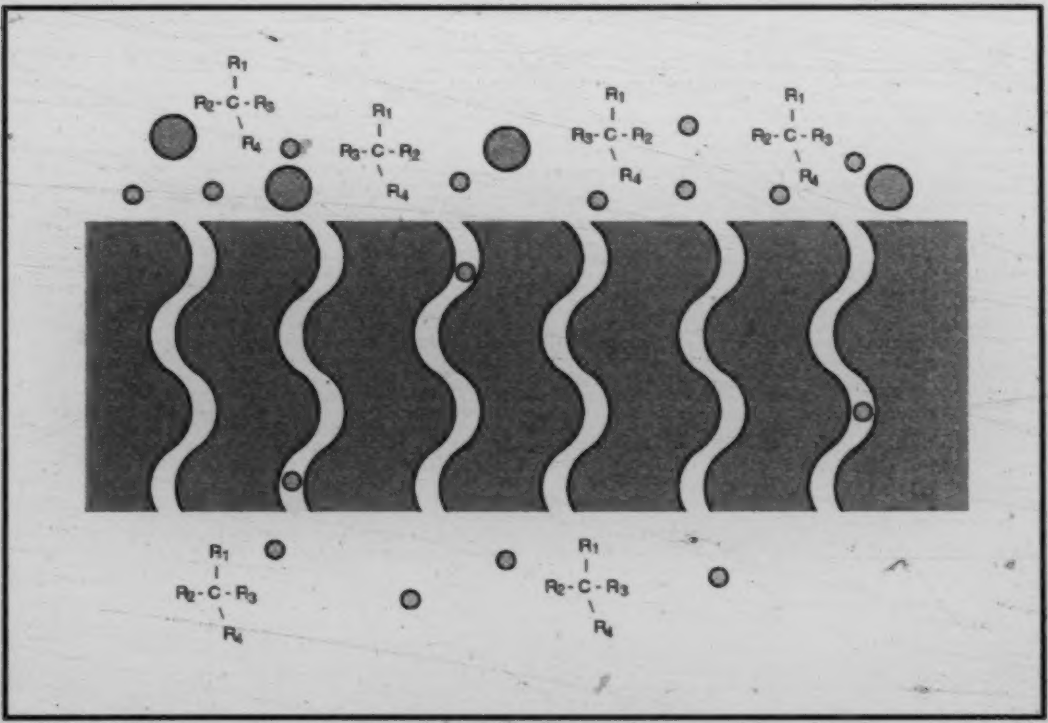

Figure 9.2 – Membrane filtration. A perforated thin film may be removed from the substrate and used in chiral or size-selective separations.

Other useful experiments involve creating perforated films of alternate materials such as metals or ceramics, or further evaluating and optimizing the optical rotation and humidity sensing properties of the existing devices. In addition, the inverted square-spiral geometry is an extremely important thin film microstructure that could conceivably be created using the perforated thin films technique. The photonic properties of this structure are expected to be interesting, and they could easily be evaluated once the structure has been fabricated.

Regarding hydrocarbon sensors, the Pt GLAD films did perform better than sputtered films, but not substantially better, and even with thicker GLAD films, it is not expected that the performance of supported catalyst technology will be superceded. Yet, this invites another possibility: high surface area Al_2O_3 GLAD films may actually provide effective support for higher surface area Pt catalysts, thus allowing all the support/catalyst interaction advantages that these structures provide. In addition, the films would retain their integratability with common microfabrication techniques which would permit their use in on-chip sensor applications. If catalytic hydrocarbon detection research is pursued, supported catalysts should be the focus.

For thermal barrier coatings, both the mirage and 3ω techniques did not truly capture the heating conditions which were appropriate to thermal barriers under their actual operating conditions. In reality, the thermal constants are tensor quantities, and the truly relevant components are those in the direction perpendicular to the substrate. In the mirage effect measurement, heat flowed spherically outward from an essentially 0-dimensional source, and by the 3ω technique, the source was 1-dimensional. However, only when a relatively large, 2-dimensional region of the surface is evenly heated, and energy is forced to flow through the entire TBC structure will the measured constants truly reflect the total conductivity reduction provided by the GLAD TBC. There are a variety of alternate techniques for measuring thermal properties,[11-15] and measurements by any one would further substantiate the claims that GLAD coatings act as effective TBCs, but unfortunately all of the existing techniques are similarly plagued with the problem of measuring the incorrect tensor element. It appears that an entirely new technique employing distributed surface heating must be developed or an existing technique modified to that effect. (Possibly a large spot size of the mirage heating laser or a rastering, resistive heating element as per the 3ω technique would suffice.) By these means, a more accurate representation of the thermal properties of our GLAD TBCs may be realized.

That being said, the thermal properties have actually been relatively well studied, while the durability issue has been relatively neglected. Before one can expect GLAD TBCs in industrial applications, a series of experiments will be necessary to measure their cyclic failure time, spallation resistance, and mechanical properties, and it may be this, rather than additional thermal investigations, that is the most logical course for future work on thermal coatings.

References

1) G. Schmid, M. Bäumle, M. Geerkens, I. Heim, C. Osemann, T. Sawitowski, Current and future applications of nanoclusters, *Chem. Soc. Rev.*, **28**, 179-185, (1999).

2) P. Hoyer, N. Baba, H. Masuda, Small quantum-sized CdS particles assembled to form a regularly nanostructured porous film, *Appl. Phys. Lett.*, **66**(20), 2700-2702, (1995).

3) H. Masuda, K. Nishio, N. Baba, Preparation of microporous metal membranes by two-step replication of the microstructure of anodic alumina, *Thin Solid Films*, **223**, 1-3, (1993).

4) M.W. Seto, K. Robbie, D. Vick, M.J. Brett, L. Kuhn, Mechanical response of thin films with helical microstructures, *J. Vac. Sci. Technol. B*, **17**(5), 2172-2177, (1999).

5) M.W. Seto, B. Dick, M.J. Brett, Microsprings and microcantilevers: studies of mechanical response, *J. Micromech. Microeng.*, **11**, 582-588, (2001).

6) T. Rheinländer, D. Roessner, W. Weitscheis, W. Semmler, Comparision of size-selective techniques for the fractionation of magnetic fluids, *J. Magn. Magn. Mater.*, **214**, 269-275, (2000).

7) T. Rheinländer, R. Kötitz, W. Weitschies, W. Semmler, Different methods for the fractionation of magnetic fluids, *Colloid. Polym. Sci.*, **278**, 259-263, (2000).

8) G.S. Duesberg, J. Muster, V. Krstic, M. Burghard, S. Roth, Chromatographic size separation of single-wall carbon nanotubes, *Appl. Phys. A*, **67**, 117-119, (1998).

9) Y. Mao, M. Warner, Imprinted networks as chiral pumps, *Phys. Rev. Lett.*, **86**(23), 5309-5312, (2001).

10) G. Heppke, A. Jákli, S. Rauch, H. Sawade, Electric-field-induced chiral separation in liquid crystals, *Phys. Rev. E*, **60**(5), 5575-5579, (1999).

11) G.I. Pangilinan, H.D. Ladouceur, T.P. Russell, All-optical technique for measuring thermal properties of materials at static high pressure, *Rev. Sci. Instrum.*, **71**(10), 3846-3852, (2000).

12) R.E. Taylor, Thermal conductivity determinations of thermal barrier coatings, *Mater. Sci. E.*, **A245**, 160-167, (1998).

13) O. Paul, P. Ruther, L. Plattner, H. Baltes, A thermal van der Pauw test structure, *IEEE Trans. Semicond. Manuf.*, **13**(2), 159-165, (2000).

14) R.E. Taylor, X. Wang, X. Xu, Thermophysical properties of thermal barrier coatings, *Surf. Coat. Technol.*, **120-121**, 89-95, (1999).

15) R.D. Cowan, Pulse method of measuring thermal diffusivity at high temperatures, *J. Appl. Phys.*, **34**(4), 926-927, (1962).

Appendix A

Properties of the Humidity Control Chamber

Commercially available humidity control chambers tend to be costly devices, with high quality, scientific testing chambers often priced at over ten thousand dollars. When performing only a limited set of experiments for a short duration, the cost of procuring a humidity chamber can be extremely prohibitive. Often, to circumvent this problem, researchers are led to develop chambers in house,[1] and in this appendix, such a chamber which was assembled for the humidity sensor measurements of Chapter 6 is described.

The physical body of the humidity chamber consists of an 11.4L molded polypropylene container with lid. In this case, the lid is easily removable to facilitate a quick changing of the contents within. The sealing edges around the lid are insulated with foam insulation to prevent air within the chamber from mixing with the ambient environment in an uncontrolled fashion.

The relative humidity within the chamber is continuously measured using a Vaisala RH/T probe. In the specifications, the sensor is reported to be accurate to within 3%RH between 20 and 80%RH, and to within 4%RH between 0 and 20%RH and 80 and 95%RH. The listed response time for the sensor is 15s at 20°C in still air. The probe's output is a voltage signal ranging from 0mV to 100mV proportional to the relative humidity within the chamber. This signal is brought from the chamber using banana jacks, so no internal air escapes in the vicinity of the electrical connections.

The humidity sensor signal enters the control circuit of Figure A.1 through the buffer input in the upper left corner and is amplified with a gain of 100. The operational amplifiers used on the input are high precision, low drift OP-07 amplifiers. The humidity sensor signal is then compared to the target humidity selected using the 5kΩ, ten turn potentiometer. The control output is a slowly integrating voltage signal proportional to the difference between the measured humidity and its set point.

The physical means of varying the chamber humidity are two fans supplying respectively moist and dry air. If the desired humidity within the chamber is above that of the ambient environment, a water source (consisting, in this case, of an uncovered Petri dish filled with water) is placed directly in front of fan A, located within the chamber. The water saturated air immediately above the source is then distributed through the chamber as necessary by operating Fan A. In this configuration, Fan B is responsible for providing dry air from outside the chamber through a plastic tube. As the chamber becomes pressurized, air within the chamber may escape from the area immediately surrounding this tube. If the desired humidity is below that of the ambient air, a desiccant is placed in front of fan A, while fan B supplies humid, external air. Standard 12V fans were used in both cases.

The speed at which each fan rotates determines the chamber humidity. Because the fan speed cannot be reliably controlled by voltage variations, the duty cycle is adjusted instead. Applying voltage for a greater proportion of each cycle results in greater average fan speeds. To accomplish this, the control output is compared with the output of a triangular wave oscillator operating at 1.6Hz. The 2.2MΩ resistor provides positive feedback to expedite switching and reduce ringing in the comparator. The comparator signal is then clamped between +15V and –0.7V with a diode circuit and amplified using ICL7667 chips. The amplified signal drives one of the fans, while the inverted signal drives the second during the alternate part of the duty cycle. When it is desired to switch from the upper humidity range to the lower (or vice versa) by replacing the interior water source with desiccant (or vice versa), the DPDT switch must be changed to the alternate position to ensure the correct part of the duty cycle controls the correct fan.

In the vicinity of the fans, small fluctuations in temperature are unavoidable due to mechanical heating. In addition, any experiments undertaken within the chamber itself may also introduce sources of heat, and as a result, the homogeneity of the water content cannot be guaranteed. Also, internal air flows follow relatively consistent paths within the chamber, leading to the establishment of additional humidity gradients. The chamber does, however, provide consistent humidity readings at equilibrium.

Using this humidity chamber and control circuit, we have been able to achieve measured humidity levels between 1% and 97% of saturation humidity with a time weighted stability of approximately ±1%. Since the control circuit always seeks to match its set point voltage with that of the humidity sensor, regardless of the reliability of the sensor signal, the accuracy of the chamber is strongly dependent upon the accuracy of the humidity sensing device. As such, this chamber is less effective than some commercially available models in which tolerances of ±2% RH are common (the TestEquity 1207C, for instance). While our chamber is capable of, at best, ±3% RH, the device is much less expensive to construct. As a test of the response time, the chamber humidity was raised from its ambient value of 40% to a selected value of 75%. This change was completed in 195s.

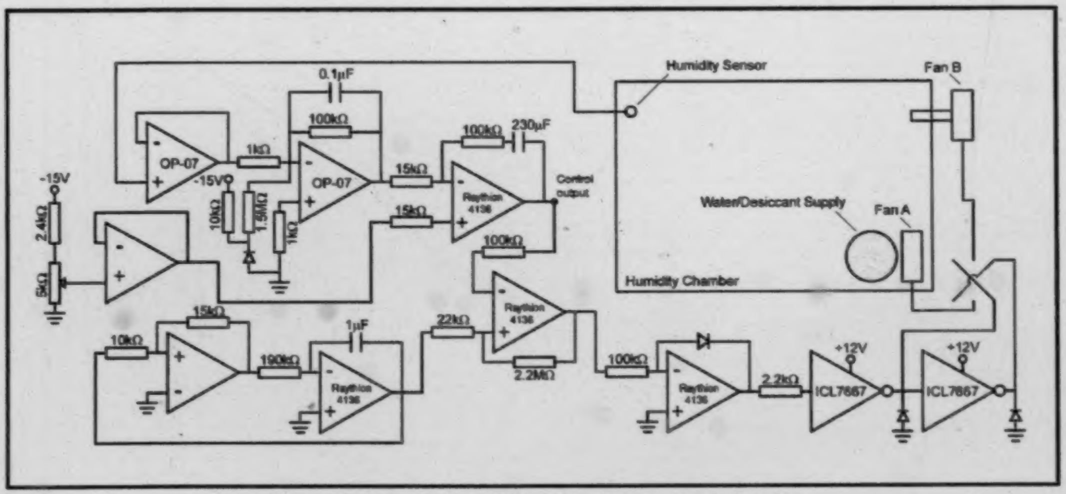
Humidity Sensor
Fan B
0.1μF
100kΩ
OP-07
1kΩ
OP-07
100kΩ
230μF
-15V
-15V
2.4kΩ
10kΩ
1.5MΩ
1kΩ
5kΩ
15kΩ
15kΩ
Raythion 4136
Control output
Water/Desiccant Supply
Fan A
100kΩ
Humidity Chamber
15kΩ
10kΩ
190kΩ
1μF
Raythion 4136
22kΩ
Raythion 4136
2.2MΩ
100kΩ
Raythion 4136
2.2kΩ
+12V
ICL7667
+12V
ICL7667

Figure A.1 – The humidity chamber control circuit.

Portions of this appendix have been excerpted with permission of the Institute of Physics from the paper entitled, "A simple and inexpensive humidity control chamber", which appeared in the January 2002 issue of the journal Measurement Science and Technology.[2] The article may be found online at http://www.iop.org/journals/mst.

References

1) I. Harvey, G. Coles, J. Watson, The development of an environmental chamber for the characterization of gas sensors, *Sens. Actuators*, **16**, 393-405, (1989).

2) K.D. Harris, A. Huizinga, M.J. Brett, A simple and inexpensive humidity control chamber, *Meas. Sci. Technol.*, **13**(1), N10-N11, (2002).

Appendix B

The Response Time Test Circuit

The measurement of the response time for a capacitive sensor with capacitance variations over as many as five orders of magnitude is a significant design problem. Common capacitance meters either sample at rates much too slow to be useful (i.e., sampling rates on the order of 1-2 samples per second are common), lack digital outputs, or are prohibitively expensive. Therefore, an original circuit assembled by A. Huizinga was used to measure response speeds for the humidity sensors described in this thesis.

The response speed test circuit consists of two basic block diagram stages: an oscillator which produces a signal with a frequency proportional to the sensor capacitance, and a frequency-to-voltage converter which extracts a voltage signal proportional to the oscillator frequency. The two blocks will be considered independently.

In Figure B.1, a schematic drawing of the oscillator circuit is provided. The humidity sensor is attached to the circuit as a component of an integrating operational amplifier configuration in the lower left corner of the figure. The two diodes (Part No. 1N914) to the right of the figure limit the operational amplifier input voltages to the range between +0.85V and –0.85V. Assuming an initial state where the input is +0.85V, and the output at point A is –0.85V, the subsequent response at point A is a linearly rising ramp between -0.85V and +0.85V. As the sensor capacitance changes to reflect the ambient humidity conditions, the integration time between the output bounds also changes, higher capacitance values leading to slower ramp speeds. The output voltage, V_A, is then compared to its input in the LM339 comparator microchip. When V_A exceeds the input, the comparator switches between the high and low states, and the amplifier input is shifted to –0.85V. The integrating amplifier then begins to ramp downward. The oscillator output, V_B, is a square-wave signal which switches between ±15V at a frequency depending upon the sensor capacitance. Higher capacitance values lead to lower frequency oscillation. The transistor/resistor configuration near the center of the schematic is a high-speed buffer stage for the LM339 output.

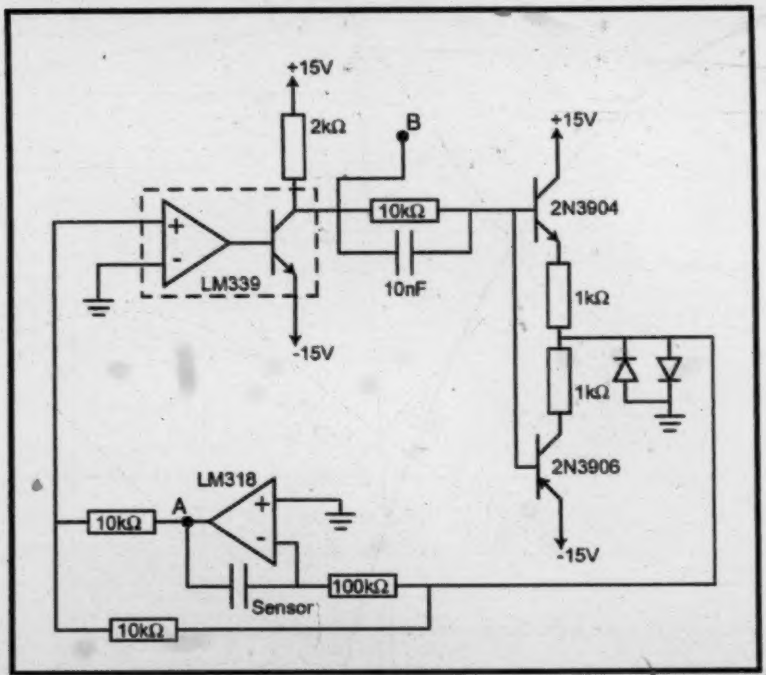

Figure B.1 – The oscillator circuit. The capacitive humidity sensor is attached to the circuit in lower section, and the output is a square-wave signal which oscillates at a frequency depending on the sensor capacitance.

The frequency-to-voltage converter portion of the circuit is shown in Figure B.2. At this stage, the oscillator output is first converted to a 0-15V signal using a 7667 microchip and used to drive a 4047 one-shot. The one-shot delivers a fixed-duration, +15V pulse for every rising edge of the oscillator signal. The pulse duration is adjusted to be 90% of the period at the highest oscillator frequency so as to avoid any peculiarities that may arise as a result of overlapping one-shot pulses. The on-time for the one-shot output is fixed, while the off-time varies with the change in sensor capacitance.

Within the SSM2141 chip, the resistances are matched, and the gain of the circuit is set at unity. Open-circuiting either of the input arms passes any signal on the opposing arm unchanged, while tying the two arms together leads to a zero output. Therefore, using a common input with one arm passed through a capacitor rejects the high frequency AC signal and passes the DC. This DC signal is essentially an average value for the one-shot output, and consequently it is also a voltage signal proportional to the oscillator frequency and the sensor capacitance.

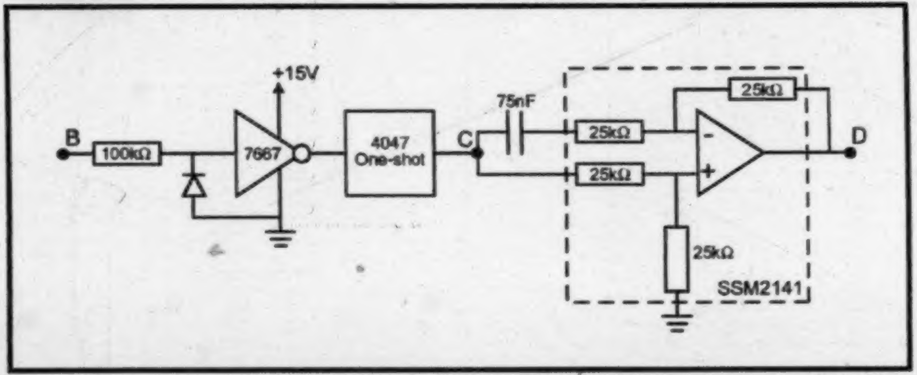

Figure B.2 – The frequency-to-voltage converter. The oscillator output triggers a one-shot chip, and the DC component of the stream of one-shot pulses is then extracted by the SSM2141 chip. This signal is a voltage proportional to the original sensor capacitance.

As a test, the frequency-to-voltage converter portion of the circuit was energized with a frequency sweep from a WAVETEK Model 166 Sweep Generator. The sweep range was 150Hz to 35kHz, and the sweep frequency was 10.63Hz. The circuit attempted to track the frequency changes, and it was found that the response time for the circuit itself was approximately 5ms. This is the fastest rate of change that the circuitry is capable of measuring. Sample waveforms for each of the labeled schematic points in response to an arbitrary, stable capacitance are shown in Figure B.3.

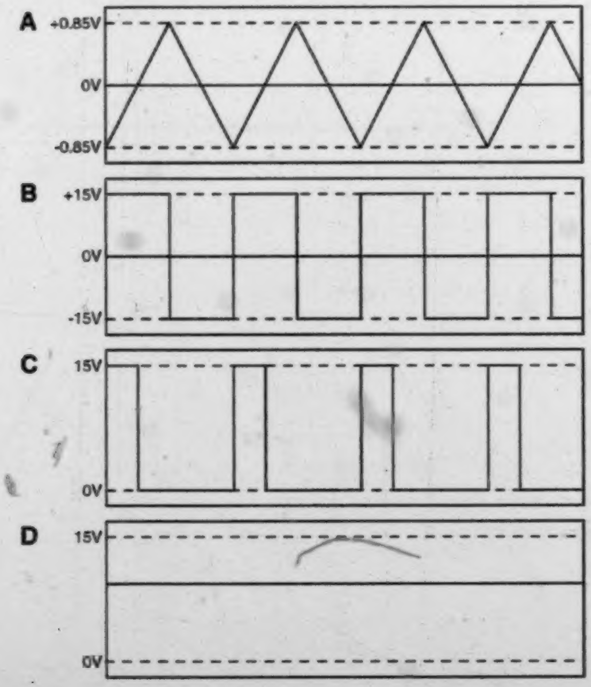

Figure B.3 – Sample response speed test circuit waveforms. a) is the integrating amplifier output, b) is the oscillator output, c) is the one-shot output, and d) is the frequency-to-voltage signal.

Appendix C

Derivation of the Conversion Efficiency Equation

The conversion efficiency, η, is defined in terms of the inlet and outlet reactant concentrations, c and c_o as:

$$\eta = 1 - \frac{c}{c_o} \qquad \text{(C.1)}$$

For a first order reaction, (which is typical of many heterogeneous catalyst reactions) the rate of reactant consumption is proportional to the concentration:[1]

$$\frac{dc}{dt} = -\kappa c \qquad \text{(C.2)}$$

Thus,

$$c = c_o e^{-\kappa t} \qquad \text{(C.3)}$$

The temperature dependence of κ usually obeys the Arrhenius law:[2]

$$\kappa = \kappa_o e^{-E/kT} \qquad \text{(C.4)}$$

where E is the activation energy for the reaction, and k is Boltzman's constant. In our case, the gas is not stagnant, but rather moves past the sample with a characteristic residence time, t_r, given by:

$$t_r = \frac{lwh}{Q} \frac{T_o}{T} \qquad \text{(C.5)}$$

where the product of l, w and h is the reactor volume, Q is the volumetric flow rate of the gas, T is the gas temperature in the reactor, and T_o is the gas temperature at the location of the mass flow controllers. Only a fraction α of reactant molecules will diffuse to the sample within this residence time, and by solving the one-dimensional diffusion equation, this fraction may be given approximately by:

$$\alpha = \frac{\sqrt{2Dt_r}}{h} \qquad \text{(C.6)}$$

where D is the coefficient of binary molecular diffusion. For most reactant species of interest, the diffusion coefficient has a temperature dependence of the form:[3]

$$D = D_o\left(\frac{T}{T_o}\right)^n \qquad \text{(C.7)}$$

Combining all of these equations, and using an n of 1.75,[3] we then arrive at the following expression for the conversion efficiency:

$$\eta = \sqrt{\frac{2D_o lw}{hQ}\left(\frac{T}{T_o}\right)^{0.75}}\left[1-\exp\left(-\frac{\kappa_o T_o lwh}{Q}\frac{e^{-E/kT}}{T}\right)\right] \qquad \text{(C.8)}$$

This behavior of equation (C.8) is illustrated in Figure C.1, where the conversion efficiency is plotted using an arbitrary set of activation energies and rate constants as a function of temperature for CO and C_3H_6. At low temperatures, the reaction is kinetically limited and the conversion efficiency increases roughly exponentially with temperature. At high temperatures, the reaction becomes mass transport limited as diffusion of the reactant to the catalyst becomes the rate determining step. (To further illustrate this limit, I have included in dashed lines the factor α which was described above.)

Experimentally, the value we are most interested in is the "light-off temperature", defined as that temperature for which the conversion efficiency reaches half of its maximum (mass transport limited) value. The light-off temperature is directly related to the activity and the number of catalytic sites on the sample, and thus a low light-off temperature is characteristic of a good catalyst.

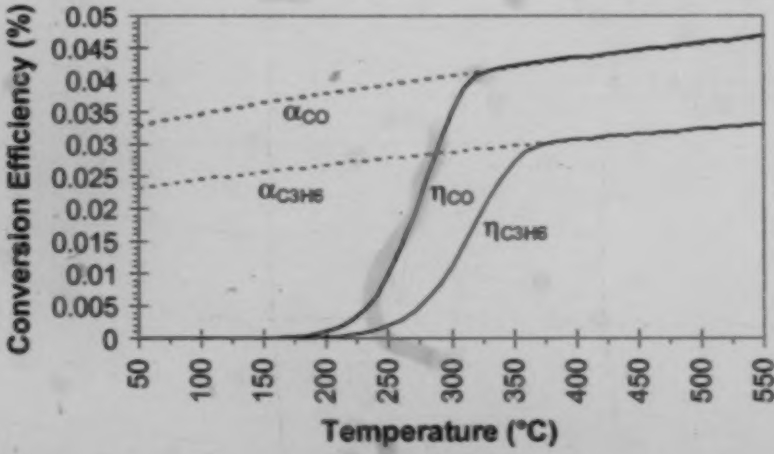

Figure C.1 - Calculated conversion efficiency as a function of temperature. These plots were calculated using volumetric flow rates of 1sccm, an activation energy of 100kJ/mol, and rate constants of $2\times10^{14}s^{-1}$ and $5\times10^{13}s^{-1}$ for CO and C_3H_6, respectively. The cross-sectional dimensions of the reaction vessel are 5cm x 5cm.

Portions of this appendix first appeared in the report entitled, "Evaluation of the catalytic properties of a Pt-GLAD film for use in automotive sensor applications", which appeared in Ford Research Laboratory technical report SRR-2000-0057.[4]

References

1) S.R. Radel, M.H. Navidi, Chemistry, p. 645, (West Publishing Co., 1994).

2) S.R. Radel, M.H. Navidi, Chemistry, p. 666, (West Publishing Co., 1994).

3) J.R. Welty, C.E. Wicks, R.E. Wilson, Fundamentals of momentum, heat and mass transfer, pp. 486-488, (John Wiley & Sons, New York, NY, 1984).

4) J.R. McBride, K.E. Nietering, M.J. Brett, K.D. Harris, Evaluation of the catalytic properties of a Pt-GLAD film for use in automotive sensor applications, Ford Research Laboratory Technical Report SRR-2000-0057, (2000).